AN ACTOMYOSIN DRIVEN, PRESSURE BASED ADHESION MODEL OF CONFINED GLIOBLASTOMA MULTIFORME CELL MIGRATION.

by

JAMIE WRIGHT

Presented to the Faculty of the Graduate School of
The University of Texas at Arlington in Partial Fulfillment
of the Requirements
for the Degree of

DOCTOR OF PHILOSOPHY

THE UNIVERSITY OF TEXAS AT ARLINGTON
May 2016

Acknowledgements

I would like to express my deepest gratitude to Dr. Cheng-Jen Chuong, my committee chair, for his guidance and support as well as for the countless discussions and debates that eventually shaped this research. I would also like to thank all of my committee members including Dr. Digant Dave, Dr. Young-Tae Kim, Dr. Robert Bachoo, and Dr. Samarendra Mohanty for the discussion, advice, and guidance needed to complete this research.

In addition, special thanks to James Nyagilo (PhD) at UT Southwestern for the countless hours providing remarkable images. Without your work none of the analysis or modeling would have been possible. Thanks to Loan Bui at UTA for the microchannel device fabrication and culturing information. Thanks to Yuxiao Sun (PhD) and Nanda Regmi (PhD) for their work with cell preparations and cell transfection as well as protein tagging. Thanks to all members of our team for weekly discussion and suggestions including Armin Soltan-Zadi and Sara Picirrillo.

Special thanks to all of my family, especially my wife, Reshma, and daughter, Sabrina, whose patience and support made it easy to work the long hours when necessary.

Thanks to the NIH and CPRIT for funding the research that made all of this possible. Thanks to UTA and the department of bioengineering for all of the support.

April 22, 2016

Abstract

AN ACTOMYOSIN DRIVEN, PRESSURE BASED ADHESION MODEL OF CONFINED GLIOBLASTOMA MULTIFORM CELL MIGRATION.

Jamie Wright, PhD

The University of Texas at Arlington, 2016

Supervising Professor: Cheng-Jen Chuong

Glioblastoma multiforme (GBM) is the most aggressive and common form of glial tumors arising in the support cells of the brain. Cell migration plays a critical role in undermining the surgical resection of tumors. Peripheral cells freely detach and invade the surrounding tissue, preferentially collecting and migrating within confined, mechanically distinct environments such as along the borders of white matter tracts and vasculature. These tracks have been mimicked experimentally using small, rectangular PDMS microchannels. GBM cells will readily enter and migrate through these micro-channels in the absence of any chemoattractant, even without specific cell-substrate adhesion (integrins) if channel dimensions decrease to the point of dorsal-ventral compression of the nucleus. Live imaging of GBM cells with fluorescently labelled F-actin and myosin reveals that, unlike in larger channels, cells confined to the point of nuclear compression will often adopt protein distributions dissimilar to what is observed in 2D. Actin and myosin profiles are redistributed to amass at localized regions near both axial terminals and diminish toward the center of the cell. A subset of these fully confined cells termed quasi-stable length (QSL) migrators will move with stable cell lengths under slight axial shortening. Because these cells are migrating in tight confinement without the usual cycles of protrusion and retraction at the front edge that accompany mesenchymal migration strategies, they make good candidates for employing possible alternative cell/substrate adhesion mechanisms. Using Comsol, we have constructed a 3D finite element model treating the cell as a biphasic material, to allow for separate tracking of the cytoskeleton and cytosol phases, where dynamic, experimentally derived actin and myosin distribution data can be coupled with governing equations to quantitatively predict the roles and interactions of forces (adhesion, polymerization, and actomyosin contractile forces) that drive complex 3D cell migration in the absence of specific cell-substrate binding. The model is unique in that it incorporates dynamic experimental data to drive complex temporally changing behavior. While previous models have used equations describing protein reaction kinetics or integrin binding kinetics to study migration, the current model is driven by experimentally obtained distributions. The model predicts that cells can utilize transient, actomyosin-driven, pressure-dependent anchors at the cells terminal ends derived from regional actomyosin foci to create a temporary frictional foothold to overcome nucleus-channel friction and enable the cell to migrate. In addition the model verified the importance of tensile homeostasis through an actively contracting coupling between opposite axial boundaries.

Table of Contents

List of Illustrations

List of Tables

Chapter 1

GBM and Confined Migration

1.1 Gliobalstoma multiforme (GBM).

Gliomas are a collection of tumors arising from glial or support cells within the central nervous system. Gliomas have been classified histologically by the World Health Organization (WHO) into one of 4 grades (I, II, III, and IV). Unfortunately, grade IV tumors or glioblastoma multiforme (GBM), which are the most invasive and aggressive are also the most common (1). GBM is characterized by uncontrolled proliferation, diffuse invasiveness, rampant necrosis, widespread angiogenesis, and extensive heterogeneity (2). These grade IV tumors are further divided into either primary or secondary subtypes with primary tumors arising de novo without any evidence of prior disease and secondary tumors arising from progressive transformation (2). Primary tumors are more common, occurring more often in older patients whereas secondary tumors are more infrequent, occurring in younger patients, under 45 years old.

Although these tumors are relatively uncommon, their incidence carries a high mortality rate. Even with treatment by surgical resection along with radiation and chemotherapy with temazolomide, median survival is only 12 to 15 months for patients with GBM (3). In addition GBM accounts for 60 to 70% of the malignant gliomas(3). Thus, these tumors require significant attention based solely on the severity of the prognosis.

Poor surgical outcomes in treating GBM lesions seem to be tied to both the topologically diffuse nature of the tumors as well as the diffuse infiltration throughout the brain.   The topological heterogeneity makes complete resection challenging. In addition, unlike other tumors, glial tumors show higher incidence of localized spreading but lack the ability to establish secondary tumors outside the CNS by utilizing blood vessels or the lymphatic system(2). This inability to surgically resect the entire tumor and all of its margins along with high incidence of very localized spreading away from the tumor margins leads to frequent (> 90%) tumor recurrence adjacent to the resection cavity(2). In addition GBM cells which have broken away from the margins of the original tumor can invade distant brain tissue possibly employing a more primitive form of migration, most frequently migrating along white matter tracts and blood vessel basement membranes before giving rise to new tumors away from the margins of the original tumor (1, 2).

The failure of adjunct treatment strategies like radiation and temozolomide implies that at least a portion of the migrating cells have adopted some resistance to these strategies. Recent work by Bui et al suggests that physical confinement during migration could confer migrating cells with resistance to chemotherapy that might otherwise be effective against cells migrating on a 2D planar platform (4). Consequently, it is imperative to explore the migration strategies and mechanical phenotypes associated with cells in confined environments and compare them to 2D strategies to highlight any differences that could lead to a better understanding not only of cell navigation but of changes to cell behavior in general.

1.2 Cell Migration.

1.2.1 Cells adopt different migration strategies depending on environment

Cancer cell invasion is typically regarded as heterogeneous, adaptive, and plastic with cells migrating either in groups or individually (5). Cancer cells employ a variety of migration strategies during invasion and are capable of adapting and switching strategies as the environment dictates. Cells achieve movement by integrating any number of cytoskeleton (csk) derived protrusive and/or contractile engines in concert with a specific (integrin based) or nonspecific cell-substrate transmission system. It is important to recognize that movement in 3D is certainly more complex than any single propulsion scheme with cells being able to draw from an array of csk derived engines and couple them with an assortment of transmission systems eliciting an integrated response to complex biophysical environmental cues. Biophysical stimuli could invoke mixed migration strategies or result in hierarchical overrides. For example chemo-attractive stimuli might override a cell’s normal response to mechanical cues inducing a strategy more dependent on polymerization dependent protrusion. Clearly, cells can draw from several protrusive engines including actin polymerization driven protrusion and microtubule driven protrusion. Once more, cells can utilize actomyosin based motors to drive regional contraction. Theoretically, the cell could achieve force transmission to the substrate in 3D confined environments via either specific binding to the substrate or via local frictional engagements stemming from internal pressure or polymerization derived forces pushing the cell boundary into contact with the adjacent substrate. Utilization of a particular transmission system may arise solely as a result of the cell balancing efficiency against a thrust threshold. To summarize, it makes sense that cells may collect all biophysical environmental cues integrating a categorical response by matching appropriate protrusive or contractile engines with the most efficient transmission system capable of overcoming any environmental resistance to movement. Consequently, it stands to reason that to define any particular migration strategy at any particular time it is necessary to characterize the combination of csk driven engines invoked by the cell as well as to characterize the mechanism of force transmission between the cell and environment.

. While observations from 2D provide critical insight into some of the processes and controls that are available to cells in 3D, strategies can actually differ significantly depending on substrate geometries (6). Although cells can theoretically employ either a polymerization or bleb based mechanism on 2D planar surfaces, in the absence of multiple constraining surfaces which might be exploited by the cells as surface anchors to promote squeezing, specific cell substrate adhesion is all but mandatory as illustrated in fig. 1A and 1B.

Typical mesenchymal migration involves the coupling of 2 different engines (contractile, polymerization) with a graded focal adhesion based transmission. Polymerization derived protrusion within a thin lamellipodium at the leading edge of the cell ratchets the front membrane forward as new actin monomers are inserted between the growing actin branches and the plasma membrane(7-12). Behind the lamellipodium lies the lamellum where backward flowing (retrograde flow) actin approaching from the lamellipodium is compressed into bundles that combine with myosin II, tropomyosin, and actin crosslinkers like α-actinin that eventually form a network of stress fibers that attach to new focal adhesions and contract to maintain the cell shape as well as pull the rear forward. Within the lamellipodium, as new actin is added to the leading edge and the leading membrane is pushed forward, the actin csk in the lamellipodium is in turn pushed backward creating a retrograde actin flow directed back toward the cell interior. Newly developed focal adhesions (FA) located just posterior to the lamellipodium grip the substrate providing a clutch whereby the cell can anchor to the substrate and turn polymerization at the leading edge into forward propulsion(6, 13, 14). The efficiency of this clutch dictates how much actin polymerization within the lamellipodium is converted to leading edge movement versus retrograde flow. Higher efficiency in the clutch mechanism (more gripping) results in less actin retrograde flow and more leading membrane thrust. Slippage in the clutch promotes more retrograde flow and reduces the proportion of actin polymerization that is converted to forward ratcheting of the membrane(6). As the cell moves forward newly established FAs at the front of the lamellum migrate slowly toward the rear along with any attached stress fibers. Graded adhesion between the front and rear of the cell is critical for converting leading edge protrusion and acotmyosin contraction into forward propulsion (14, 15). It is imperative that front end of the cell grips more tightly than the rear upon contraction so that adhesions at the rear can be ruptured allowing the cell posterior to be pulled forward(6, 14, 15). So actin polymerization in the lamellipodium ratchets the leading edge forward and produces retrograde actin flow in a ratio depending on the efficiency of adhesion at the front edge of the lamellum. Actin and myosin derived contraction in the stress fibers and graded actin polarity bundles of the lamellum and cell body create tension in the cell, determine cell shape, and pull the rear forward when adhesion is graded across the cell so that stronger adhesion near the front of the lamellum is maintained while FAs at the rear of the cell rupture. FA turnover allows ruptured FAs from the cell rear to recycle and reestablish nascent adhesions near the front of the lamellum.

1.2.2 3D migration complicates analysis

In complex 3D environments cell locomotion becomes more nebulous, involving a wider spectrum of possible migration strategies as illustrated in fig 1(C-E) (16). While 2D planar migration primarily is characterized by a mesenchymal-like approach employing lamellipodia driven polymerization at the leading edge coupled with actomyosin contraction and integrin driven grip and slip transmission to planar surfaces, migration in the 3D environment can embody multiple protrusive structures including blebs, lobodpodia, pseudopodia, ruffles, and filopodia (6, 17, 18) . Once more, cells in 3D environments appear readily able to switch migration strategies between protrusion types in response to stimuli (17). Although necessary for migration on 2D surfaces, contractility and integrin-dependent adhesion become dispensable in 3D environments (6, 17-19). Focal adhesions have been shown to decrease during migration in reconstituted ECM gels (16, 20). All of this indicates that cells probably are capable of employing multiple migration tactics within the confined micro-environments afforded by complex 3D environments. Genetic alteration due to malignant transformation further complicates the picture. Cancer cells are known to employ multiple invasion strategies and can switch easily between these techniques (plasticity) leading to heterogeneous and adaptive migration styles (5).

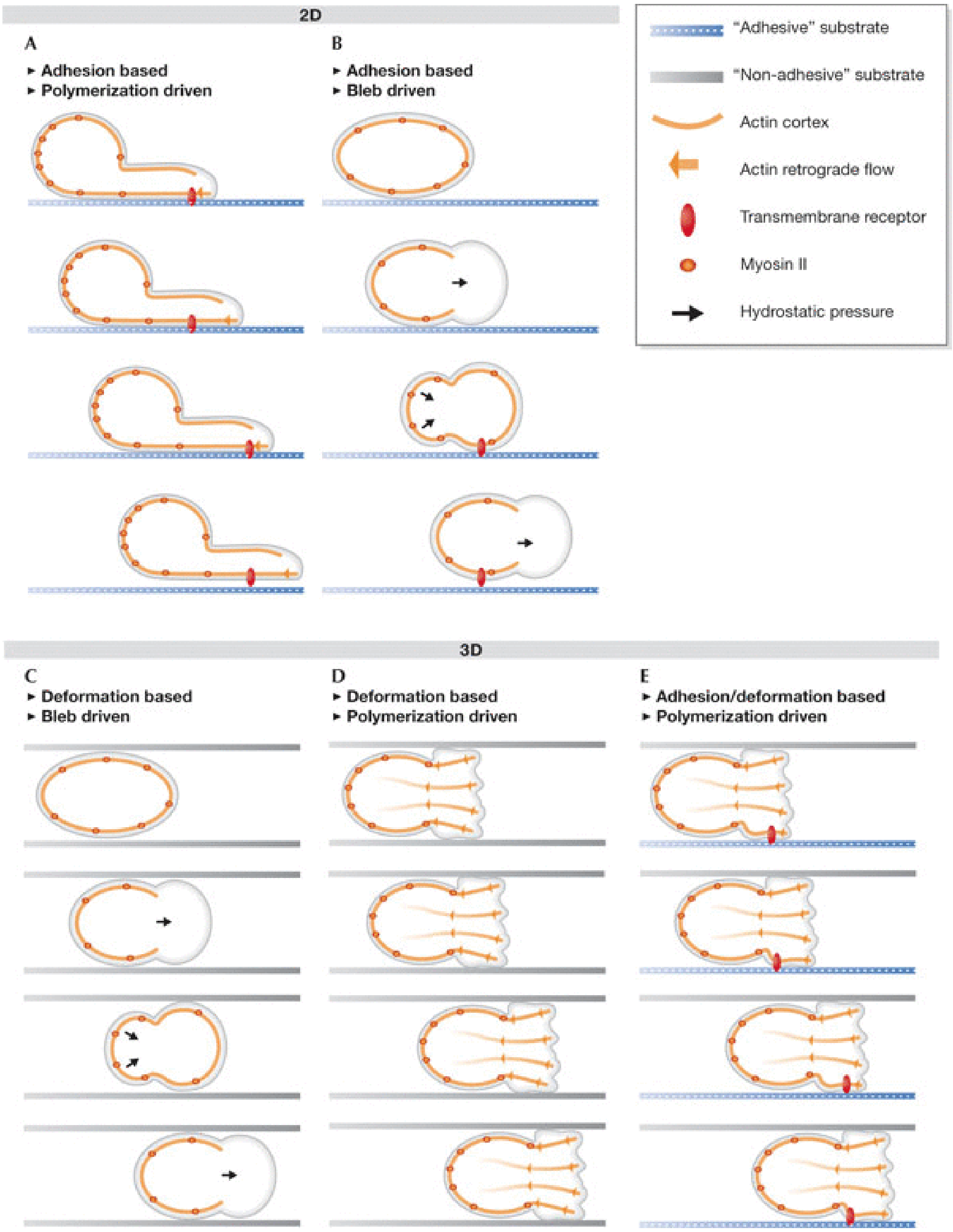

Figure 1-1. Comparison of migration strategies in two and three dimensional environments. A) 2D planar mesenchymal adhesion and polymerization based migration. B) 2D planar adhesion based bleb driven migration. C) Deformation based, bleb driven 3D migration. D) Deformation based, polymerization driven migration. E) Adhesion and deformation based, polymerization driven migration. Adapted from Renkawitz and Sixt , 2010 (6).

It has become imperative to develop new assays to probe the attributes of 3D migration as mounting evidence suggests that extrapolation from 2D data gives us an incomplete picture of 3D migration capabilities. Boyden chambers consisting of two fluid-filled chambers separated by a microporous membrane have been utilized to explore leukocyte chemotaxis (21). Various gel-based ECM's have been utilized to explore the effects of gel stiffness on migration speed (22), study the effects of changing porosity in both MMP-degradeable and MMP-nondegradeable gels on the limits of cell and nuclear deformability in confinement (23), and even to explore compartmentalized forward pressure changes driven by actomyosin generated pulling of the nucleus forward creating a piston-like effect (24). Cancer cells typically utilize confined interfaces between 3D tissue structures during single cell invasion to invade distant tissues (5, 25). Because GBM cells commonly migrate through confined spaces along white matter tracts and adjacent to blood vessel basement membranes, fluid saturated microchannels offer a reasonable replica of this natural environment where some of the geometric variables complicating 3D migration can be eliminated allowing more manageable observation and analysis. Consequently, microchannel devices bearing cross-sectional areas similar or smaller than cell dimensions are an intriguing choice to examine cell migration through these structures (4, 19, 25-29).

1.2.3 Microchannel derived migration assays for 3D analysis.

Because microfluidic devices are relatively easily manufactured and provide a reasonable reproduction of some 3D environments encountered by migrating cells, researchers have been utilizing these microchannels to explore migration in various cell types for some time now. Unfortunately, although these assays have yielded novel observations, there remains a lot of variability and ambiguity in the results probably due to the inconsistencies in cell types used, as well as differences in relative channel sizes, and even irregularities in stimuli application like the inclusion/exclusion of chemoattractants. The experimental variability in results and interpretations derived within 3D environments in the literature seems to support the notion that the confined 3D migration may be affected by a number of factors ranging from cell type to geometry to chemical environment to mechanical cues, and that cells can alter their strategy depending on these factors. The inclusion / exclusion of or variation in geometrical, mechanical, or chemical cues can thereby alter the response leading to ambiguous findings.

Cell migration in larger micro-channels reproduces a mesenchymal-like motion characteristic of 2D planar migration employing multiple different protrusive structures while attaching to multiple planes. but as channel dimensions decrease, cell length becomes increasingly persistent (19, 25). Under the influence of an externally applied chemotactic gradient, metastatic breast cancer cells will migrate through narrow channels even after inhibition of actin polymerization, Rho-Rock, myosin II-dependent contractility, or integrin binding (19, 25) suggesting either that the cells can switch between strategies or the cells employ a strategy independent of actin polymerization and myosin contractility. Interfering with microtubule (MT) dynamics in small confined channels (3 μm x 10 μm) reduces the net displacement in MDA-MB-231 cells dramatically by causing frequent directional changes, leading researchers to postulate that MT polymerization is involved in pushing the front edge forward in confined chemotactic migration (19). Similarly, osmotic shocks at the front or rear of the cell have been proposed as an alternate driving force in breast cancer cell migration under chemotactic influence (25). Research with chemotaxing HL60 neutrophil-like cells in confined channels suggests that cell migration may be induced by the interaction of two mechanically distinct F-actin networks in the cell. An adherent network is polymerized against the channel-wall interface and pushes toward the center of the cell anchoring a free network of F-actin as it polymerizes, pushing the leading edge forward (18). Irimia et al (2013) found that various human cancer cells will move spontaneously, even in the absence of an external gradient, when they are mechanically constrained in narrow channels (27). Furthermore, some of these cells would even migrate after inhibition of MT dynamics suggesting an actin/myosin based component. Dictyostelium will exhibit persistent migration in microfluidic channels characterized by an alternating left-right protrusion at the leading edge while exhibiting high actin density against the cell/wall interface suggesting an actin role in anchoring the cell (30). Again, the evidence suggests that cells are capable of employing any of a spectrum of migration strategies. The migration strategy adopted in any case seems to be a function of cell type, genetic transformation, porosity, confinement, and external stimuli (chemical, mechanical, etc.).

Actin and microtubule polymerization have been largely implicated in migration through confined channels, while actomyosin contraction has been ignored because experiments employing chemotactic gradients to artificially drive cell migration have indicated that myosin light chain kinase (MLCK) inhibitors (ML-7) and blebbistatin (dissociation of myosin and F-actin) do not lead to reduced velocities in confined cancer cells and may in fact lead to increased confined velocity (19, 25). Research in confined linear elastic gels with fibroblasts, however, suggests that actomyosin contraction can play a crucial role allowing the cell to guide the nucleus through confined spaces and creating compartmentalized pressure changes which help drive lobopodial protrusions (24). In addition, Wilson et al found that when arp2/3 nucleation of actin was perturbed, cells were still able to migrate but switched to a migration mode characterized by intense blebbing indicating a possible switch to a mode more dependent on actomyosin contraction(18).

Microfluidic rectangular channels categorized as either multi-planar 2D having cross sections larger than cell dimensions (15 μm^2) or fully confined characterized by cross sections small enough to force nuclear compression (5 μm^2) were utilized to explore GBM migration in different confined environments. GBM cells with fluorescently labelled F-actin or myosin were followed and imaged as they readily traversed channels in the absence of any chemotactic cues guided only by mechanical cues. The removal of chemotactic cues is critical as this eliminates a chemical stimulus which could possibly tip cells to a more polymerization dominant (actin or microtubules) migration strategy. Cells migrated readily through both channels, but the phenotype and corresponding migration strategy were dictated by the degree of confinement. Cells in larger channels exhibited protein distributions and migration styles similar to those observed in the 2D wells only extended to multiple planes. As confinement increased and cell nuclei were forced into compression, actin and myosin distributions began reorganizing with centralized actin maxima redeploying toward axial extremities resulting in high density localized regional protein hubs adjacent to both axial cell boundaries and minimum protein concentrations near the cell nucleus. The cells forced into nuclear compression moved along a spectrum of migration strategies bookended by one of two subtypes. One subgroup employed a more active front end (AFE), again mimicking a more mesenchymal form of motion. The second subgroup migrated in a quasi-steady length (QSL) state maintaining highly coupled almost linear front and rear movement while displaying intense blebbing at both axial boundaries. Because these cells are migrating in tight confinement without the usual cycles of protrusion and retraction at the front edge that accompany mesenchymal migration strategies, they make good candidates for employing possible alternative cell/substrate adhesion mechanisms. Because of the vigorous blebbing and the deviation from the typical protrusion-retraction cycles witnessed in mesenchymal migration, we hypothesize that the cells could be employing actomyosin contraction to generate transient localized pressure dependent anchorage to garner a temporary foothold for leverage, and to generate competitive pulling on the nucleus and cell interior to both maintain tension in the cell for mechanosensing, and give the cell a possible means of redirecting itself with minimal reorganization.

1.2.4 Numerical modeling

Using Comsol, we have constructed a 3D finite element model treating the cell as a biphasic material, to allow for separate tracking of the cytoskeleton and cytosol phases, where dynamic, experimentally derived actin and myosin distribution data can be coupled with governing equations to quantitatively predict the roles and interactions of forces (adhesion, polymerization, and actomyosin contractile forces) that drive complex 3D cell migration in the absence of specific cell-substrate binding. The model is unique in that it incorporates dynamic experimental data to drive complex temporally changing behavior. While previous models have used equations describing protein reaction kinetics or integrin binding kinetics to study migration, the current model is driven by experimentally obtained actin and myosin distributions. The model predicts that cells can utilize transient, actomyosin-driven, pressure-dependent anchors at the cells terminal ends derived from regional actomyosin foci to create a temporary frictional foothold to overcome friction due to nuclear push on the channel walls and enable the cell to migrate. In addition the model verified the importance of tensile homeostasis through an actively contracting coupling between opposite axial boundaries. We use the model results to hypothesize a migration mechanism utilizing actomyosin contractility and pressure based cell-substrate adhesion.

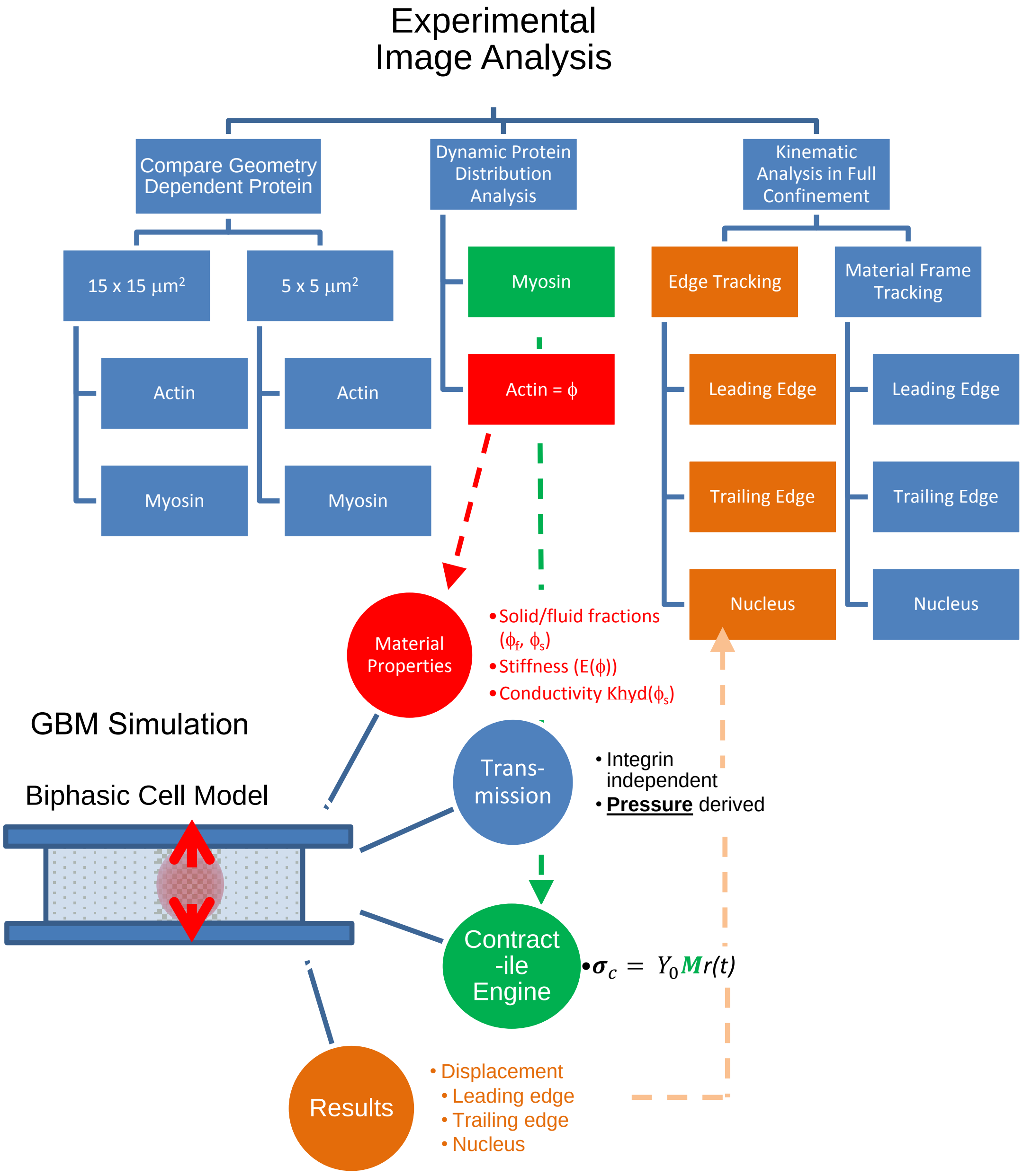

Figure 1-2. Flow chart outlining the integration of experimental results within the numerical model. Dynamic actin (red) and myosin (green) distributions are coupled through material coefficients (actin) and internally generated body stresses (myosin) to drive the simulation. Simulation derived displacements are then compared with experimental displacements for model validation

Chapter 2

Confined GBM Migration Analysis

2.1 Methods

Sampling and culturing of primary glioblastoma cells and selection of samples with confirmed presence of CD133+ were performed courtesy of the University of Texas Southwestern. The cancer stem cell hypothesis proposes that tumor growth is driven by a small subset of cancer cells within a tumor population having stem cell like features. These cells have an ability to self-renew and increased proliferative potential. CD133 is a cell surface marker thought to identify glioblastoma cells capable of initiating neurosphere growth and the formation of tumors upon transplantation into immune-compromised mice. Cells were labelled for actin using F-tractin transfection and for myosin II with EGFP- p-MLCII (31).

All images were provided courtesy of James Nyagilo at the University of Texas Southwestern Medical Center in Dallas. Imaging of CD133+ GBM cells was performed on an inverted microscope (Zeiss Axio Observer) using a 20x, 0.3 numerical aperture (NA) objective. EGFP constructs were excited using a 488 nm laser with an emission of 514 nm. Images were collected at 10 minute intervals.

To keep the cells viable we used an in-house designed chamber developed by 3D printing. The environment was kept at 5%:95% carbon dioxide to air ratio with greater than 95% humidity. To obtain the required gas mixture and humidity 100% carbon dioxide was mixed with air using an Ibidi gas mixer then pumped through water heated to 50^{o}C. The humidified gas mixture was then pumped through the chamber at 10 L/h. Using this method, cells could be kept viable in the chamber for up to 72 hours. Analysis of images was performed using ImageJ v 1.48 (National Institutes of Health, Bethesda, MD).

All Channels were provided courtesy of Loan Bui (Neural Engineering Lab, Dr. Young-Tae Kim) from the University of Texas at Arlington. Polydimethylsiloxane (PDMS (Dow Corning, Sylgard 184)) based microfluidic channels were fabricated using a soft lithography technique employing a 2 layer fabrication process whereby a device design was transferred via a mylar mask to a layer of negative photoresist (SU 8-5/SU 8-50) spin-coated on a dehydrated silicon wafer creating a patterned lithographic master onto which PDMS could be poured, cured, then peeled before being placed on a poly-D-lysine pre-coated glass coverslip yielding confined microchannels as outlined previously(32, 33). Microfluidic channel devices were designed as reported previously(33). Briefly, each device consisted of two wells (150 μm deep) created using punches (8 mm or 6 mm) joined by a series of microchannels coated with 10 μg/ml of laminin (Sigma-Aldrich) having one of 2 characteristic square cross sectional areas (CSA). Openings measuring 15 X 15 um^2 measured slightly larger than cell dimensions giving a 3D environment characterized by a migration path constrained to the axial direction where cells could employ multiple planar surfaces for attachment. Meanwhile, devices containing openings smaller than the nuclear spread measuring 5 X 5 um^2 were employed to force nuclear compression during migration.

2.2 Results

2.2.1 Protein distributions vary with mechanical confinement.

Lamin coated, PDMS, rectangular microchannels were utilized to first observe how GBM cell phenotype was affected under varying degrees of mechanical confinement. GBM cells with fluorescently labelled GFP labelled f-Tractin or myosin II-GFP were placed into reservoirs and allowed to enter PDMS channels having cross sections of either (15 μm x 15 μm) or (5 μm x 5 μm). The more expansive 15 μm channels bore cross sections that were larger than the characteristic GBM width presenting cells with a pseudo-2D environment where an invading cell could utilize multiple 2D planar surfaces for integrin specific anchorage but in which the cells never experience the steric normal confinement of smaller channels. 5 μm channels, however, bore cross sectional areas smaller than characteristic width of the GBM nuclei compelling the cells to squeeze and contract laterally particularly in the nuclear region. These assays were used to explore actin and myosin phenotypes in cells migrating in fully confined 3D tracts mimicking the those spaces around blood vessels or white matter tracts .

Cells entering 15 um channels utilized multiple walls to migrate while employing migration strategies and actin/myosin distributions similar to those seen on planar substrates. Fig.2.1 A is a snapshot of cells with gfp-labelled f-Tractin migrating though the entrance region of 15 μm channels. The left-handed side of the image is populated with a mass of cells that have pushed to the edge of the loading well nearing the channel entrances. These cells are still attached to the 2D planar substrate in the well and reveal actin distributions with maximum actin densities in the central nuclear region decreasing toward the cell periphery. Cells that have entered the channels (cell 1, cell 2, and cell 3) do not fill the channels. Instead, they tend to migrate along one or more surfaces (Fig. 2.1 A- cell 3 and cell 1) sometimes switching surfaces or using opposite distal extents (Fig 2.2 C) or extending branched pseudopods (Fig 2.2 B) to establish contact with multiple surfaces simultaneously. These cells utilize a variety of protrusions extended to multiple planar targets undergoing cycles of front end protrusion followed by pulling of the cell rear. Fig 2.1 C zooms to cells 1,2, and 3 as they migrate through the 15 μm channels. Actin intensities appear brighter in the central regions of the cells surrounding the nuclei. ImageJ was used to draw axial arcs beginning at one distal extremity, through the central region of the cell before ending at the opposite extremity. These curves were analyzed for normalized intensity indicating the relative local actin density (Actin*) and plotted along the normalized arclength (X*) in Fig. 2.1E. The intensity profiles indicate that the actin density peaks in the central, nuclear region of the cell as would be expected in a planar 2D environment.

A bird's eye view of GBM cells entering two 15 μm channels with gfp-labelled non-muscle myosin II (NMMII) is illustrated in Fig. 2.1 B. Much like the actin profiles, the myosin profiles appear to approach maximum density in the central, nuclear region of the cells and fade to minimum values at the periphery. Zoomed and cropped images (fig. 2.1 D) of cells 4, 5, and 6 further illustrate this nuclear-centric myosin weighting. Once again, arc lengths drawn using imageJ from one extremity to the opposite extremity through the nuclear center indicate that normalized myosin II profiles (Myosin*) reach peak densities in the central portions of the normalized arc-length (X*) corresponding with the nuclear region of the cell. Thus, the actin and myosin profiles in the semi-confined, pseudo-2D, multiplanar environment fit very closely what would be expected on a 2D plane. Furthermore, similarities in regional variations in the actin and myosin profiles point to a close correlation between local actin and myosin relative densities.

Cells migrating into 5 μm channels must find a way to squeeze the nuclear region laterally in order for the larger nucleus to fit within the smaller profile of the channel. Cells entering channels with small enough cross sections to force nuclear compression exhibit cytoskeletal protein distributions dissimilar to those witnessed within cells atop planar substrates or within larger channels. A snapshot of GBM cells entering 5 μm channels with gfp-labelled f-Tractin is shown in fig. 2.3 A. As the cells enter these more restricted spaces, the actin portion of the cytoskeleton undergoes a radical redistribution whereby the F-actin, which was more heavily centralized in the 2D and pseudo-2D channels, reshuffles toward the distal boundaries of the cell leaving an actin distribution heavily weighted at the poles. Zoomed images of individual cells (fig.2.3 B) show intensity peaks at the both axial poles of the cell with minimum intensity in the center of the cell surrounding the nucleus. Normalized actin profiles (Actin*) taken along a normalized axial midline (X*) drawn from one end of the cell to the opposite end using ImageJ as illustrated in Fig. 2.3 C confirm that actin densities peak in highly localized hubs near each of the axial termini of the cell before diminishing abruptly toward the cell interior. Thus as cells enter fully confined environments forcing nuclear compression, the actin distribution in migrating GBM cells transforms so that peak actin densities reorganize, drifting from a centralized nuclear localization toward localized hubs near the cellular axial boundaries.

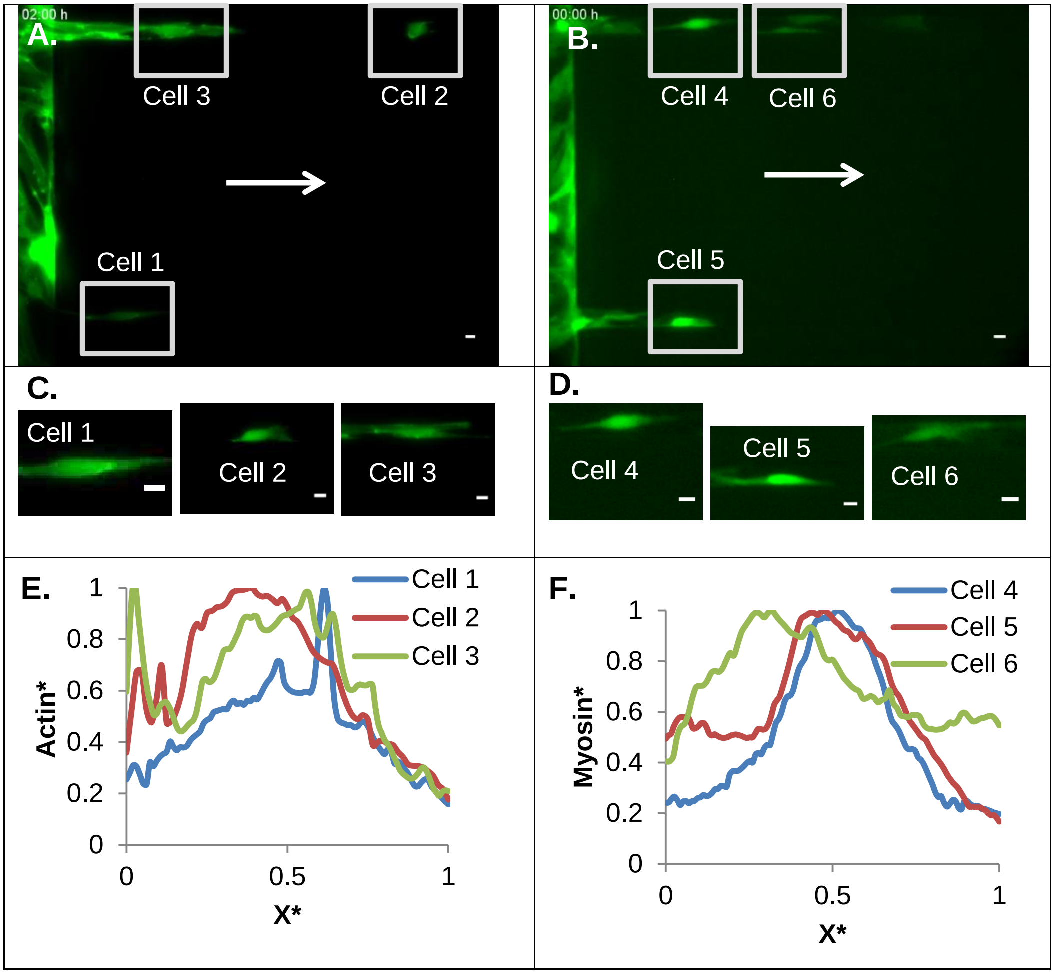

Figure 2-1: GBM cells migrating through 15 μm channels exhibit protein distributions similar to planar 2D. (A, C, E) illustrate GBM cells with gfp-labelled F-tractin while (B, D, E) indicate cells having labelled myosin (myosin II-gfp). Zoomed images of cells labelled for C) actin or D) myosin show brighter intensities in the centralized nuclear region of the cell indicating a nuclear-heavy protein distribution. Normalized intensity data captured using ImageJ along normalized arclengths (X*) drawn from one extremity to the opposite through the center of the cell affirm that both (E) actin and (F) myosin densities peak in the center of the cell and fade to a minimum at the cell periphery.

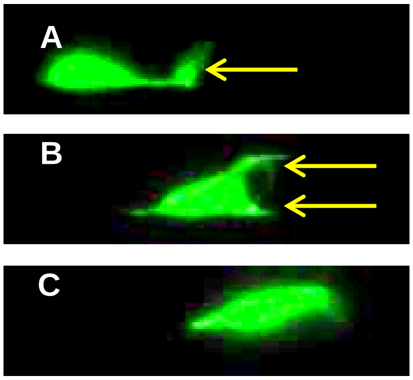

Fig. 2-2: Multiplanar migration in a 15 x 15 μm^2 channel. GBM cells with labelled F-tractin migrating though a 15 μm^2 channel move similar to 2D migration with multiple protrusive structures and can either A) migrate along a single 2D planar surface, or use B) branching pseudopodia or C) opposite distal extents to establish contact with multiple surfaces.

In addition to changes in the actin distributions, GBM cells entering confined environments under nuclear compression exhibit a concomitant reorganization of their myosin II distributions. Fig. 2.3 D reveals multiple GBM cells with myosin II-gfp entering 5 μm channels from a 2D planar holding well. Cells within the channels demonstrate higher fluorescent intensities near the localized regions adjacent to the axial ends of the cells. Zoomed images of individual cells migrating in fully confined spaces in fig 2.3 E reaffirm the presence of intensity peaks adjacent to both termini of the cells with minimum intensities in the central locales. Normalized intensity measurements plotted vs normalized axial location (X*) taken along an axial centerline in fig 2.3 F reasserts that myosin redistribution in these fully confined channels follows an identical pattern to that of actin. Namely, the myosin is reorganized so that the central maxima in cells on 2D planar surfaces shuffles to the cell's axial boundaries leaving distributions with peaking densities in regional hubs near each of the cells axial bounds and minimum values near the cell's center.

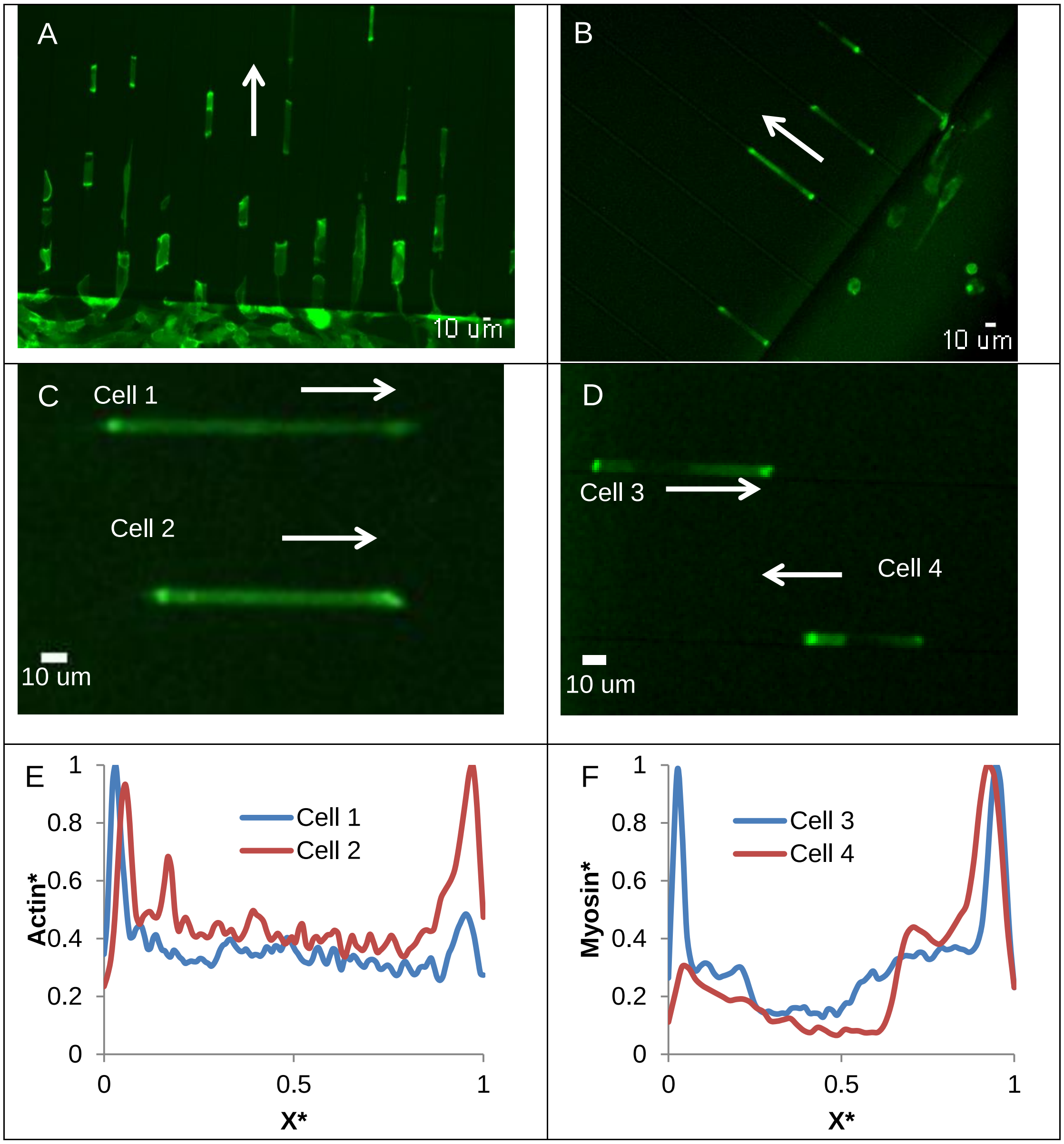

Fig. 2-3: Protein distributions in full confinement. GBM cells entering 5 μm channels with fluorescently labelled A) actin or B) myosin reveal unique confined protein distributions. Zoomed images of cells with labelled C) actin or D) myosin II along with axial normalized intensity plots of E) Actin* and F) Myosin* indicate the transitioning of both distributions away from centrally dense localization toward localized hubs near both of the cell's axial poles

2.2.2 *Kinematic studies reveal at least two distinct confined migration strategies*.

At initial glance, cells seem to employ a myriad of migration strategies. A closer look at cells migrating independently suggests that cells migrating individually in response to mechanical confinement alone can employ at least two distinct migration strategies either exclusively or in some combination. In order to explore cell migration, cells with gfp labelled cytoskeletal components (f Tractin or myosin II) were tracked while navigating through 5 μm channels. ImageJ was used to simultaneously track the most distal portions of the leading and trailing edges of the cells relative to a motionless datum in order to help explore the mechanism of migration. The relative displacement of each edge was calculated by subtracting the initial positions of the leading and lagging edges from the current cell position (front and rear). In each case, the front and rear edges were defined as the most distal point on the cell extremity. Only cells that migrated independently for significant time periods, without spending time entering or exiting channels, and without contacting adjacent cells were followed. In addition cells were only tracked when a clear channel marker (imperfection or edge) was present to establish a datum. Although, these conditions severely limited sample sizes, the intent was to avoid entrance effects and possible paracrine signaling effects that might alter migration strategies or protein phenotypes.

Fig. 2.4 (A-E) is a collection of time varying plots of displacement of the front (red) and rear (blue) edges of cells moving through fully confined channels (5 μm) in addition to the normalized length (black dashed) defined as the current cell length / the initial cell length. Data were collected at 10 minute intervals over collection periods approaching 4 hours. Average speeds of the front and rear edges of all cells over the entire period were calculated and are indicated in the plots. It is immediately apparent that cells can be grouped into one of two subsets based on both the average velocity of the edges and the relative movement between the front and rear edges. In cells 3, 4, and 5 (fig. 2.4 C-E) the displacement at the leading edges tends to lead the displacement at the rear and the leading edge tended to oscillate more frequently, undergoing periods of protrusion at the leading edge followed by contraction backward. This in turn resulted in oscillations in the cell stretch ratio. These cells frequently had stretch ratios higher than 1 indicating cellular elongation. Both edges routinely traveled at higher velocities than the second subset of cells achieving average speeds approaching 19-23 μm/hr. These active front end (AFE) migrators thus had frequent length oscillations and traveled at higher speeds than their counterparts. The AFE designation was used because while these cells do at first glance seem to employ a mesenchymal-like scheme, protein distributions do differ from the classical 2D planar archetype and previous literature does suggest the possibility of integrin free adhesion even in this subtype (19).

Cells 1 and 2 are representative of a second subset of cells termed quasi-steady contractile (QSC) migrators. These cells were characterized by rear edge displacements that typically exceeded displacements at the leading edges. The leading edges of these cells were less active than those in active front cells. Larger displacements at the trailing edges of these cells indicated that the rear edges had moved closer to the leading edges suggesting that these cells migrated in state of steady contraction. After initial contractions, both edges tended to migrate forward linearly maintaining more stable, contracted cell stretch ratios while both edges moved with fairly constant velocities. Whereas, the stretch ratios in active front end cells tended to protrude and retract over shorter time periods anywhere between 10 – 50 minutes, the stretch ratios in these steady contractile migrators cycled between protrusion/retraction over longer time periods of 100 minutes or longer, typically maintaining stretch ratios less than 1. Cell 1 (fig 2.4 A) began contracting at around t = 20 mins as the front end displacement slipped behind the rear end displacement. The cell continued a slow contraction as the gap between displacements slowly increased up until around 100 mins at which point the front/rear displacement gap began to narrow as the contraction relaxed and the cell returned to its initial length. Cell 2 showed a contractile burst between about 10 and 30 mins again as the rear displacement catapulted ahead of the leading edge displacement. This contraction peaked then held steady throughout the remainder of the experiment as the cell began to slide forward maintaining a steady normalized length. These QSL migrators marched at a slower pace than the active front cells described above. Limited observations showed cells achieving average velocities in the neighborhood of 9-11 μm/hr. These steady contractile movers, thus, initially underwent contraction before sliding at a relatively steady length at steady average speeds that were only about half as big as those achieved in the active front cells.

To reiterate, GBM cells moving in confined environments under nuclear compression seem to be able to navigate using a spectrum of migration styles delimited by 2 extremes (active front end migrators, steady contractile migrators) which can be distinguished by their relative speeds of migration, and the magnitude and periodicity of changes in the cell length. Furthermore, cells do not appear to be locked into a single strategy but can sometimes mix or completely alter strategies.

To further explore any localized geometrical cell changes, two representative cells, one from each migration subtype, were chosen to explore localized deformation in a moving reference frame. By removing each cell's translational component, relative front and rear compartmental changes could be explored. Each cell's domain and nuclear compartments were traced as separate regions using ImageJ at each time-point. These outlines were then rearranged and positioned vertically so that the axial position of the trailing edge of the nucleus was aligned in each frame to give a relative time-dependent map of the regional cellular changes (front, nucleus, rear) as the cell moved.

The outlined cell and nuclear compartments at each of the time points in an active front-end migrator are illustrated in fig 2.5. The dynamic compartmental deformation history (arranged vertically for comparison) is provided along with the plots of the displacement at the leading edge, trailing edge and nuclear centroid for comparison. Any changes in nuclear shape were small and difficult to discern possibly because the nuclear envelope is not explicitly observable but is interpreted from the images. The displacement plots shown in fig. 2.5 indicate that there was very little separation between the displacement of the trailing edge (blue) and the displacement of the nuclear centroid (green). This suggested that as the cell moved forward and the leading membrane pushed forward then back, the rear of the cell and the nucleus were coupled more tightly as they slid forward. This might be achieved by a dynamically changing front compartment and a more static rear compartment as the cell moves. The compartmental deformation history given in fig. 2.5 confirms this. The rear compartment changes comparatively little remaining relatively stable over time. Only a small contraction between 70 and 130 mins is indicated by the compartmental deformation history. The front compartment on the other hand changes dynamically expanding for 20 minutes before contracting again between 20 and 40 minutes.

The forward compartment continues this cycle of expansion and contraction over the remaining time steps. Thus, the compartmental deformation history indicates a cell moving forward with a relatively stable rear compartment (in size) and a cyclically expanding-contracting leading compartment. This cell has a very active front end that protrudes away from the nuclear compartment before being retracted. This cycle of leading edge protrusion and front compartment expansion followed by leading edge retraction and front compartment contraction is repeated over and over. The vertical map highlights the drastic decoupling between the front and rear compartments in the AFE migrator. This decoupling suggests multiple regional engines driving the migration and is highly reminiscent of 2D mesenchymal strategies.

The outlined cell and nuclear compartments at each time point in a QSL migrator are illustrated in fig 2.6. Again, the dynamic compartmental deformation history (arranged vertically for comparison) is provided along with the plots of the displacement at the leading edge, trailing edge and nuclear centroid for comparison. Once again, the deformation plots show tightly matching rear edge and nuclear movement over time suggesting highly coupled nuclear and rear edge movement. The compartmental deformation history suggests that there is little change in the size of the rear compartment as the cell marches forward. The front compartment in this case is much less decoupled from changes in the rear, but the majority of contraction is achieved in the leading compartment while the rear compartment maintains a more steady size. So while decoupling between edges was less obvious in the QSL migrator it was still evident in the asymmetric compartmental changes. This asymmetry in the compartmental deformation history again suggests that migration was either achieved utilizing multiple localized engines or as a consequence of regional dissociation.

2.2.3 *Protein distribution differences between subtypes suggest different mechanisms at the leading edge.*

Like the kinematic analysis, dynamic axial protein distributions (actin and myosin II) collected at each time step in migrating cells suggested that indeed there were at least two different migration phenotypes based on distribution dissimilarities between cells. Axial protein distributions were collected from fluorescent images using imageJ to plot the normalized fluorescence intensity (actin and myosin II) data along a cell's axial centerline beginning at the rear edge of the cell passing to the leading edge. Fig 2.7 illustrates transient axial actin profiles taken in an AFE migrator every 10 mins for 60 mins along with a combined graph of all profiles. The data clearly indicate a highly localized actin concentration peak adjacent to the rear of the cell at each time step. The actin distribution falls to a minimum at the center of the cell and there is a more diffuse smaller peak that swells and fades adjacent to the leading edge. In the AFE migrator the actin has been redistributed to the poles, but while there is an identifiable regional peak near the rear edge, the front is less obvious and more diffuse. For comparison, the axial actin distributions (fig 2.8) taken at 10 min intervals for 60 mins in a QSL migrator indicate highly localized, stable peaks adjacent to both the trailing and leading extremities. Note in the combined plots that the changes near the maxima adjacent to the edges are somewhat subtle. The peaks tend to center around the same location with approximately the same relative heights. Clearly there are changes in the spatial gradient in these regions however. Thus it appears that cells may be able to adjust speed and direction with relatively small regional protein adjustments to change relative regional contraction strength. The only exception to this is near the leading edge in the AFE migrator where there is more variability among the dynamic distributions probably resulting from the more pronounced cycling between protrusion and retraction in this region.

The axial myosin II distributions plotted in AFE migrators (fig 2.9) and QSL migrators (fig. 2.10) follow similar patterns to that observed with actin. In the AFE migrators, the highly localized regional maximum is again associated with the rear of the cell. Once again there is a more diffuse peak that swells and fades much like was the case with actin. QSL migrators show highly localized maxima near both the rear and leading edges that are relatively stable.

To summarize, in AFE migrators actin and myosin II are redeployed to highly localized maxima adjacent to the cell's axial boundaries. Deployment to the rear results in a steady, conserved, highly localized peak while deployment to the leading edge results in a more diffuse peak that grows and fades dynamically as the front end cycles between protrusion and retraction. QSL migrators show protein deployment to steady, conserved, highly regionalized peaks at both the trailing and leading edge of the cell. The strengthening and waning in the leading edge protein distribution associated with protrusion and retraction cycles is no longer evident in the QSL migrator. The protein distribution dissimilarities between migration subtypes reaffirm that the cells may use multiple migration tactics depending on the migration phenotype.

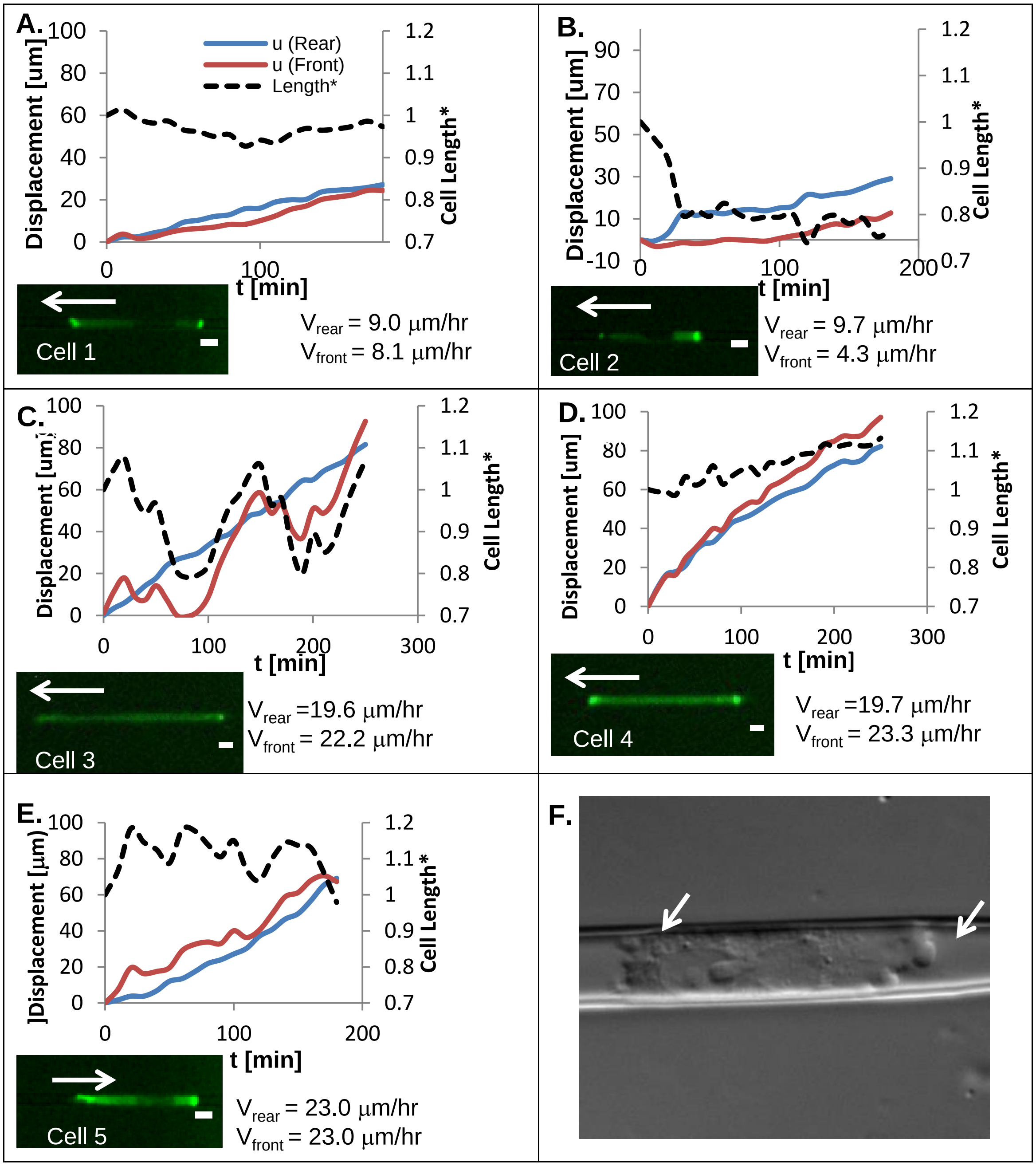

Fig. 2-4: Kinematic confined cell analysis. A-E) Plots of displacement of the leading (red) and lagging (blue) edges of GBM cells migrating through 5 μm channels. Bar = 5 μm. F) DIC image of GBM cell navigating a 5 μm x 10 μm channel clearly showing active blebbing at both ends of the cell.

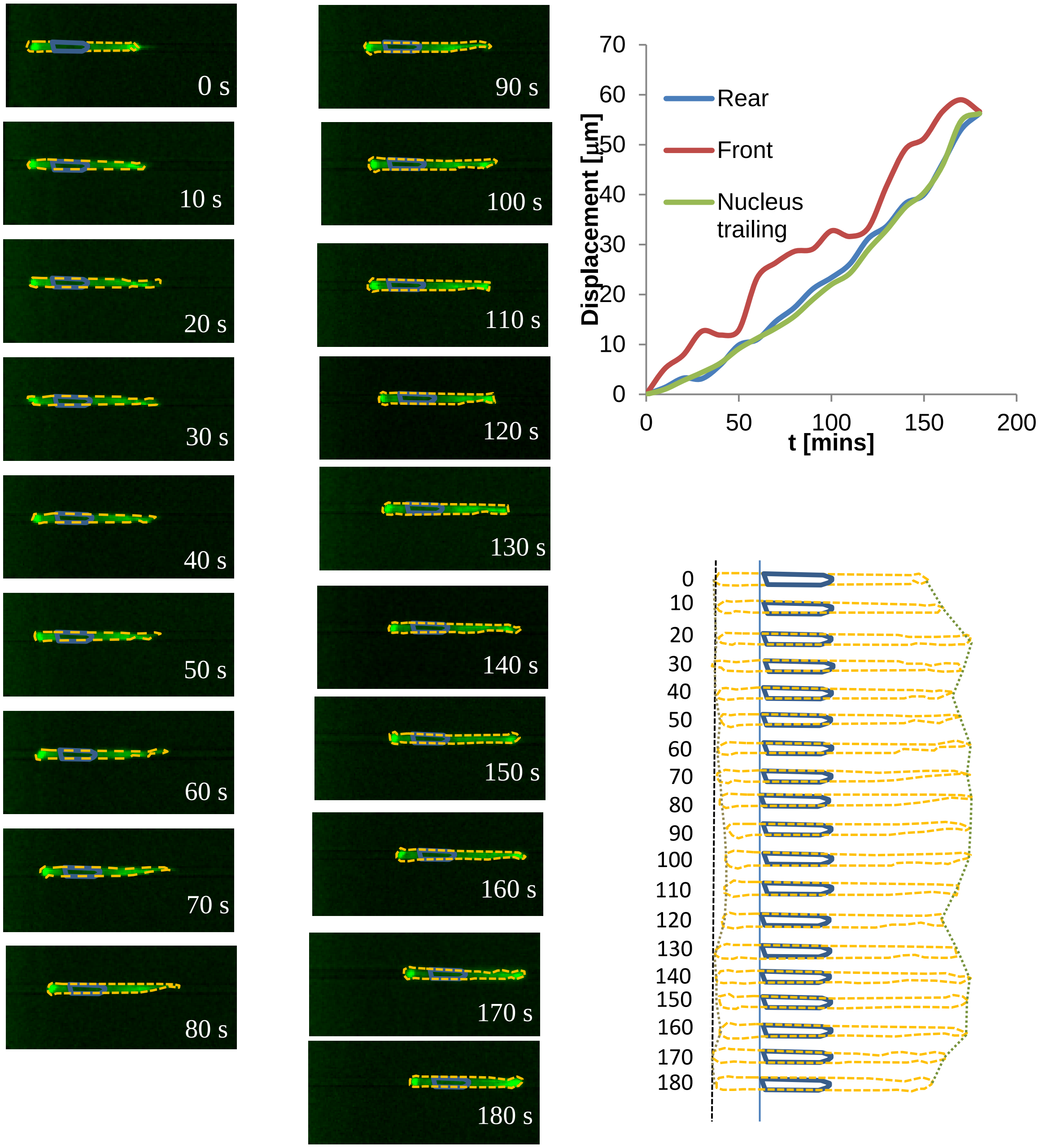

Fig. 2-5. Dynamic compartmental deformation analysis in an AFE migrator. A) Dynamic outlines of cell (orange dashed) and nuclear (blue) domains in an active front end GBM migrator (cell 1). These regional outlines were arranged vertically by time, lining up the axial position of the back end of the nucleus to illustrate the relative regional deformation while removing the overall translation of the cell. Expansion of the front and rear in this cell are highly decoupled suggesting multiple motors to drive migration.

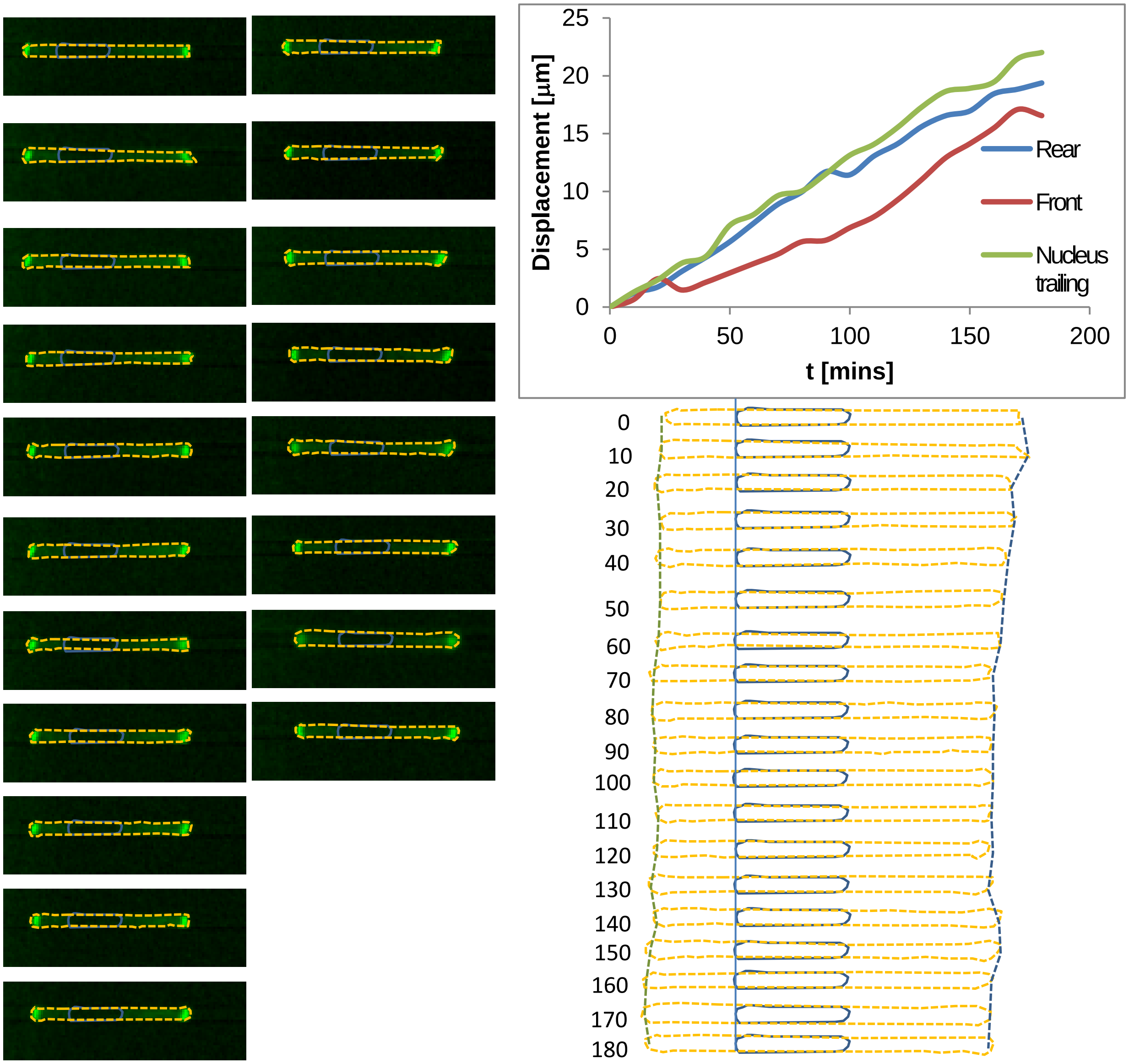

Figure 2-6: Dynamic compartmental deformation analysis of a QSL migrator. A) Dynamic images of a steady contractile GBM migrator (cell 2) were utilized to outline the cell and nucleus for a closer look at cell migration in confinement. Cell outlines were copied and arranged vertically by, time lining up the axial position of the back end of the nucleus to illustrate the relative deformation within each compartment (front and rear) of the cell at various time points. This cell moves in a steady state of contraction.

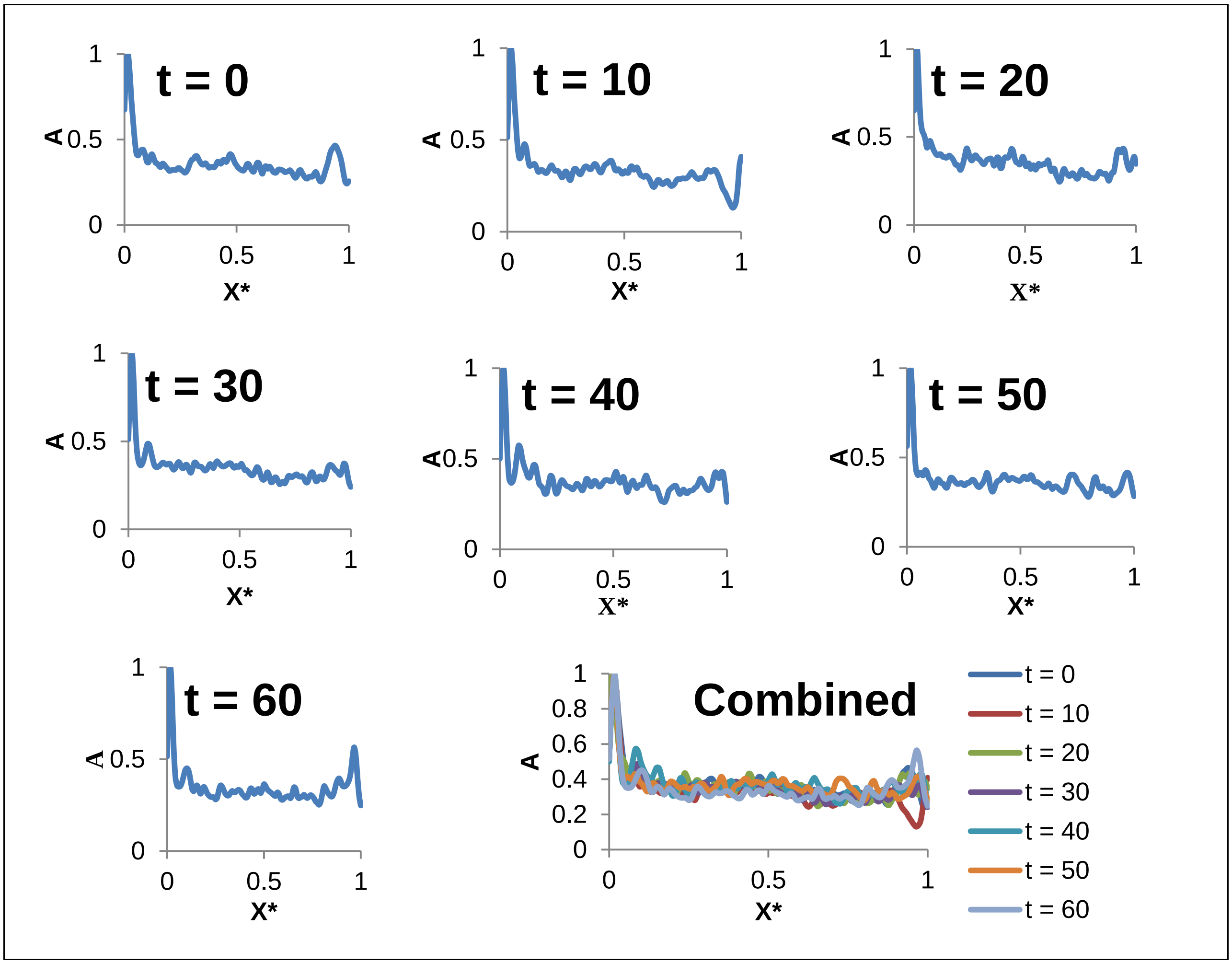

Figure 2-7. Dynamic axial actin profiles (every 10 mins) in an AFE migrator. Actin distributions are relatively stable particularly at the rear edge. Actin distributions spike near the rear axial pole and are more diffuse near the front of the cell spiking slightly at some time periods (0 mins, 60 mins). Actin density variation is greatest near the leading edge indicating polymerization and retraction cycle.

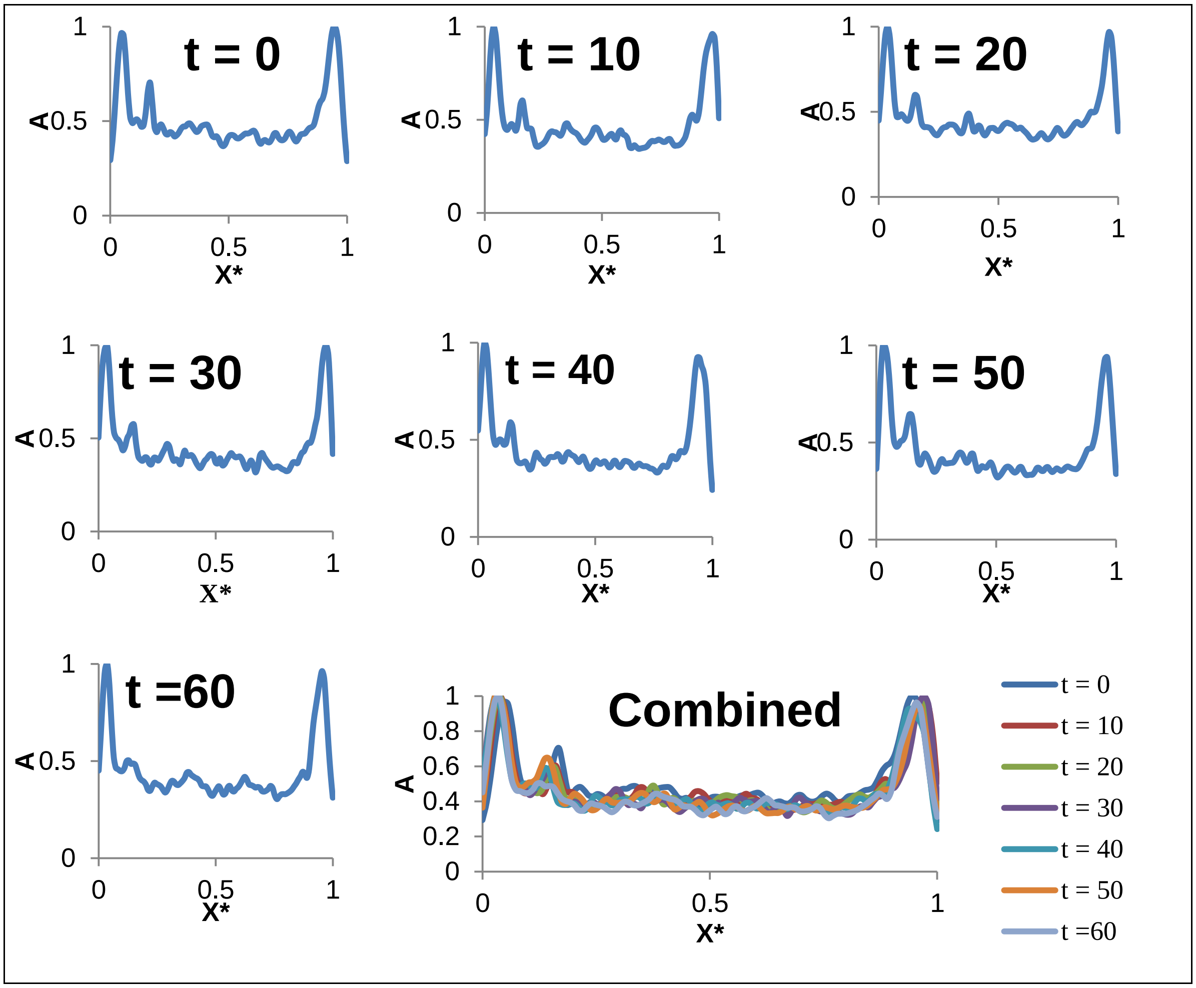

Figure 2-8. Dynamic axial actin profiles (every 10 mins) in a QSL migrator. Actin distributions show only localized changes but remain relatively steady. Actin density maxima are localized near both axial boundaries with minimum values in the center of the cell.

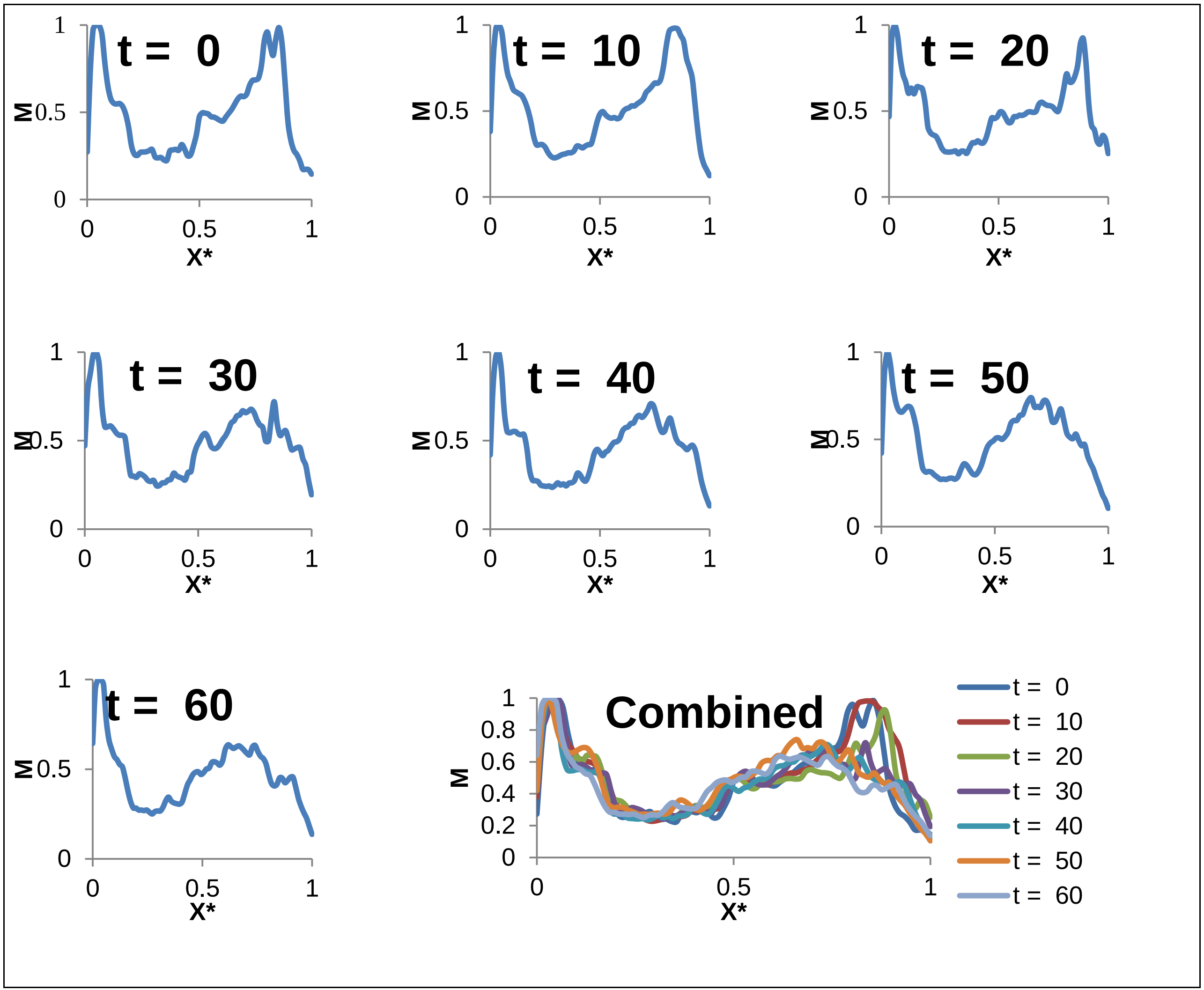

Figure 2-9. Dynamic axial myosin profiles (10 mins) in an AFE migrator. Myosin peaks remain relatively stable near the rear edge. Myosin densities near the front are more variable as the peaks cycle between highly localized taller peaks and short broader peaks. Myosin densities are, again, minimal in the central cell region.

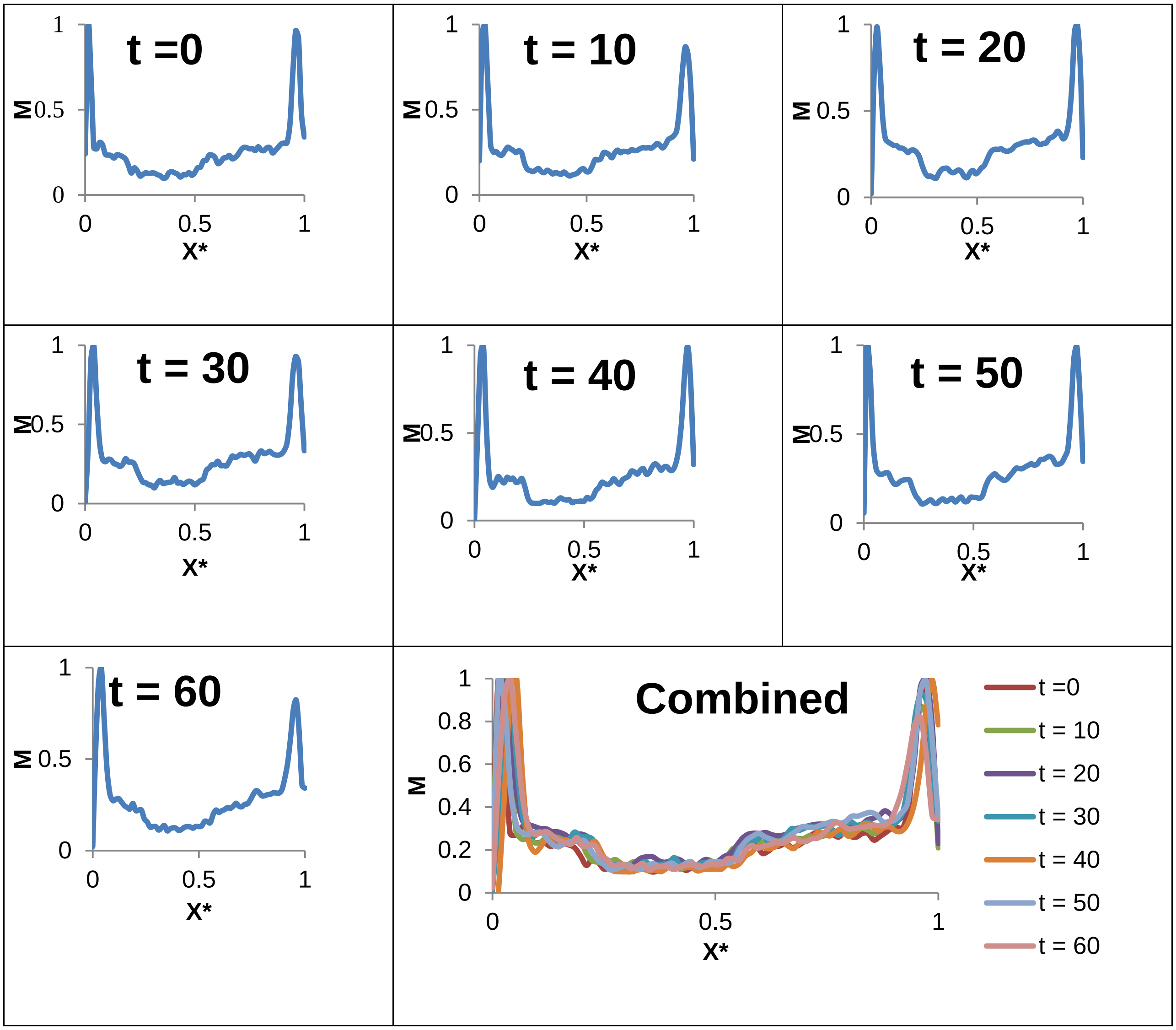

Figure 2-10. Dynamic axial myosin profiles (every 10 mins) in a QSL migrator. Myosin density maxima are localized near both axial boundaries with minimum values in the center of the cell. Myosin distributions show only localized changes but remain relatively unchanged.

Chapter 3

Computational Model

3.1 Background.

GBM migration in confined channels under conditions forcing nuclear compression (5 x 5 μm^2) resulted in 2 migration phenotypes (AFE migrators or QSL migrators). Whereas AFE migrators showed frequent protrusion and retraction cycles at the leading edge similar to multi-planar 2D migration, QSL migrators moved with relatively stable cell lengths and more temporally steady protein distributions while persistently blebbing vigorously at both axial boundaries. The lack of protrusion-retraction cycles in QSL migrators seems to suggest an alternative mechanism to the typical integrin driven grip-pull-release process witnessed in planar mesenchymal cells. Evidence pointing to a loss of integrin dependent adhesion in these channels in some cell types seems to reconfirm this possibility (19, 25). Whereas specific substrate gripping would seem crucial to allow force transmission to the substrate when cells are traveling on a 2D plane, cell confinement opens new possibilities for cell-wall force transmission through the utilization of either polymerization or pressure driven normal forces which could create transient friction based anchorage. Distal localized actin and myosin hubs and persistent vigorous blebbing in QSL migrators suggested that cells might be employing dynamic pressure buildup and diffusion to establish transient adhesion within the channels. In addition previous research with C6 and U87 human glioma cells migrating through narrow channels in the absence of any externally applied gradients showed cell line dependent (U87) decreases in cell and nuclear movement under the influence of blebbistatin suggesting actomyosin dependence in some cell lines (34). An FEA model was developed using COMSOL Multiphysics to explore the compatibility of dynamic pressure derived cell/substrate adhesion with observed QSL protein phenotypes.

Deriving tractable computational models to explore cellular motility encompasses key challenges. Models must integrate distinct biological, chemical, thermal, and mechanical phenomena that occur over length and time scales that can vary over several orders of magnitude. Once more, models must address the development of appropriate continuum material descriptions of complex, heterogeneous, locally distinct cellular environments. Perhaps the key burden in developing a useful model is simplifying the vast complexity into a few manageable core components that capture enough of the seemingly infinite interconnected cell processes involved to adequately describe the migration phenomenon. While the scope of the model can vary from targeted models like those characterizing actin forces at the leading membrane based on polymer kinetics and diffusion to global or whole cell models, a global cell approach seems appropriate in this case to examine cell migration (10, 11, 15).

Researchers have developed variety of strategies for modeling the cellular environment that have increased in complexity over time. One of the early models developed treated the cell as a group of linked discrete viscoelastic elements. This model was utilized to predict that asymmetry in cell adhesion was necessary to drive planar migration with higher binding affinity in the front of the model (35). Cells have been simplified as fluid filled vessels or treated as elastic films (36). Some researchers have chosen to capture complex cytoskeletal character using continuum viscoelastic models to capture the characteristic energy storage and loss attributes of the cytosol (37-40). While these viscoelastic models capture the mechanical responses of the cell very well, they lack the ability to track separate solid and fluid phases when this information becomes important. To this end, researchers began adopting multiscale, multiphase approaches to independently track fluid and solid phases within the cell (41-43). Early multiphase approaches often combined separate Eulerian fields to describe phase movement with phase interaction terms to couple the phases. Experimentally, it has been argued that the cellular space behaves as a poroelastic medium with independent cytosolic fluid streaming through solid polymer fractions with rates depending upon the characteristic conductivities dictated by the fluid viscosity along with the geometry and density of the solid fractions (44, 45). Consequently, some later modeling works have treated the cell as a poroelastic or biphasic continuum composed of independently moving solid and fluid volume fractions that interact through momentum exchange (46-49).

Much of the modeling effort to date has focused on migration on 2D planar platforms. Modeling work in 3D environments is lacking due the increased complexity of cell behavior. Hawkins et al (2009) developed a 2D viscoelastic model of a confined cell treated as a polymerizing gel strip that achieved migration through polymerization driven interaction with the wall (39). Modeling cell behavior in confined microchannels provides some of the complexity 3D migration with the added benefit of reducing the degrees of freedom in the model. The steady migrating lengths maintained during QSL migration indicates that cell-channel interactions may be driven by an integrin independent mechanism in these cells. The lower speeds of QSL migrators (compare to AFE migrators) could support lower binding affinity with the channel and perhaps a more efficient migration mechanism when the cells are not faced with more extreme migration resistance possibly resulting from nuclear recoil against the walls. Once more, the steady protein profiles in QSL migrators combined with vigorous blebbing witnessed in these cells suggests that polymerization may be less of a factor in achieving cell-wall frictional anchorage than in AFE migration where protein distributions differ dynamically at the leading edge. Instead transient dynamic pressure hubs might be important for developing temporary frictional anchorage. This would allow a natural asymmetry in the cell-substrate force transmission. To explore the possibility of dynamic localized pressure-driven adhesion to drive GBM migration in confinement we have developed a numerical model adopting a biphasic framework to allow independent phase tracking allowing regional contraction-driven pressure transients to drive cell-channel anchorage. Furthermore, this model is driven by dynamic experimentally obtained protein distributions to predict complex cell behavior over long time scales.

The biphasic framework treats the cell as uniform sponge-like, poroelastic material and assumes that the cell is composed of a traditional linear biphasic polymeric solid cytoskeleton saturated in a fluid cytosolic phase. Traditional linear-biphasic equations have been adopted and modified to include terms to account for pressure derived adhesion forces and actomyosin driven contractile forces. One of the key objectives in the modeling effort was to incorporate the QSL migratory phenotype into the simulation by including experimentally derived actin and myosin data to respectively define the material characteristics (solid volume fraction, stiffness, and permeability) as well as drive the localized contractile engine. Leading and trailing edge displacements and velocities predicted by the simulation could then be compared to experimentally derived values to validate the model. Parametric studies were included to explore how changes in the contractility parameter, representing increased contractility or blebbistatin inhibition, or nuclear adhesion parameter, perhaps in response to lamin A downregulation, affected cell migration.

3.2 Modeling approach

3.2.1 Governing equations.

COMSOL 4.3a was utilized to develop a 3D, biphasic, finite element framework to numerically explore how the dynamic, experimentally driven QSL migration phenotype could employ a pressure derived cell-substrate adhesion to elicit confined migration.

Continuity: The governing equations were derived assuming that a scale is adopted which is small enough that any inhomogeneities in cell material properties can be ignored within a single tiny representative element volume where material properties are represented by microscopic average quantities that remain constant when the volume element is small enough. We begin by assuming that every point in the bulk material is saturated by a combination of fluid (*f*) and solid (*s*) volume fractions (ϕ). Each of these phases is assumed to be incompressible.

$$\varphi_s + \varphi_\mathrm{f} = 1 \tag{1}$$

Conservation of mass is described by the fluid and solid continuity equations (Equations 2 and 3) where $\boldsymbol{v^f}$ represents the fluid velocity, $\boldsymbol{u}$ is the displacement of the solid cytoskeleton, and $\boldsymbol{\nabla}\cdot$ is the divergence operator. Any changes in the specified volume fraction over time (1st term LHS) result from either transport of the phase in/out of the control volume (2nd term LHS) or as a result of polymerization/depolymerization (ψ_P). These equations can be combined to give a combined continuity equation (Eq. 4).

$$\frac{\partial\varphi^f}{\partial t} + \boldsymbol{\nabla}\cdot\left(\varphi^f\boldsymbol{v^f}\right) = -\psi_P \tag{2}$$

$$\frac{\partial\varphi^s}{\partial t} + \boldsymbol{\nabla}\cdot\left(\varphi^s\frac{\boldsymbol{\partial u}}{\partial t}\right) = \psi_P \tag{3}$$

$$\boldsymbol{\nabla}\cdot\left(\left[\varphi^f\boldsymbol{v^f} - \varphi_f\left(\frac{\boldsymbol{\partial u}}{\partial t}\right)\right] + \left(\frac{\boldsymbol{\partial u}}{\partial t}\right)\right) = 0 \tag{4}$$

Momentum: Darcy's law (Eq. 5) describes the relative movement of each of the phases as proportional to the product of the gradient of the pressure (P) and the hydraulic conductivity (K). Darcy's law (eq. 5) can be substituted into the combined continuity equation (Eq. 4) to give the pressure diffusion governing equation (Eq. 6) which indicates that any expansion or contraction of the csk are balanced by pressure diffusion through fluid redistribution. The hydraulic conductivity (K) determines the relative ease with which the fluid phase flows through the porous solid csk phase. Thus a smaller K value leads to slower pressure equilibration in the model through fluid rearrangements; thereby resulting in longer maintenance of local deformation-driven pressure gradients within the model.

$$\left[\varphi_f\left(\boldsymbol{v_f}-\left(\frac{\partial \boldsymbol{u}}{\partial t}\right)\right)\right]=-K\boldsymbol{\nabla}P \tag{5}$$

$$\boldsymbol{\nabla}\cdot\left(K\boldsymbol{\nabla}P\right)=\left(\frac{\partial \boldsymbol{u}}{\partial t}\right) \tag{6}$$

Stress equilibrium: Each of the phases maintains a stress component. The fluid and solid portions of the stress are outlined in Eq. 7 and eq. 8. The fluid stress contribution is dictated entirely by the local fluid portion of the pressure, whereas the stress carried within the solid csk comes from a combination of the solid portion of the pressure, the passive elastic stress ($\boldsymbol{\sigma_e}$), and the contractile stress ($\boldsymbol{\sigma_c}$) generated from actomyosin. In the QSL simulation the polymerization stresses are ignored as the experimental data seems to suggest fairly steady protein profiles adjacent to the edges.

$$\boldsymbol{\sigma_f}=-\varphi_f p\boldsymbol{I} \tag{7}$$

$$\boldsymbol{\sigma_s}=\boldsymbol{\sigma_e}-\varphi_s p\boldsymbol{I}+\boldsymbol{\sigma_c} \tag{8}$$

The solid *csk* is considered to be linear elastic (Eq. 9) with ∈ indicating the strain tensor.

$$\boldsymbol{\sigma_e}=\lambda(\boldsymbol{\nabla}\cdot\boldsymbol{u})\boldsymbol{I}+2\mu\in\text{, given}\qquad \in=\frac{1}{2}\left((\boldsymbol{\nabla u})+(\boldsymbol{\nabla u})^T\right) \tag{9a}$$

λ and μ denote Lame's constants which characterize the mechanical properties and can be related to the Young's modulus (E) and Poisson ratio (v) as

$$\lambda=\frac{Ev}{(1+v)(1-2v)},\quad \mu=\frac{E}{2(1+v)} \tag{9b}$$

Eq. 7 and eq. 8 can be added to give the combined stress constitutive equation.

$$\boldsymbol{\sigma} = \boldsymbol{\sigma_e} - p\boldsymbol{I} + \boldsymbol{\sigma_c} \tag{10}$$

The stress equilibrium equation (Eq. 11) is a derivative of Newton's 2nd law and asserts that any changes in the state of stress within a control volume (LHS) are a consequence of the application of internal and external forces (RHS).

$$\boldsymbol{\nabla} \cdot \boldsymbol{\sigma} = F_{adh} \tag{11}$$

Substituting the Eq. 10 into Eq. 11 delivers the final version of the stress equilibrium equation. The only external force applied on the cell is $\boldsymbol{F_{adh}}$ which represents the interaction between the channel walls and the cell periphery and is applied as a boundary condition (BC). Internally generated cell forces are implemented as active stress terms. A body force representing the force generated by actomyosin contraction ($\boldsymbol{\nabla} \cdot \boldsymbol{\sigma_c}$) is applied throughout the volume as a function of the myosin distribution.

$$-\boldsymbol{\nabla} \cdot \boldsymbol{\sigma_e} \;=\; -\nabla p\boldsymbol{I} + \boldsymbol{\nabla} \cdot \boldsymbol{\sigma_c} + \boldsymbol{F_{adh}} \tag{12}$$

Gravitational and inertial forces are assumed to be relatively small and accordingly ignored. Together equations 6 and 12 represent the governing pressure diffusion and stress equilibrium governing equations respectively.

3.2.2 Geometry:

Once the cells reach full confinement they roughly assume the shape of the channel. Since the microchannels have a rectangular cross section, the cells are modelled as elongated cuboid having the cross-sectional areas of 5 μm x 5 μm. The cells were split down an axial plane along the midline. Only half of the channel was modeled using symmetry to reduce computational load. Cells were not split axially in the vertical direction to allow possible simulation of wall pairs exhibiting compliance mismatch. The length of GBM cells in the microchannels is highly variable ranging from tens of microns to hundreds. The initial cell length was taken from the average of 3 manageable cell length measurements and given a value of 48 μm. The final dimensions of the brick shaped computational domain were 5 μm x 2.5 μm x 48 μm.

3.2.3 Boundary conditions

All of the boundaries were assumed to restrict fluid movement normal to the surface. This is consistent with the cell membrane retaining fluid. Similarly no normal gradient was permitted across the symmetry plane.

$$\widetilde{\boldsymbol{n}}\boldsymbol{\nabla}p = 0 \tag{16}$$

Both the rear and leading edges of the cell domain were left unconstrained initially allowing free movement depending on the deformation dictated by the model. However, later it became apparent that a global pre-stress was necessary to maintain pressure in the cell. This pre-stress was envisioned as a contractile link connecting the two distal cross sectional surfaces of the cell through the nuclear region probably through intermediate actin-myosin filaments. This conformation would allow the cell to remain under tension, retain a positive pressure, and provide an active link between the edges of the cell and the nucleus that would provide an avenue for mechanosensing. This stress boundary condition (eq. 17) was modeled as a normal inward stress on each axial extreme directed back toward the nuclear region and the opposite extremity with a magnitude equal to the initial pressure.

$$\boldsymbol{\sigma_{rear\ edge}} = \boldsymbol{\sigma_{leading\ edge}} = -\widetilde{\boldsymbol{n}}P_0 \tag{17}$$

The cell walls were modeled as compliant using a spring foundation boundary allowing a nominal degree of normal penetration. Wall surfaces permitted only small penetration into the surrounding channel walls by employing a restoring penetration force ($\boldsymbol{F_{pen}}$) directed normal to the cell-wall contact region back toward the original position.

$$\boldsymbol{F_{pen}} = -K_{pdms}(y - y_{wall})\big|_{y=0,2.5} \tag{18}$$

$$\boldsymbol{F_{pen}} = -K_{pdms}(z - z_{wall})\big|_{z=5} \tag{19}$$

$$\boldsymbol{F_{pen}} = -K_{glass}(z - z_{wall})\big|_{z=0} \tag{20}$$

Pressure dependent adhesion boundaries: A key objective of the modeling was to examine how cells might generate propulsion in the absence of specific cell-wall binding. Typically, models involving lamellipodia driven propulsion utilize a viscous adhesion-like drag force that is proportional to the local density of integrins involved in specific cell-substrate binding (37, 38). Although this strategy has been utilized to account for integrin based binding previously, with some minor adjustments a similar approach can be utilized to model nonspecific, pressure dependent cell-wall interactions.

$$\boldsymbol{F_{adh}} = -\beta(p)\frac{\partial \boldsymbol{u}}{\partial t}\,|_{wall} \tag{21}$$

$$\beta = \beta_0(p + p_n) \tag{22}$$

The adhesion force is proportional to the csk velocity through a pressure dependent constant (β) but directed in the opposite direction. Equation 21 indicates that as internal pressure rises there is an increase in the frictional drag force at the wall. β_0 is a proportionality constant that controls the strength of the adhesion. Values ranging from 2 to 200 $\frac{s}{\mu m}$ were employed in literature simulate integrin based adhesion (37, 38). As there are no available direct measurements of confined cell-wall friction, b ranges were adopted from the lower end ranging from 2 to 20 $\frac{s}{\mu m}$ thereby assuming less adherent conditions**.** An additional adhesion force was applied between the nuclear and channel walls by including an artificial nuclear pressure. We assume that as the cell is squeezed into small confined regions, the csk within the cytosol will rearrange relieving some of the elastic recoil. The compressed nucleus, on the other hand, will retain more elastic energy continuing to push back against the confining walls providing additional resistance to movement. This resistance would be partially alleviated during contraction of the global link connecting the cell's extremities and passing around the nucleus. As tension were to build in the filaments the cell edges would be pulled inward and the nucleus would be flattened as the filaments were pulled toward the midline. This was simulated by ramping pn down as the actomyosin contractions ramped up. We have adjusted the normal force in this region to compensate for this effect.

3.2.4 Material properties and physical parameters:

The actin and myosin densities in the model are key factors driving the material properties and the applied driving body forces respectively. The data for the actin and myosin densities was extracted from experimental data in taken from GBM cells migrating in confinement. The experimental data was normalized in terms of magnitude and in terms of the axial spatial dimension (X*) and then added into applied within the simulation. Since it was not possible to take the actin and myosin data from a single cell, the dynamic myosin data from a QSL migrator was collected from one cell and combined with a static actin density taken from a second cell. The experimental myosin and actin profiles that were loaded into COMSOL are illustrated in fig. 3-1.

The density of the cytosol was chosen to match water or ρ = 1000 kg/m^3 (37, 38, 47). The solid volume fraction in the model is a product of the dimensionless actin density and the maximum actin concentration which was taken to be 0.5. Both the hydraulic permeability and Young's modulus were varied with the solid volume fraction. The hydraulic conductivity can vary over several orders within different cells and probably varies significantly internally. For our purposes, a base value (K_0) of 4E-15 [m^4/Ns] was employed similar to Taber et al (47). The conductivity was allowed to vary as a function of the porosity. Regions with more solid fraction exerted more resistance to fluid flow trapping fluid for longer periods and allowing regional pressure buildup. In addition, conductivity was dropped by two orders of magnitude through the nuclear region assuming that the nuclear membrane and contents would provide a large resistance to fluid movement through the center of the cell. The Kozeny-Carmen equation predicts that for porous materials made up non-cylindrical pores, the hydraulic conductivity will vary as a function of the porosity as indicated in Eq.23 (50). The poisson ratio was chosen as 0.3

$$K = K_0 \left(\frac{\varphi^{f^3}}{\varphi^{s^2}} \right) \tag{23}$$

The cell stiffness was also controlled by the solid volume fraction and was modeled as a product of an initial stiffness coefficient E_0 and the dimensionless actin concentration. The value for E_0 was taken to be 500 [Pa] in line with other values used (37, 38, 43, 47).

The actomyosin contractile engine drove the model. The contractile stress was modeled as a function of an actomyosin contraction parameter (Y_0) and the dimensionless myosin distribution similar to previous papers (37, 38, 51). The contraction was assumed to occur axially. Y_0 was varied over values from 50 to 200 [Pa].

$$\boldsymbol{\sigma_c}\, \boldsymbol{i} = Y_0 Mr(t) \boldsymbol{i} \tag{24}$$

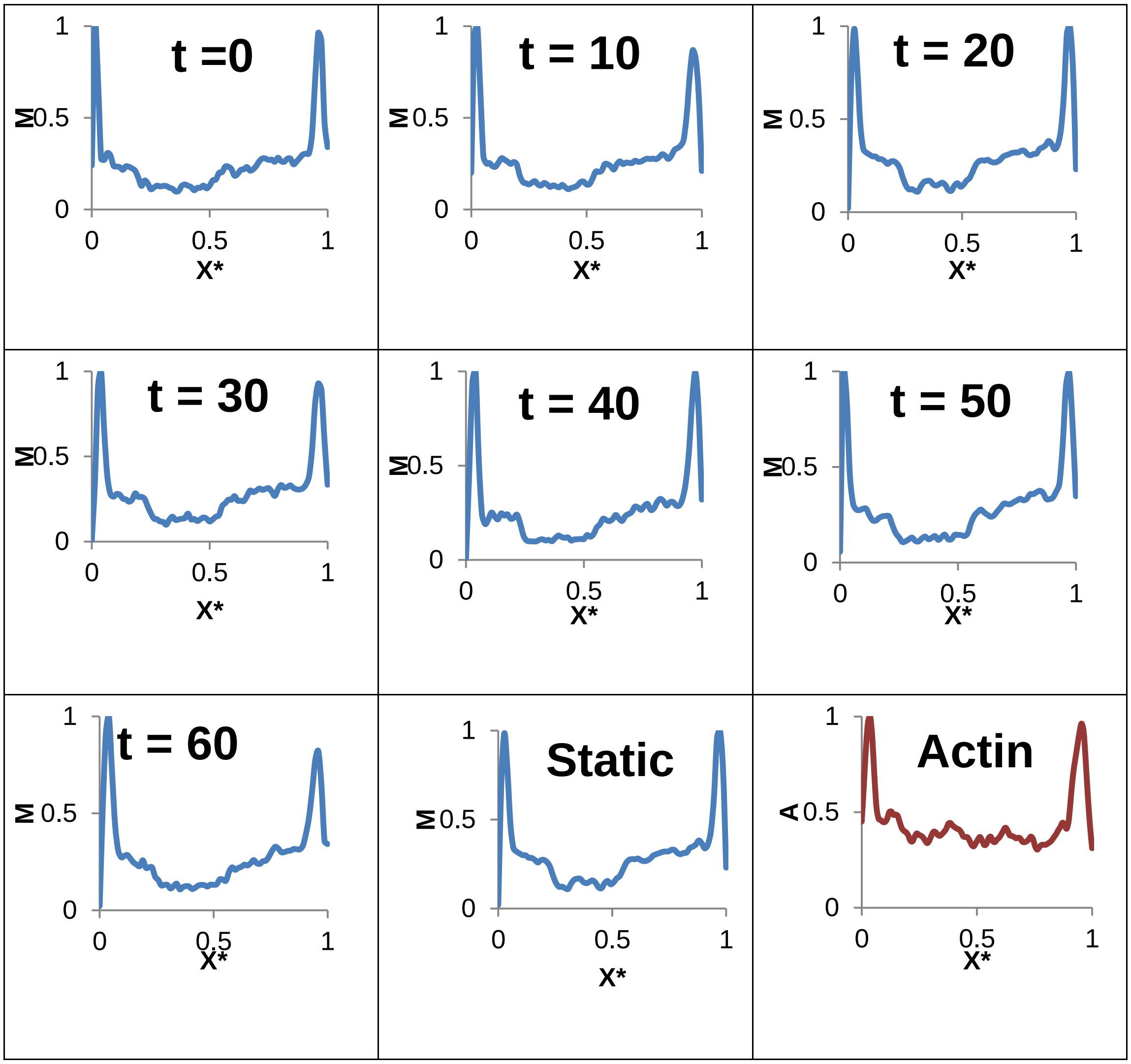

Figure 3-1. Actin and myosin distributions were integrated into the simulations. Dynamic myosin distributions taken from the QSL migrator in chapter 2 were integrated into the simulation to validate the model using comparisons of displacements predicted by simulation versus those observed experimentally. A static myosin distribution was employed in a separate simulation. Static actin profiles used to define the solid fractions in the model were derived from QSL migrators in chapter 2.

3.2.5 Initial Conditions:

Initial displacements and velocities of the csk were set to zero and a nominal initial internal pressure was established in the range of 50 – 100 [Pa] giving internal cell pressures at the low range of measurements taken in fibroblasts by previous research (24). The pressure in the cell was assumed to have reached a steady state equilibrium condition before the initiation of contraction or polymerization thereby neglecting any preexisting pressure variations.

We have assumed that the solid volume fraction in this case is dictated by actin cytoskeleton ignoring contributions from organelles etc. Previous researchers have modeled the intracellular actin distribution as a normalized distribution increasing from the rear edge toward the leading edge as suggested by data taken from within the lamellipodia (38, 49). Live GBM cell imaging in 5 μm x 5 μm confined channels has revealed axial actin profiles characterized by actin accumulation at the cell poles. We utilized an axial actin distribution that mimics the experimentally derived protein distributions as illustrated in fig 1. Fig 1A shows a GBM cell in a 5 x 5 um microchannel traveling in the direction indicated by the arrow. Analysis using imageJ software indicated preferential F actin aggregation near the poles of the cell. Fig 1C illustrates the pole-dominated actin distribution utilized during the COMSOL simulation. The actin profile has been normalized to give a maximum value of 0.5 near the poles of the cell. Live GBM imaging was also conducted using cells stained fluorescent green for myosin (pMLCII). Once again, cells within the microchannels exhibited myosin distributions characterized by heavier concentration at the poles. Although there were variations both temporally within single cells as well as between various cells, the general pole-heavy myosin distribution illustrated in fig. 1B and graphically in fig.1D is common to a large number of cells within the channels. Fig 1B clearly illustrates that myosin has been reoriented in full confinement to gather preferentially at either pole of the cell. Using freely available imageJ processing software an axial distribution profile was extracted by quantifying normalized intensity along the axial centerline of the cell (fig 1D). Fig. 1D illustrates the distribution taken from fig 1B.

Table 3-1 Outline of multiple simulations exploring confined cell migration.

	Simulation 1	Simulation 2	Simulation 3	Parametric
Actin	Static	Static	Static	static
Myosin	Dynamic	Static	Dynamic	Dynamic
Global Contraction	No	Yes	Yes	yes
Value	Proof of Global Contractile Engine	Closer exploration of physics	Validation	Explore effects of varying contractility parameter and nuclear drag

3.2.6 Discretization and solution

The swept mesh was composed of 5100 hexahedral elements. Width and height distributions were employed to control the number of horizontal and vertical elements in any cross section with the height being divided by 10 elements and the width by 3 elements. Axial distributions were separated into the rear, the nucleus, and front of the model. The rear and forward compartments were broken down into 70 axial divisions aligned in a symmetric geometric sequence allowing increased element density near both the cell edges where loads are applied and near the nucleus where there is a sharp change in material parameters. The nuclear compartment was subdivided into 30 axial divisions again utiling a symmetric geometric sequence allowing increased element density adjacent to nuclear-cell interfaces where material parameters change. Mesh refinement studies were performed until increasing axial mesh density produced no significant changes in the results.

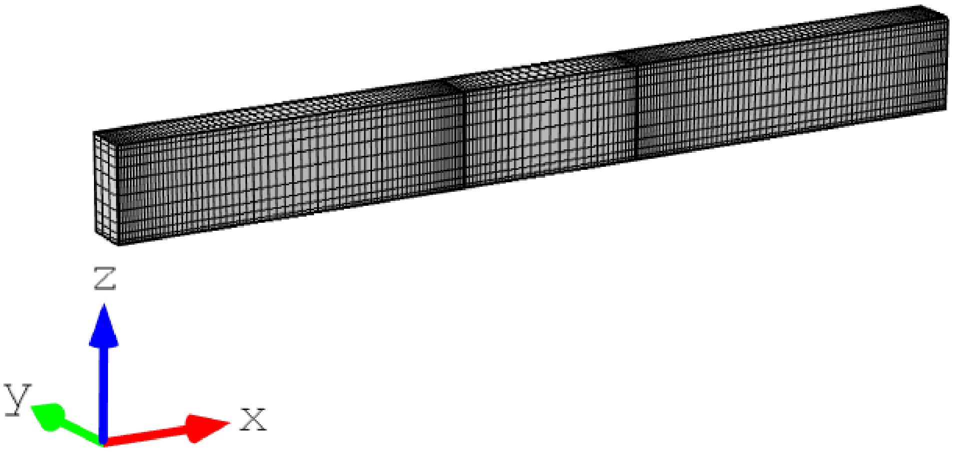

Fig 3-2. Discretization. Hexahedral elements were swept from rear to the front in the rear, nucleus, and front domains employing element inflation near the domain boundaries and interfaces.

Simulations were carried out for 10 minutes or 70 minutes simulation time respectively. An intermediate BDF time-stepping scheme was utilized with a maximum step of 10 s to prevent errors near time steps having abrupt changes. A multifrontal massively parallel sparse direct solver (MUMPS) was employed at each time step. All equations were fully coupled using an affine invariant form of the damped Newton method.

3.3 Results

3.3.1 Simulations without a global active link produced unrealistic pressures

Early simulations were attempted without any active global contractile linker (global engine) applied to the axial boundaries. These cells were unable to maintain positive internal pressures during lengthening even at the axial poles. The QSL migrators do undergo cycles of lengthening and shortening, but these cycles are much longer than lengthening and shortening cycles observed in AFE migrators. The GBM cell represented in fig. 2.4A was a QSL migrator that was undergoing a period of lengthening (relaxation) as the data collection began.

Figure 3.3 shows volumetric pressure contours at time points corresponding to 20 s, 40 s, 60 s, and 120 s. Note that the actomyosin generated contractile stress (internal engine) ramps up to full strength between 2 s and 12 s. The contractile strength is proportional to the myosin density (equation 2.?) which has highly localized peaks adjacent to the cell's edges (fig 3.1: t=0). Furthermore, the localized actin peaks adjacent to these edges result in regions of lower fluid permeability allowing for temporary pressure buildup. As the cell ramps up its actomyosin generated stresses, the local regions near the cell edges undergo the maximum levels of contraction while also maintaining the highest resistance to fluid flow. The pressure buildup near the edges is apparent at 20 s (fig. 3.3). As time progresses the localized buildup dissipates as fluid is redistributed.

The simulation predicts a lengthening period corroborated by the experimental observation. Strong contractions near the cell ends in conjunction with a slight axial lengthening results in negative pressures that begin to develop near the cell's center as can be seen in fig. 3.3 as early as t = 20 (s). By the time the simulation has progressed to 2 minutes, the intracellular pressure profile throughout the entire cell body has dropped below zero. Without any global axial load or constraint to offset the expansion in the cell interior, the cell cannot maintain positive pressure. In order to maintain the internal pressure in a vessel there needs to be some type of tension or load actin in the opposite direction like a surface tension directed inward or a stressed cytoskeleton. Experimentally, GBM cells traveling through fully confined channels displaying QSL migration characteristics do not stop blebbing as the cells go through elongation and shortening. This implies that a global force (cytoskeleton tension or membrane tension) linking the two poles must be present to maintain the positive intracellular edge pressures needed for blebbing as the cell undergoes slow elongation.

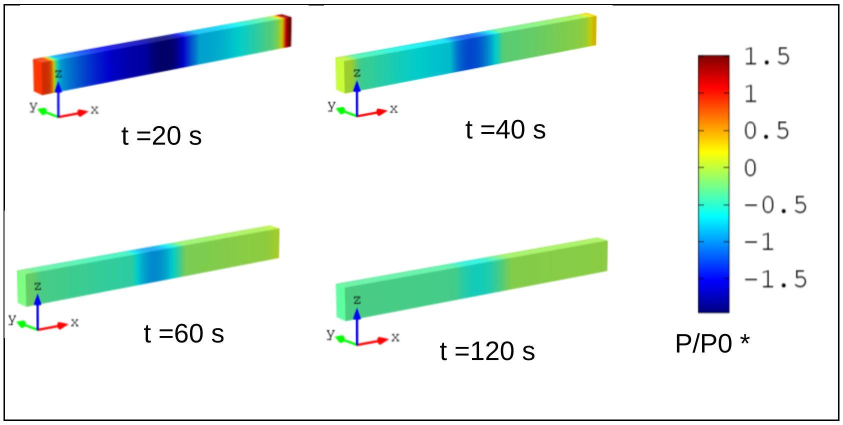

Figure 3-3. Pressure distributions in a simulated GBM cell undergoing localized actomyosin contraction in the absence of an active global link. As the actomyosin contraction ramps up from 2 s to 12 s localized pressure buildup is seen at the edges. By 20 s negative pressure begins to overtake the cell interior. By the time 1 minute is reached all pressures have been driven to negative values.

When the time has reached 1 minute expansive strains are notable in central portions of the cell adjacent to the nucleus (fig. 3.4). This region coincides with lower stiffness values due to lower actin concentrations near the cell center. Thus there is a central region of lower stiffness (fig. 3-4: between the lines) surrounded by regions of higher stiffness at the cell edge and at the nucleus. Strong contractions at the edges result in an outward pulling that leads to expansive strain within this weaker central cell region. This axial expansion drives negative pressure generation in the region that quickly spreads throughout the cell

When the simulation was repeated with the exception of adding a boundary stress directed along the inward normal at each axial boundary in order to mimic an active based stress connection pulling the edges toward the nucleus and one another, the pressure profiles returned to the positive regime (fig. 3-5). The extremities maintain positive pressures throughout the simulation even as the cell is in an elongation mode. This reinforces the necessity of the existence of a continuous force transmitting link between the leading edge, trailing edge, and probably the nucleus.

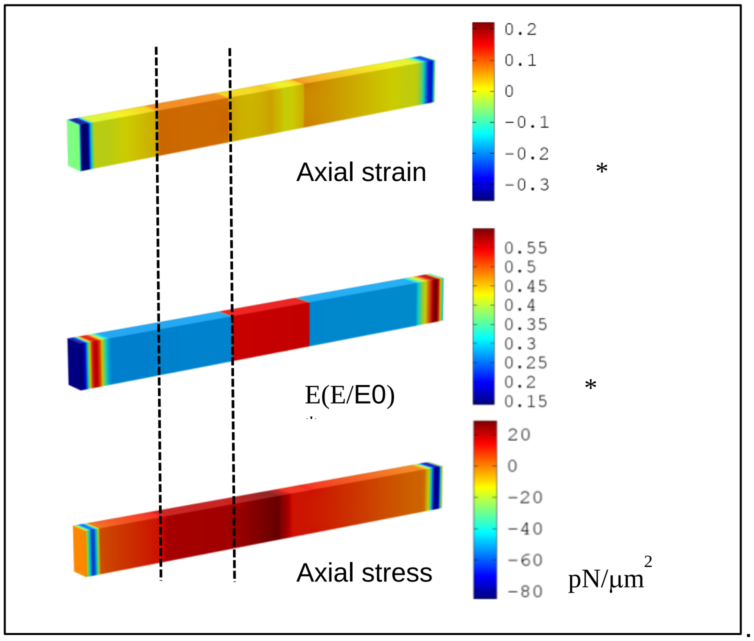

Figure 3-4. Strain, normalized modulus (E/E0), and stress at t = 1 min.

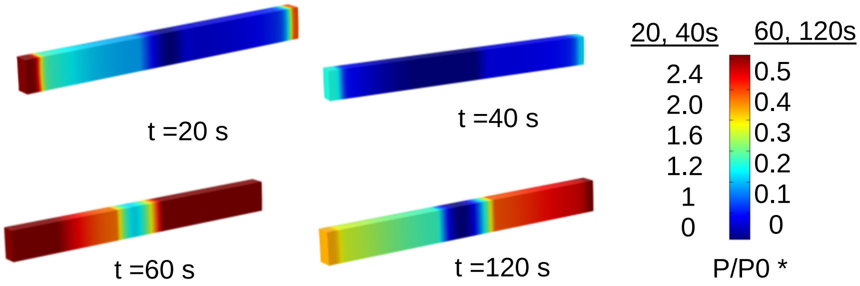

Figure 3-5. Pressure distributions obtained after addition of prestress to the edges. Pressure distributions were obtained at 20 s, 40 s, 60 s, and 120 s. Note that even at 120 s the pressure distribution is positive particularly in the extremities.

3.3.2 Static actin and myosin profile produced realistic movement

The remaining simulations all included an added force coupling between the leading and trailing edges. A load equal to the initial pressure (P0) was applied to the leading and trailing boundaries that pointed along the inward normal back toward the cell center or opposite boundary. This was intended to mimic an interior contractile structure fastened to both ends of the cell and pulling them toward one another with a relatively constant force.

Static experimental actin and myosin data (fig. 3.1) were fed into the simulation to examine the predicted cell dynamics more closely. The simulation was carried out for 10 minutes. Figure 3-5 outlines the dynamic displacement of the trailing and leading edges during the 10 minute simulation. Initially, as the myosin contractions ramp up (0 s to 1o s) in the cell extremities, there is a concomitant retreat of the leading edge and propulsion of the trailing edge. As strong contractions are generated in the extremities in the early seconds, there is a pull to the contractile centers just proximal to both edges causing both edges to be pulled toward the cell interior.

After an initial pull toward the cell interior, both edges begin to move forward with a very linear displacement over time indicating a constant velocity at both edges. Much like the observations with QSL migrators, the front and rear edges remain well coupled during migration as can be noted by the very steady gap between the displacements of the edges. The simulation predicts an average velocity at the rear of 7.6 μm/hr and at the front of 8.8 μm/hr. This is comparable to the QSL speeds noted in fig. 2.4 which are close to 9 μm/hr at the rear and range from about 4 to 8 μm/hr in the front. The speeds are slightly elevated at the rear due to the slight initial retraction of the leading edge. Consequently, the leading edge achieves slightly less displacement over the time period.

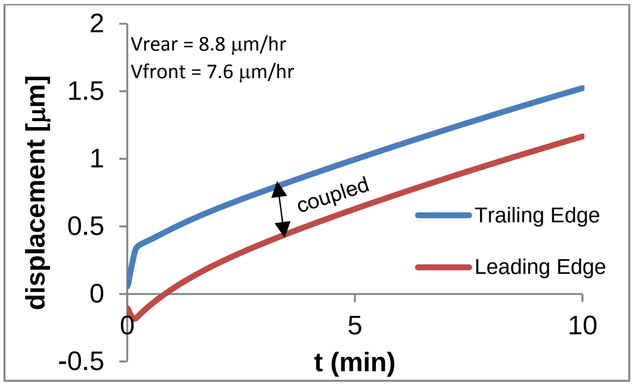

Figure 3-6. Displacement at the leading (red) and trailing (blue) edges during simulated cell migration with a static myosin loading. The edges are slightly displaced at t=0 s due to the inclusion of a global contracting force.

3.3.3 Local pressure and adhesion forces varied transiently.

In typical 2D migration, cells transmit forces within their cytoskeleton to the substrate via integrins or focal adhesions. In this simulation, the integrin based transmission has been replaced by a pressure based transmission. Figure 3.4 combines graphs of the axial profiles of dimensionless intracellular pressure coupled with the pressure based adhesion forces to explore the role of dynamic pressure in cell/substrate force transmission.

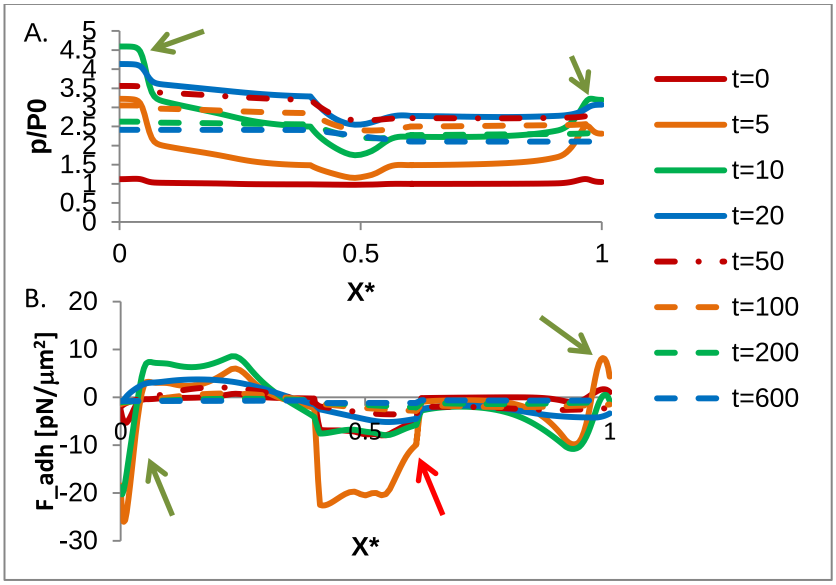

Figure 3-7. Dynamic axial pressure and adhesion profiles. A) Dynamic axial pressure profiles along with B) dynamic pressure induced adhesion force profiles

Early in the simulation (up to 20 s), as contractile stresses build especially near the axial edges, there are resulting spikes in localized pressure (fig 3-7.A green arrows) adjacent to the edges. These regional spikes in pressure result in simultaneous adhesion spikes in the same areas (fig. 3-7.B green arrows). Recall that the adhesion force is proportional to the velocity and directed in the opposite direction. At the trailing edge, these adhesion forces are negative due to the forward pull on the trailing edge. At the leading edge these adhesion forces are positive, directed against an initial backward movement of the leading edge as illustrated by the early negative displacement of the leading edge in fig. 3-6. These pressure spikes slowly disappear as the fluid begins to redistribute through the cell interior leaving a cell with elevated interior pressure. Meanwhile adhesion forces begin to stabilize with the dwindling of peripheral adhesion spikes. The adhesion forces across the entire surface reduce and become negative as more of the cell begins to slide forward. Soon the adhesion forces are all directed backward as the entire cell begins to migrate.

In the beginning there is strong adhesion in the nuclear region (red arrow). This strong adhesion disappears quickly as the cell is able to gain traction and utilize the axial pull to laterally flatten the nucleus enough to migrate.

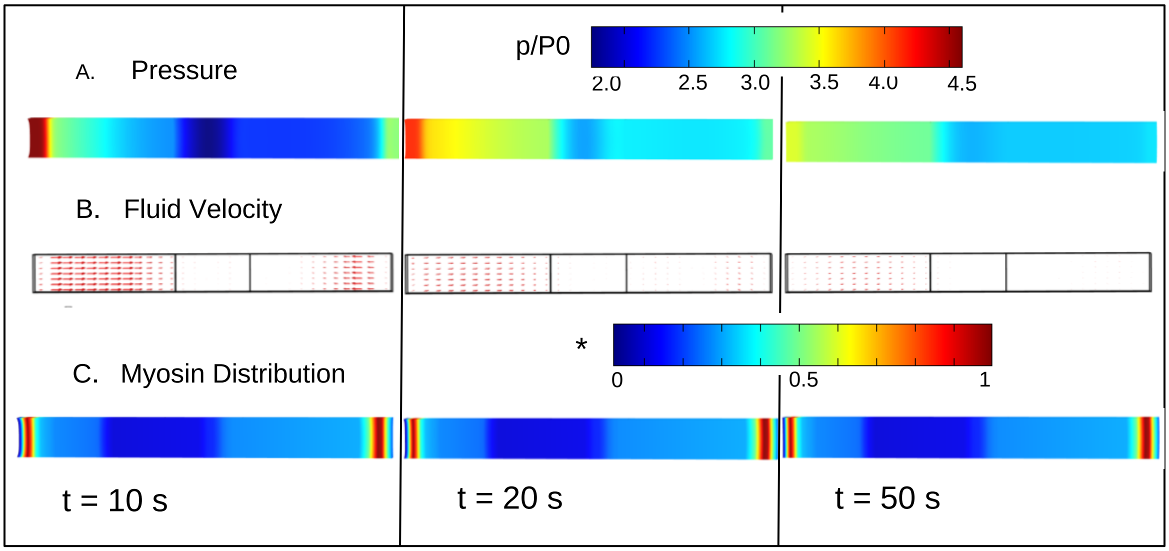

Fig. 3-8. Dynamic pressure and myosin contours along with fluid velocity vectors. A) Axial pressure contours illustrate early pressure buildups (t = 10 s) in localized hubs near the cell extremities and eventual dissipation (t= 50 s). B) Fluid vector plots indicate the redistribution of fluid away from the early axial pressure hubs. C) Myosin distributions are shown for reference to the location of strongest contractions.

Fluid redistribution after early pressure buildup near the edges is illustrated in fig.3-8. As contractions ramp up (t = 10 s), localized pressures begin to escalate (fig 3-8 A) in local contractile zones which correspond to local myosin and actin maxima (fig 3-8 C). As pressures build, elevated pressure gradients begin forcing fluids away from these pressure hubs (fig. 3-8 B). Eventually this redistribution of fluid permits pressure stabilization (fig 3-8 A). As local pressures stabilize, fluid movement slows.

3.3.4 Dynamic myosin profile integration reproduced complex migration

Experimental dynamic myosin profiles taken every 10 minutes (fig. 3.1) from a QSL migrator that was followed for over 70 minutes were incorporated into the simulation. The model was able to predict the displacement of the cell over that time period along with the initiation of lengthening / shortening. Figure 3.8 shows the track of simulated rear (blue solid) and front (red solid) of the cell alongside the experimentally observed track the rear (blue dashed) and front (red dashed) of the cell actually followed. The temporal pattern of displacement is reproduced by the simulation over the experimental time frame.

Period A: Over the first 10 mins of the simulation the cell moves forward with a linear displacement over time. The simulation slope (velocity) is a very good match for the experimental velocity at the front of the cell over the first two thirds of the period and is slightly faster than the rear. Near the end of period A, the cell begins to slow. The simulation continues with the linear behavior indicating that a shorter sampling period would be more accurate. This under-sampling of the experimental data leads to a slight over-prediction of displacement in the first period. Over this period, the leading edge in the simulation is slightly ahead of the trailing edge but there is very little separation. The cell achieves a much larger gap between leading and trailing edges experimentally. This is probably either due to a lack of the modulation of the active global constraint binding the rear and front of the cell or, more likely, due to the model's application of impermeable boundaries combined with incompressible conditions. While the model doesn't allow any fluid transfer between the cell and environment, this condition is probably too severe. In fact, there is certainly, fluid exchange between the cell and channel for the cell to achieve the observed states of lengthening and contracting witnessed.

Period B: As period B begins there are two notable changes in the cell. First, the cell begins to slow down. As B begins, the trailing edge velocity slowly diminishes until the cell displacement flatlines for nearly the entire period. Meanwhile the cell undergoes another notable change in that it begins to shorten. The leading edge begins too slow just prior to the onset of period B, but continues its negative trajectory over the entire period leading to a shortening. The simulation predicts the velocity change as the simulated rear displacement also flatlines over this same period. The change is more abrupt in the simulation, again probably indicating that an increased sampling frequency in this time period might lead to a more gradual change. Once more, the simulation also indicates a slowing of the leading edge at the onset of period B. The simulated cell also begins moving in a shortened configuration and continues over the remainder of period B. The contraction occurs rapidly at the onset of the period and the shortened state is not nearly as impressive as that witnessed in the cell, but again this probably indicates that impermeable boundaries are too severe.

Periods C-G: After period C the cell continues to move in a contracted state for the entire duration of migration. The velocity remains pretty linear with the exception of a single rise and fall surrounding period F. Over the same period, the simulation predicts a very similar trajectory. Once again, the velocity is slightly slower than the trailing edge of the cell. Figure 3-10 shows displacements over the last 50 minutes fitted to linear trendlines to ascertain the relative velocities. The simulation predicts a linear velocity of 0.150 μm/min over the time frame. This falls right in between the observed velocities of 0.142 um/min at the leading edge and 0.156 μm/min at the trailing edge.

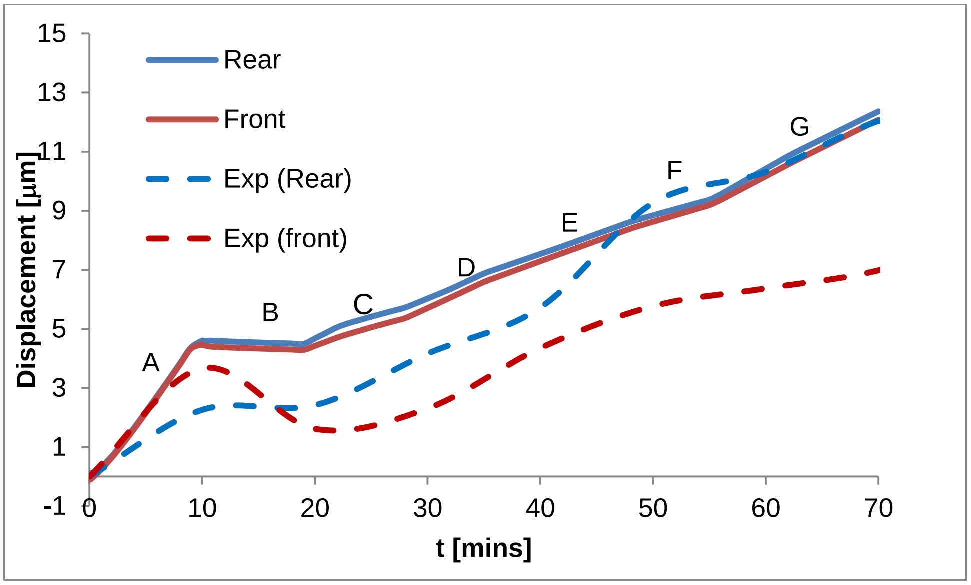

Figure 3-9. Comparison of simulation predicted and experimentally observed displacements. The displacements are plotted over time (70 minutes) for the leading (red dashed) and trailing edge (blue dashed) of a QSL migrator and compared to the simulation predicted results at the leading (red solid) and trailing edges (blue solid).

All periods: To summarize, the simulation was able to predict the migration behavior of a QSL migrator when supplied with dynamic myosin data to drive migration. Displacements and velocities predicted by the simulation were close matches to the observed migration. The simulation was able to accurately predict the pattern of lengthening/shortening observed experimentally but was unable to achieve the same level of separation between the front and rear displacements witnessed experimentally probably owing to the application of overly severe impermeable boundary conditions between the cell and the channel.

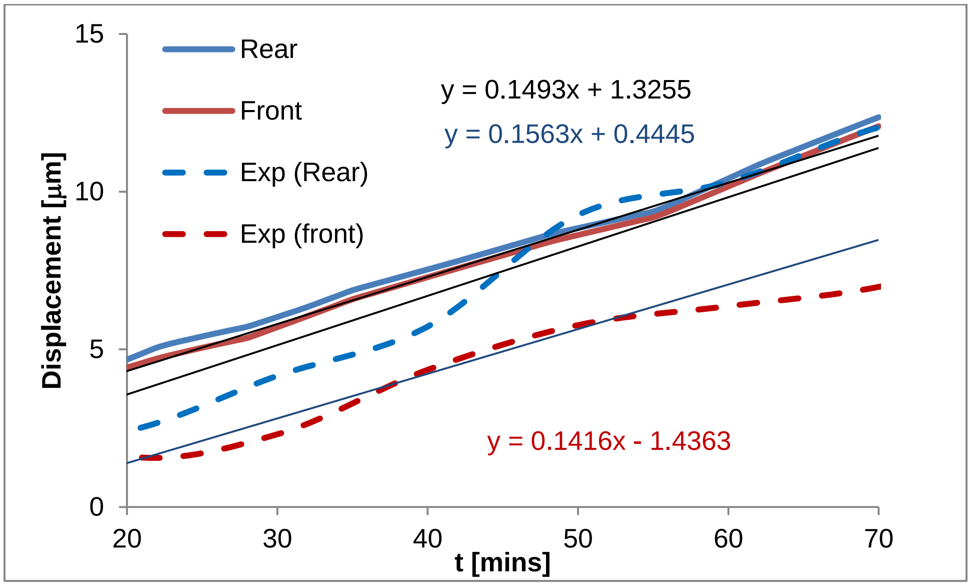

Figure 3-10. Cell and simulation predicted velocities over the final 50 minutes. The simulation and experimentally predicted displacements were plotted again, this time with trend lines to compare velocities over the last 50 minutes. The simulation predicts a velocity of 0.15 μm/min over the final 50 minutes whereas the front and rear move with velocities of 0.14 μm/min and 0.16 μm/min. respectively.

3.35 Parametric analysis varying the contractile stress parameter and the nuclear swell parameter.

In theory, varying the strength of actomyosin contractility or the nuclear resistance (deformability) should affect the cells ability to migrate effectively. Clearly, blebbistatin exposure inhibits or slows migration in cells dependent on actomyosin contraction. Previous research also indicates that nuclear deformability constitutes a rate-limiting step during cell migration in 3-D environments and that cells reduce levels of lamin A/C in the nuclear envelope which are critical determinants of nuclear stiffness(52).

The model successfully reproduced complex migration strategies over a long time period with multiple contractile inputs. Parametric simulations were next undertaken for 50 minutes varying the contractile stress parameter and the nuclear pressure coefficient respectively to garner model insight into confined migration during inhibited contraction or changing cell deformability.

The first parametric study was conducted varying the contractile stress parameter (Y0), which controls the strength of the actomyosin contraction, utilizing values ranging from 50 [Pa] (solid lines) to 100 [Pa] (dashed lines) to 200 [Pa] (dotted lines). Fig 3-11 indicates that as Y0 dropped from 200 [Pa] (dotted lines) to 100 [Pa] (dashed lines) to 50 [Pa] (solid lines) there was a concomitant decrease in cell velocity and distance travelled. The model predicts that if cell contractility is interfered with possibly using blebbistatin or some other drug cell velocities will slow.

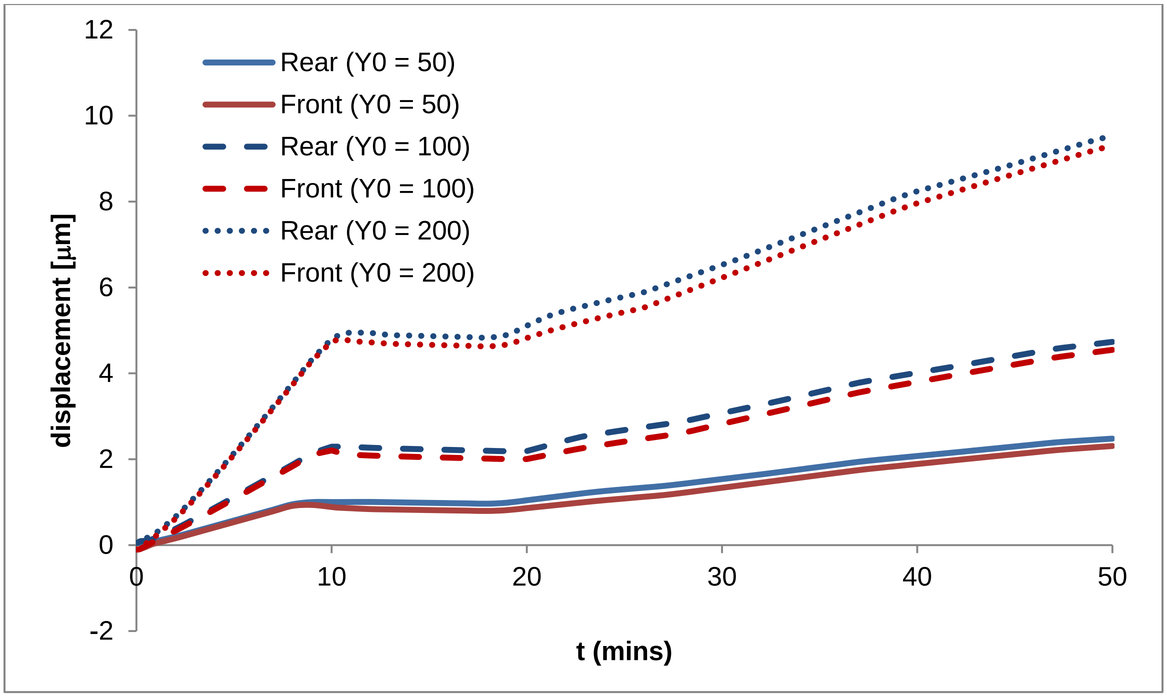

Figure 3-11. Cell migration changing as a function of a varying contractile stress parameter. As the contractile stress parameter (Y_0) was decreased from 200 [Pa] (dotted) to 100 [Pa] (dashed) to 50 [Pa] (solid) the cell slowed down.

The second parametric study explored the consequences of varying the nuclear recoil pressure coefficient which controls the amount of additional friction-inducing pressure exerted by the nucleus onto the walls due to nuclear recoil as a result of the nuclear elasticity after squeezing into confinement. The nuclear elasticity pressure coefficient was included to simulate an additional force directed against the walls by the nucleus in response driven by nuclear elasticity recoiling against confined compression. Figure 3-12 shows that as the nuclear recoil pressure coefficient was increased form 5 [Pa] (solid lines) to 50 [Pa] (dashed lines) to 500 [Pa] (dotted lines), the cell speed and displacement reduced. Thereby, the simulation predicts that cell migration in confined channels is hindered by nuclear envelope stiffness and any reduction in this stiffness should increase migration potential.

To summarize the parametric studies were conducted to examine model predicted cell responses to changes in cell contractility or changes in nuclear drag induced by nuclear recoil against the walls in response to confinement. The simulation predicted that increases in the contractility parameter led to a parallel increase in migration potential in the traveling cells. Decreasing the contractility parameter as would be the case during exposure to drugs such as blebbistatin led to decreases in the cell’s migration potential. Reduction in nuclear drag possibly as a result of lamin A/C downregulation in the nuclear envelope again led to increased migration potential. Cells with stiffer nuclei would experience greater difficulty migrating through confinement suggesting that indeed drag induced by nuclear elastic recoil in confinement may play a major role in determining cell migration potential.

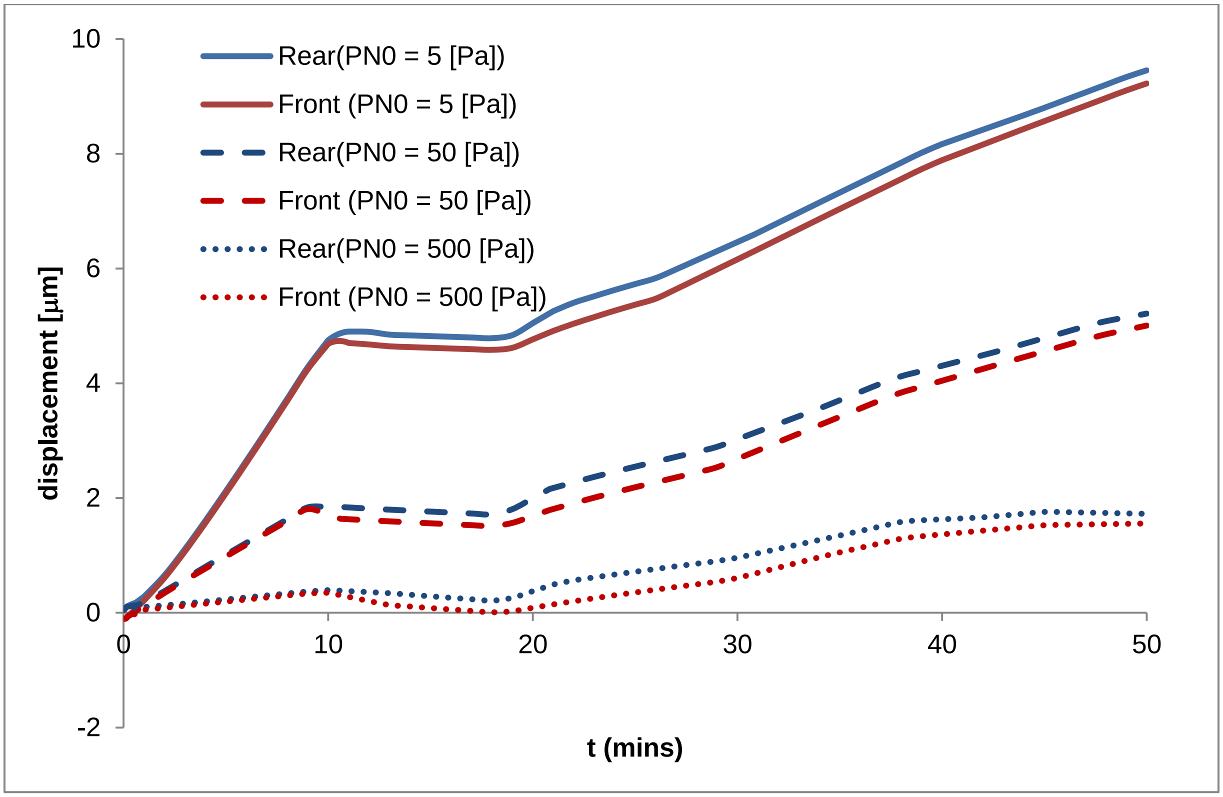

. Figure 3-12. Cell migration reduced as a function of increasing nuclear pressure coefficient. As the nuclear recoil pressure parameter (RN_0) was increased from 5 [Pa] (dotted) to 50 [Pa] (dashed) to 500 [Pa] (solid) the cell slowed down significantly indicating that nuclear drag is a key factor affecdting migration.

Chapter 4

Discussion

4.1 Migrating cells with compressed nuclei show at least two distinct migration strategies

As GBM cells enter channels with dimensions less than their nuclear cross sectional areas there are changes in the cytoskeleton distribution. Actin and myosin both are redeployed away from the interior of the cell out toward localized regions near the cell edges. Integrin dependent migration becomes dispensable (19, 53).

Two characteristic migration subtypes were identified after observing GBM cells migrating through channels undergoing nuclear squeeze. One subtype, termed an active front edge (AFE) migrator was more consistent with 2D planar mesenchymal cells due to frequent protrusion and retraction of various protrusive structures (pseudopodia, lamellipodia, invadopodia, filopodia) at the leading edge. The second subtype termed a quasi-steady length (QSL) migrator propelled itself forward maintaining a nearly steady length while traveling in a committed compressed state. This second subtype was characterized by vigorous blebbing at each axial free boundary.

The QSL and AFE migration subtypes were readily identified and characterized based on both the speed of their migration as well as the degree of coupling between front and rear displacements. AFE migrators routinely moved attaining higher speeds than their QSL counterparts. AFE velocities easily doubled the cell velocities seen in QSL migrators. Kinematic analysis revealed that AFE migrators did in fact experience more frequent activity at the leading edge usually in the form of protrusions followed by retractions. AFE migrators were characterized by a high degree of decoupling between movement of the trailing edge and movement of the leading edge usually with the trailing edge moving steadily forward with nearly constant velocity while the leading edge cycled forward and back. QSL migrators on the other hand maintained stable lengths while migrating, experiencing much less decoupling between the movement of leading and trailing edges. They travelled with reduced speeds comparatively and blebbed vigorously. While these migration strategies were readily identifiable and distinguishable, at least a portion of cells were not necessarily married to any particular strategy, instead maintaining the ability to switch strategies if needed.

The QSL migration strategy was explored more closely utilizing a quantitative framework to explore whether localized actomyosin contraction could be utilized to generate localized dynamic pressure driven distal adhesion to drive steady propulsion.

4.2 An argument for actomyosin driven confined migration

With integrins becoming dispensable to migration in small microchannels, and the AFE migration strategy appearing to more closely mimic mesenchymal-like, integrin-based gripping and pulling strategies, the QSL migrators became prime candidates to identify alternate transmission mechanisms. Although much of the research in channels appears to favor polymerization-based propulsion (actin or microtubule) in confinement, there is enough ambiguity in the results to suggest that actomyosin based propulsion may not be at odds with previous findings.

Previous research employing chemoattractants may artificially tip interchangeable migratory subtypes toward more of an AFE or polymerization driven subtype. Some of the studies supporting polymerization dominant mechanisms in confinement employed chemoattractants within the microfluidic setup to encourage migration (18, 19, 25). The purpose of many of these studies is to explore how mechanical confinement affects velocity, but the inclusion of an additional chemical stimulus complicates the picture. It is possible that chemical stimuli may override or tip cells to employ a particular migration strategy when combined with mechanical cues. The simulations and experiments outlined in chapter 2 were performed without the addition of any chemoattractant in order to isolate the effects of the mechanical from chemical stimuli as much as possible. Wilson et al fingered actin polymerization as the impetus for chemotactic migration in confined HL60 cells. Interestingly, they noted that if the cells were treated with an arp2/3 inhibitor (which prohibits the nucleation of new actin branching) cells did not cease movement altogether(18). Instead a population of cells adopted an alternate migration strategy characterized by vigorous blebbing. This seems to affirm that there is a second migratory phenotype and even implies that this phenotype may be suppressed by the addition of chemoattractant but is recoverable in the presence of a second chemical stimulus (arp2/3 inhibitor). Irimia et al observed breast cancer cell migration in confinement without chemoattractant and observed that these cells responded more to microtubule inhibition than actomyosin inhibition concluding that microtubule polymerization was the key driving force in breast cancer cell migration(27). Curiously, however, they found a small population of cells that continued to migrate even after microtubule inhibition which would support the possibility of two migratory subtypes and suggest that one of these phenotypes is driven by a mechanism other than microtubule polymerization. Again this points to the reality of multiple migration subtypes. Ultimately the lack of response to particular inhibitors should be interpreted with caution. It may well be less of an indicator of the absence of a particular mechanism and more of an indication of the cell's enormous potential for adaptability.

Other researchers have proposed alternative mechanisms to the actin/microtubule polymerization mechanisms above. Stroka et al (2014) noted that cell migration persisted even after the inhibition of actin polymerization and myosin II-mediated contractility (25). They proposed a mathematical model along with experiments suggesting that an osmotic engine could drive a “cell volume regulating” migration mechanism in confinement. However, they also found that their experimental results were most applicable to S180 cells which migrate independently of actin polymerization. Their findings were less relevant to MDA-MB-231 cancer cells which employed an active polymerization component. Once again chemoattractants were employed which have the potential to tip a cell away from a contractile mechanism toward a polymerization based mechanism which seems to be lacking in S180 cells. Petrie et al (2014) proposed that actomyosin contraction was critical for movement of human fibroblasts in 3D extracellular matrices and affected the type of protrusions the cell used to migrate (24). They suggested that intermediate filaments made up of actin and myosin IIA surrounded the nucleus and were linked to the nucleus through nesprin-3. Actomyosin contraction was employed by the cell to pull the nucleus forward, like a piston, pressurizing the forward compartment and inducing lobopodia formation. This migration description is consistent with the AFE migration mechanism which is characterized by a number of leading edge protrusions including lobopodia-like protrusions. Interestingly, their proposed model provides the first hint toward an active global contractile link within cells in confinement that couples both ends of the cell directly to one another as well as the nucleus (see fig. 4.1). Their model only lacks a rear attachment for the actin/myosin filaments whereby the cell could create global tension as well as lateral nuclear compressive forces.

QSL migrators move maintaining stable cell length ratios and are characterized by vigorous blebbing at both free axial boundaries. Polymerization based propulsion would seem to presuppose that cell length would change frequently with polymerization based protrusion at the leading edge followed by contractile or depolymerization driven retraction of the rear. The heavy blebbing suggests elevated pressures at the cell’s edges which could be driven by local internal contraction. An osmotic engine seems unlikely as the primary driving force generator in this experimental context as it would not explain the blebbing and there is a lack of steep osmotic gradients in the experimental setup. Actomyosin contraction on the other hand would explain the high intracellular pressures necessary for blebbing along with a possible explanation for alternative, pressure-derived force transmission to the substrate.

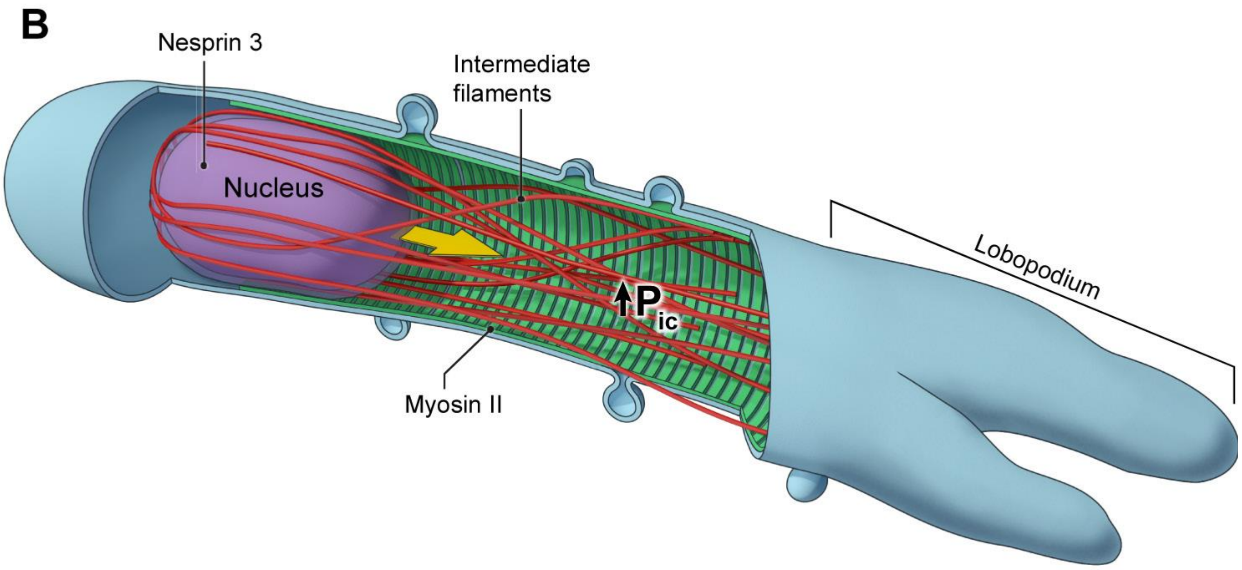

Figure 4-1. Nuclear piston model proposed by Petrie et al (2014). The nucleus is linked to adhesions at the front end through intermediate actin and myosin filaments that also bind the nucleus through Nesprin-3. Actomyosin contraction pulls the nucleus forward creating a nuclear piston that pressurizes the forward compartment driving lobopodia formation. Adapted from Petrie et al, 2014 (24)

4.3 GBM simulation suggests an active global link between axial edges with nucleus.

Simulations carried out without inward directed normal boundary stresses at each edge to mimic the effects of a continuous, actively contracting mechanical link between the two cell edges and the nucleus revealed that the cells had difficulty maintaining positive intracellular pressures when under internal expansive strain (fig 3-3). When this active mechanical link was added to the simulation positive internal pressures were maintained throughout the course of simulation. This suggests an actively contracting connection between the leading and trailing edges probably attached to the nucleus as well. There are a couple of possibilities to achieve this end-end linkage. The first possible mechanical link is the cell plasma membrane (PM). If the plasma membrane remained continuous and was associated with an actively contracting cortex the cell could encompass an end to end mechanical link while maintain intracellular pressures through surface tension. QSL migrators undergo periods of shortening and elongation. Any PM tension would be continuously disrupted by the active blebbing at the cell extremities. Once more, this may not provide the best setup for linking the cell surface to the nucleus to provide a means of mechanosensing especially in light of changes to the nuclear membrane (lamin A downregulation, possible loss of LINC complexes) that may accompany confinement. Another possible mechanism of achieving this linkage would be through contractile actin-myosin stress fibers or intermediate filaments that span the cell attaching from one end to another while skirting the nuclear boundary much like proposed by Petrie in fig. 4.3 above. Direct linking between the surface and nucleus would ultimately depend upon the presence and availability of LINC proteins like Nespin1, 2, 3 and SUN protein complexes.

4.4 Maintaining a pre-stressed configuration is critical for cell mechanosensing.

Research shows that when cells that are attached to flexible substrates are deformed they undergo immediate changes to their internal structures and stress fiber alignment (54). Forces that are applied to integrins can induce distant realignment of stress fibers and nucleoli, and mechanical coupling between integrins and nuclei is lost when intermediate filaments are disrupted (55). Despite unremittent remodeling of the cytoskeletal network, cells contain a “hard wired” interconnectivity that serves as a mechanical coupling between the environment and deep cellular structures like the nucleus. This interconnectivity provides a mechanical link by which the cell can quickly sense changes in its surroundings. Furthermore, because physiological loads decay to very tiny magnitudes within about 10 μm of the plasma membrane when cells are not stressed and homogeneous, this long distance force propagation is only possible if elements of the cell are in tension whereby stresses can be preferentially conducted through cellular components stiffened by tensile loading (54).

The mechanical interconnectivity for mechanosensing is provided via intermediate filaments composed of actin and myosin along with plasma and nuclear membrane bound complexes. Figure 4-2 illustrates this network beginning with transmembrane integrins which attach through anchoring complexes with proteins like talin, vinculin, zyxin, and paxillin to crosslinked actomyosin filaments all the way through the cytoplasm to LINC complex proteins including nesprins and SUN proteins that provide attachment to the nuclear surface. This continuous active contractile linkbetween the cell exterior and the nucleus provides a mechanical path for signaling the cell nucleus directly as well as providing the cells with a mechanism to maintain shape and control stiffness. When cells contain this active contractile link from surface to nucleus, mechanical forces can be channeled to the nucleus in much shorter time durations (1 ms) than can be achieved if the cell were utilizing diffusion (54).

Cells need to alter mechanosensing strategies when moving from a planar 2D environment to a confined environment particularly if integrin dependent cell/substrate binding is lost. Mechanosensing in 2D is heavily dependent on integrin based adhesion. When AFE migrators employ integrin based adhesion strategies similar to 2D it stands to reason that these cells probably utilize a similar mechanotransduction scheme. However, AFE migrators that lack integrins and QSL migrators lose an integral part of this mechanical link in the integrin based transmission component.

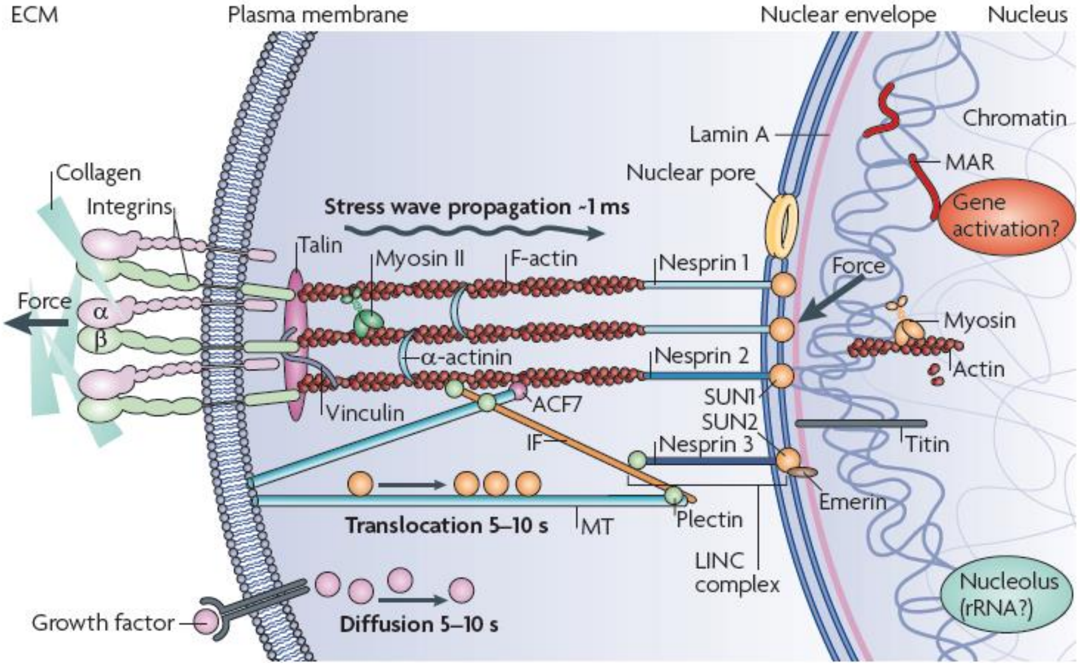

Figure 4-2. Pretension is critical for mechanotransduction. Stress waves propagate from the cell surface through pre-stressed actin and myosin filaments to the Nesprin complexes on the nuclear envelope in around 1 ms. Adapted from Wang et al 2009 (56).

4.5 Theoretical transition of stress fiber alignment form 2D to confinement

Stress fibers are critical for allowing the cell to control its shape, maintain stiffness, and preserve mechano-transductive connections used by the cell to interpret external mechanical cues. Stress fiber connectivity and force transmission on 2D planar substrates has been well outlined in the literature (51, 57-59). Stress fibers are bundles of about 10 to 30 filaments composed of F-actin crosslinked by actin-binding proteins (α-actinin, fascin, filamin) that are sometimes associated with nonmuscle myosin II (NMII) motors that generate contractile forces. Stress fibers are either coupled directly to the substrate through focal adhesions or indirectly through attachment to other stress fiber. There are three subcategories of stress fibers: dorsal stress fibers, ventral stress fibers, and transverse arcs that are characterized based on their connectivity to focal adhesions, associations with NMMII, assembly mechanisms, and function. The typical orientation and alignment of stress fibers is illustrated in fig. 4-3A.

Dorsal stress fibers (DSF) assemble without myosin. These fibers attach at one end to focal adhesions and that the other end to other stress fibers (transverse arcs). Research by Burnett et al, 2014 showed that these fibers attach to focal adhesions at the bottom of cells and rise up to attach to transverse arcs before extending radially inward toward the nucleus. The red fibers attached to focal adhesions (yellow) and extending back toward the nucleus in fig. 4-3A represent the dorsal stress fibers. These provide a lever by which transverse arc contractions can be transferred to the substrate allowing the cell to ratchet the lamellum downward controlling cell shape.

Transverse arcs contain myosin but no direct attachments to FA's on either side. Instead these cells attach through DSF to FA's and one another. These stress fibers run parallel to the cell edge creating radial arcs that move in a retrograde manner over time back toward the cell nucleus. Contraction of transverse arcs along with their attachment to DSF's allows the cell to regulate its shape.

Ventral stress fibers are rich in myosin II and associate with FA's on both sides. These stress fibers appear on the ventral surface of the cell in the 2D planar configuration and their contractions generate strong traction forces that help pull the rear forward in the planar mesenchymal motion strategy. The presence of FA's on both sides strongly suggests that these fibers play a key role in generating tensional homeostasis.

When cells move from 2D planar substrates into confined environments there will be a natural reorientation of fibers as the cells transitions first to a multi-planar mesenchymal-like strategy, then to an AFE migration strategy, and eventually to a QSL migration strategy lacking any integrin specific binding to the channel walls. Figure 4-3B-D attempts to outline a possible intuitive based transition sequence by which 2D stress fiber arrangements are transformed to phenotype consistent with AFE migration and eventually to the a phenotype consistent with live imaging of QSL migration.

As cells first enter channels, typically the nuclear dimensions exceed channel dimension and cells pause extending long pseudopodia-like extensions deep into the channels. These protrusions eventually bind with the channels walls as the cell attempts to prepare the nucleus for entry. Next, as the lamellum enters the channel, DSF's are naturally reoriented so that the FA attachments are distributed over all of the contacting planes. The radial stress fibers are deformed as the cell enters the channel. In 2D the transverse arcs run parallel to the front surface and radially move back toward the nucleus. When the lamellum moves into the channel the leading edge must fold at a right angle backward so that what was formally a large portion of the leading edge is now forced onto each side wall. Because of this, only a small portion of the former leading edge is parallel to the front boundary in the channel. The rest of the former leading edge is now parallel to the channel walls. So there is a shift in a long stretch of the transverse arcs from running parallel to the leading edge to running perpendicular to the front in a direction parallel to the side walls back toward the nucleus. Also the DSF's which were formery extending radially back toward the nucleus are now extending from one channel wall to the axial centerline aligned parallel to the front boundary. With the natural shift in fiber orientation so that these longer contracting fibers are now running from front to back, it would only require condensation of a couple of leading DSF's in the leading protrusion with the axially oriented transverse arcs which in addition could join with backward extending ventral stress fibers thereby forming a spindle of actively contracting, axially directed stress fibers surrounding the nucleus and attaching at the cell rear.   Clearly contractions in this axially directed spindle would lead to transverse compression of the nucleus as well as pulling the rear of the cell axially forward into the channel.

After the rear of the cell has pulled into the channel, the initial orientation of the stress fibers would fit very well with the proposed AFE migrator phenotype. Dense DSF and transverse arc networks originally in the lamellum would now form plugs of DSF's parallel to the front boundary extending from one wall toward the opposite wall attached to layers of axially running contractile arcs of actin and myosin.   The condensed fibers described above would form a spindle like structure surrounding the nucleus and attaching to focal adhesions in the forward portion of the cell next to the plug. Realignment of ventral stress fibers in the rear would lead to a trailing contractile plug. The rear portion of condensed stress fibers would attach through focal adhesions near this back plug. The AFE migration phenotype would have adjusted fiber orientation and a contractile spindle spanning from the front protein hub to the rear protein hub. This phenotype would retain the ability to specifically bind to the substrate through focal adhesions. Protrusions at the leading edge through pseudopodia or invadopodia like structures would allow the cell to increase its traction footprint at the front of the cell and modulate the spindle forces compressing the nucleus.

From the AFE migration phenotype, the QSL phenotype could be easily achieved with the loss of FA's and the joining of the global contractile spindle with the front and rear plugs. With the loss of FA's, the contractile plugs in the front and rear of the cell would no longer attach directly to the substrate. In addition, the spindle attachments would need to shift away from integrin dependent wall anchorage to distal plug anchorage. The QSL phenotype would consist of a local and global contractile element. The locally contracting plugs would provide a means of applying locally variable myosin stress to achieve an axially assymetric stress distribution and a possible adhesion mechanism. The axially contracting spindle would provide necessary interconnectivity between the front and rear of the cell thereby affording a vehicle for tensional homeostasis. In addition its envelopment of the nucleus would allow for lateral squeezing of the nucleus as well as provide a direct link to the nucleus for mechanotransduction.

4.6 QSL migration model

Experimental data identified two migration subtypes with the QSL subtype being a solid candidate for employing an alternate actomyosin driven, pressure based transmission mechanism. We developed a poroelastic framework employing experimentally obtained actin profiles to quantify the material properties of the model (solid volume fraction, stiffness, and hydraulic permeability). Experimentally derived dynamic myosin distributions were incorporated to describe the active stress generating mechanism in the model. A pressure based transmission system was modeled as a viscous adhesion force that was modulated as a function of local pressure as well as augmented with a term to account for the additional drag from recoil of the trapped nucleus outward against the channel. Any proposed QSL migration mechanism would need to incorporate the following simulation derived observations.

1. The simulation predicted two engines operating interdependently. Simulations without a boundary condition to account for a global active contractile element linking the two axial ends of the cell were ineffective at producing realistic internal pressures to maintain blebbing during regional expansions that occurred during typical lengthening cycles within the cell. This emphasized the importance of an integrated contracting framework spanning the cell to maintain intracellular pressures as well as maintaining intracellular tensions that would ultimately be necessary for cell mechanosensing. This was included in addition to the asymmetric, myosin density dependent stresses that drove variable adhesion and cell movment.
2. Simulations indicated a tradeoff in anchorage. As the myosin contractions built up, higher contractile stresses were developed in the extremities. With high actin/myosin densities in these regions fluid was temporarily trapped creating temporary localized pressure hubs at each end of the cell. These pressure hubs allowed the cell to develop temporary adhesion footholds in these regions. Meanwhile, nuclear anchorage dropped as the nuclear pressure parameter decreased with ramping myosin contraction.
3. The parametric analysis illustrated that migration speed could be increased by increasing the myosin contractility parameter. Cells experienced increased migration potential when the contractility parameter was increased and slowed significantly when contractility was hindered as would occur during blebbistatin exposure.
4. A decrease in the nuclear pressure factor led to increased displacement. Thus, stronger contractions pushed the cell faster, whereas the nucleus acted as a parking brake. These results suggest that regulation proteins (lamins A/C) determining nuclear stiffness may play a critical role dictating migration potential as has been suggested previously (52)

Figure 4-4 illustrates the proposed mechanism for QSL migration. Two separate but interdependent contractile engines drive cell migration. A contractile spindle-like couple between the two axial edges allows the cell to maintain tensional homeostasis (aided by pressure dependent anchorage) forming a mechanosensing link to the nucleus as well as maintaining intracellular pressure. In addition, when combined with distal anchoring the contracting lattice could help to alleviate some of the steric recoil that the cell’s nucleus would impose on the channel walls thereby releasing the anchorage at the center of the cell and reducing nuclear imposed adhesion resistance.

The second contractile engine results in asymmetric, highly localized contractile hubs that both generate asymmetric pulling and create dynamic distal pressure foci that the cell can employ in lieu of integrin based adhesion to generate traction. These contractile/pressure hubs serve two purposes. They provide dynamic pressure dependent anchorage and they provide asymmetric myosin density dependent pulling.

Both contractile components must be engaged to migrate. Without the global pretension engine the cell would have difficulty maintaining intracellular pressure and would be incapable of mechanical communication with the local environment. Meanwhile, if localized contractile machinery were not engaged the cell would be incapable of creating adhesion with the cell wall and would merely contract and release, endlessly blebbing without any productive propulsion.

Future work includes

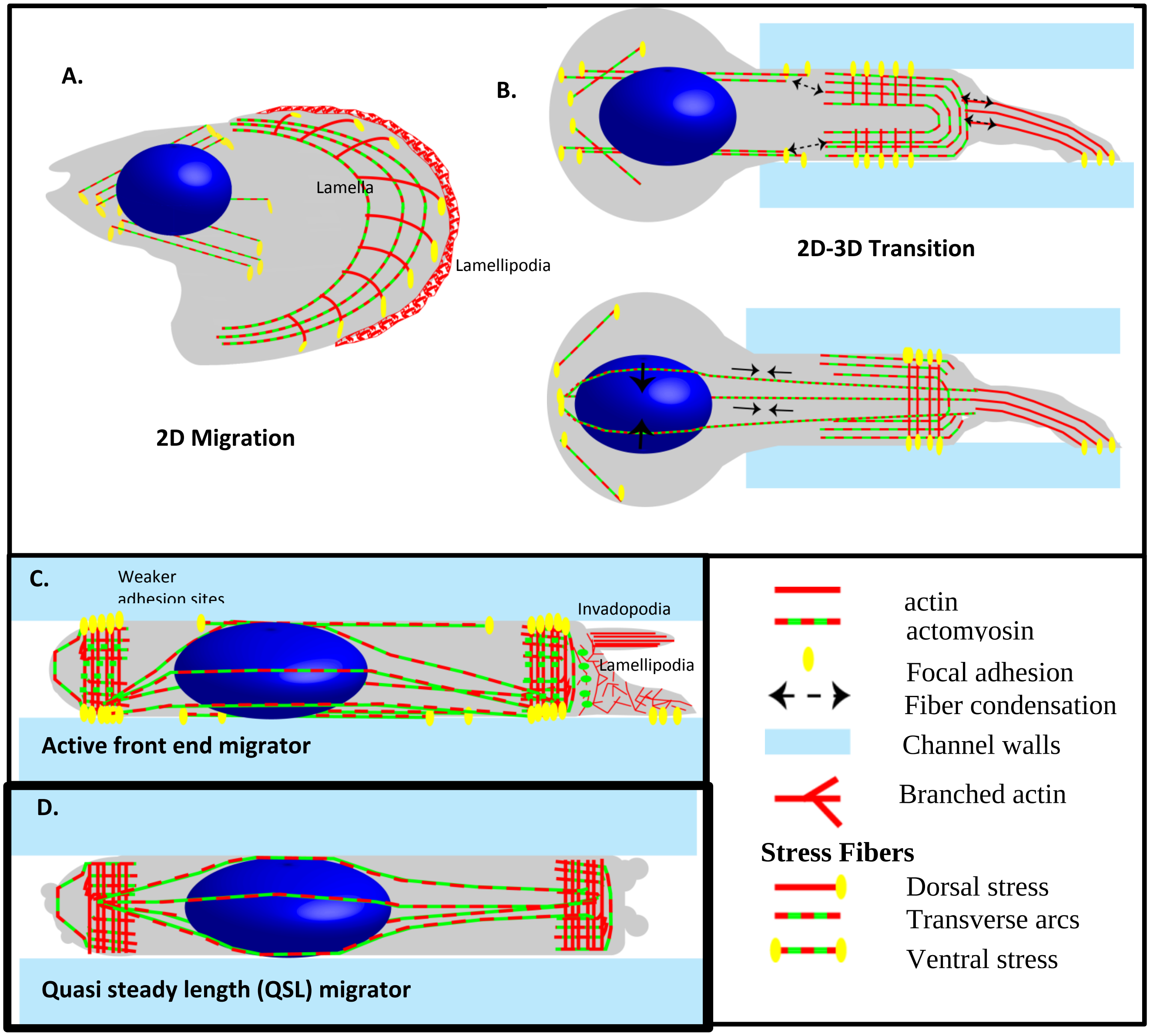

Figure 4-3. Theoretical stress fiber transition from 2D to QSL migration phenotype.

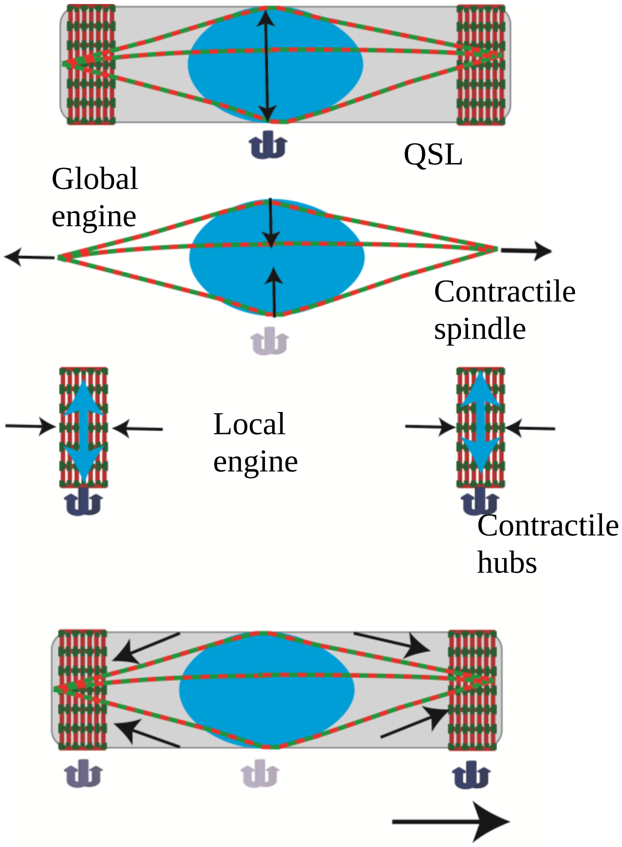

Figure 4-4. Theoretical model of QSL migration.

Appendix A

Cell Entry 5 x 5 μm^2 channel Data

GBM Cell Entering a Confined Microchannel Then Switching to a QSL Migration Mode

DIC video was recorded of a GBM cell entering a channel (fig. A-1) capturing images every 30 s for 11 minutes. Video was initiated with the GBM cell already partially inside the microchannel. The cell nucleus also had partially entered the channel. The cell was followed for 11 minutes as the nucleus entered followed by the rear of the cell. Initially the cell employed a pseudopodia/invadopodia like protrusion at the leading edge possibly aiding the cell to gain leverage to flatten the nucleus and enter.

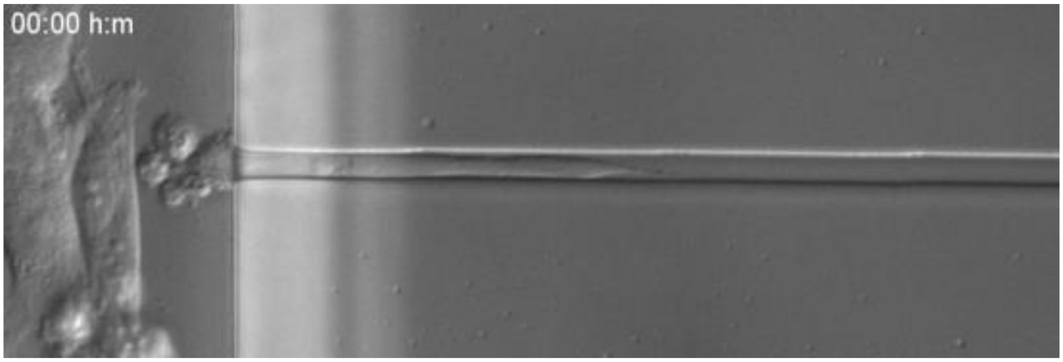

Figure A-1. GBM entering 5 x 5 μm^2 channel.

Table A-1 gives the raw data of area measurements of cell components inside and outside the channel over time. As the cell enters the channel, the associated areas change as expected with the area inside the channel increasing linearly while the area outside the channel decreased in a linear manner (fig A-2).

The nucleus fully enters the channel after about 2.5 minutes. The pseudopod appears to detach slightly after around 4 minutes and the cell transitions to blebbing at the 6 minute mark after the 1.5 to 2 minute retraction of the pseudopod. Table A-2 provides raw data of the tracking of the nuclear centroid. Fig A-3 illustrates that there appears to be a change in the nuclear speed at about the 4 to 4.5 minute mark when the pseudopod was detached. Because the nuclear extents were difficult to follow through parts of the video, the nucleolus was then tracked (Table A-4) as the nucleolus was easily identifiable throughout the video. Note that the analysis was carried out on times out to 20 minutes for the tracking of the nucleolus.

The axial displacement of the nucleus was linear with the exception of just prior to the pseudopod detachment. Fig A-5 plots the axial velocity of the nucleolus as a function of time. Interestingly, during pseudopod detachment (prior to 4 minutes) the velocity is increasing indicating an axial acceleration of the nucleolus. When the pseudopod detaches at about 4 minutes there is a steep drop in the axial velocity with a steep dip followed by an upward correction to a constant velocity. After pseudopod detachment the nucleolus continues with constant velocity.

Interestingly, when the vertical positioning of the nucleolus was tracked (fig A-6) the nucleolus appeared to cyclically bob up and down in a wave-like fashion maintaining a unbelievably repeatable period of 1 minute. Perhaps this indicates a periodic contraction within the global engine that is vertically squeezing and releasing the nucleus every 1 minute.

Table A-1. Time Dependent GBM Areas Inside and Outside Microchannel

Column1	t (mins)	Area In channel	dAin	Area Outside Channel	dAout
	0	302.924		65.929	
1	0.5	301.17	-1.754	65.134	-0.795
2	1	292.426	-8.744	58.135	-6.999
3	1.5	291.472	-0.954	48.83	-9.305
4	2	299.981	8.509	48.353	-0.477
5	2.5	304.992	5.011	49.546	1.193
6	3	313.422	8.43	46.604	-2.942
7	3.5	316.603	3.181	46.922	0.318
8	4	320.42	3.817	44.615	-2.307
9	4.5	327.737	7.317	30.937	-13.678
10	5	325.192	-2.545	36.583	5.646
11	5.5	317.08	-8.112	35.311	-1.272
12	6	317.9	1.272	27.835	-7.476
13	6.5	318.352	6.045	27.199	-0.636
14	7	324.397	7.475	27.04	-0.159
15	7.5	331.872	0.557	19.007	-8.033
16	8	332.429	3.738	22.188	3.181
17	8.5	336.167	3.419	20.996	-1.192
18	9	339.586	4.216	18.689	-2.307
19	9.5	343.802	1.057	10.975	-7.714
20	10	344.859	9.01	4.772	-6.203
21	10.5	353.869	10.212	2.863	-1.909
22	11	364.081		0	
Total Area change		**61.157**	**um^2**	**-65.929**	**um^2**
Area change/time		**5.559727273**	**um^2/min**	**-5.993545455**	**um^2/min**

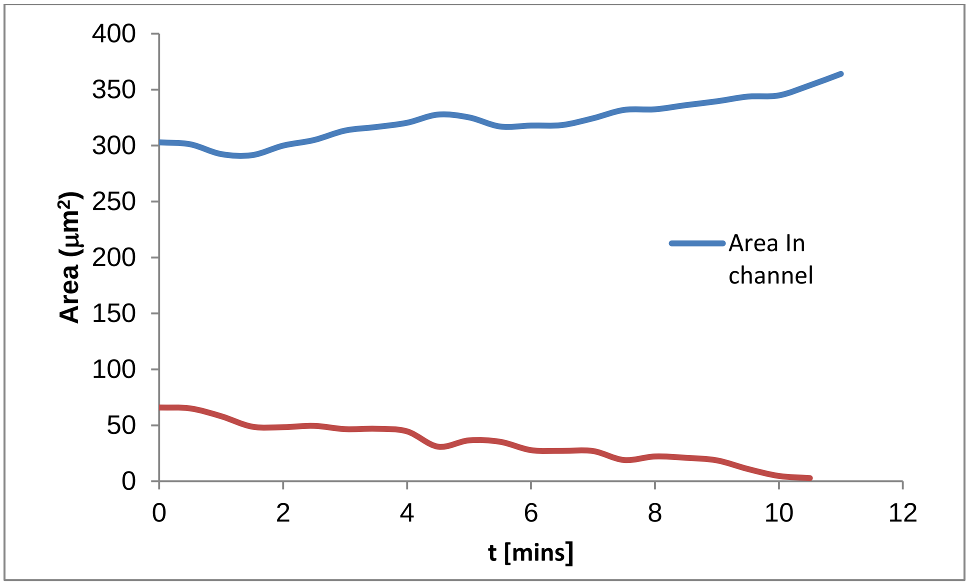

Figure A-2. Plot of cell areas inside and outside the microchannel

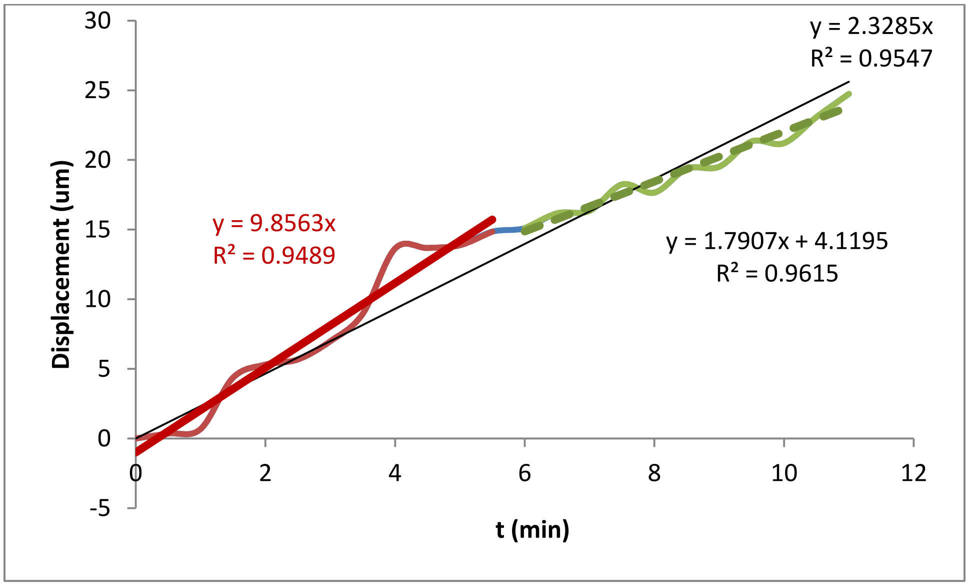

Figure A-3. Axial displacement of the nuclear centroid plotted versus time. The data appears to naturally separate into two different linear trends with the change happening between 4 and 5 minutes.

Table A-2. Raw Data of GBM Nuclear Position During Cell Entry

Column1	Column2	Column3	Column4	Column5	Column6	Column7	Column8
t (mins)	A	x	y		u (axial)	u1	u2
1	92.486	55.045	32.451	32.451	0	0	
2	91.294	55.399	32.423	32.423	0.354	0.354	
3	88.113	55.722	32.466	32.466	0.677	0.677	
4	103.699	59.41	32.473	32.473	4.365	4.365	
5	111.731	60.348	32.564	32.564	5.303	5.303	
6	115.866	60.718	32.632	32.632	5.673	5.673	
7	125.012	62.026	32.525	32.525	6.981	6.981	
8	120.32	63.988	32.561	32.561	8.943	8.943	
9	98.848	68.682	32.681	32.681	13.637	13.637	
10	101.155	68.726	32.753	32.753	13.681	13.681	
11	107.914	68.921	32.591	32.591	13.876	13.876	
12	113.799	69.896	32.556	32.556	14.851	14.851	
13	112.208	70.142	32.536	32.536	15.097		15.097
14	103.779	71.214	32.61	32.61	16.169		16.169
15	109.902	71.389	32.648	32.648	16.344		16.344
16	106.085	73.285	32.61	32.61	18.24		18.24
17	111.016	72.7	32.597	32.597	17.655		17.655
18	119.206	74.411	32.532	32.532	19.366		19.366
19	110.777	74.561	32.502	32.502	19.516		19.516
20	96.304	76.373	32.553	32.553	21.328		21.328
21	100.439	76.251	32.619	32.619	21.206		21.206
22	107.516	78.121	32.546	32.546	23.076		23.076
23	98.928	79.789	32.435	32.435	24.744		24.744

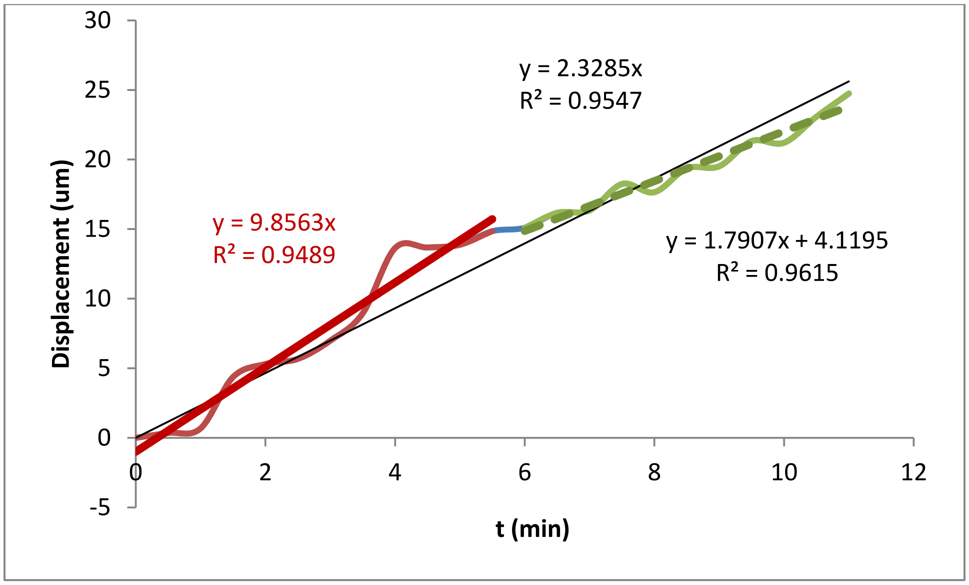

Figure A-3. Axial displacement of the nuclear centroid plotted versus time. Note that the data appears to naturally separate into two different linear trends switching somewhere between 4 and 5 minutes.

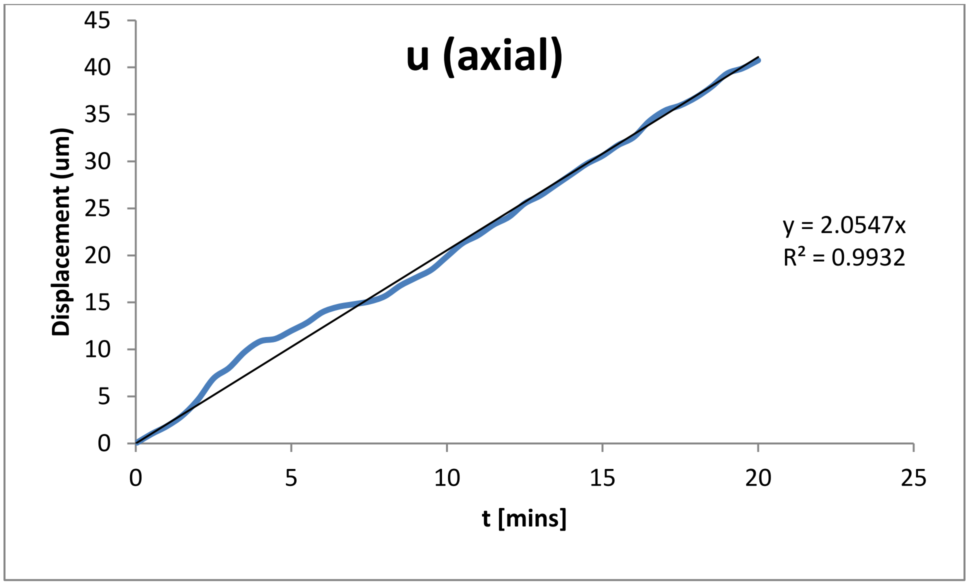

Figure A-4. Axial nucleolar displacement. Axial displacement of the nucleolus with a fitted trendline indicating a linear axial velocity of approximately 2 μm/min.

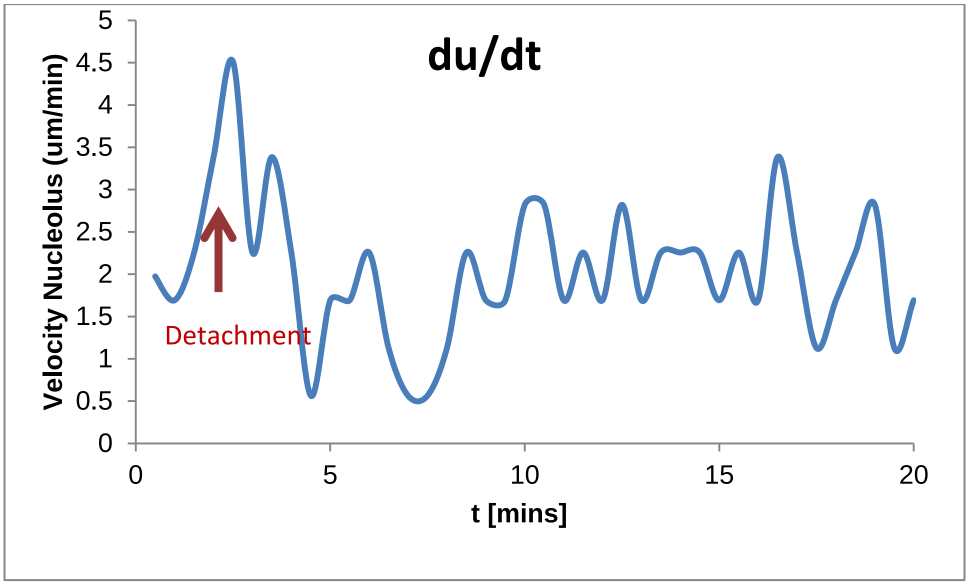

Figure A-5. Axial velocity of the nucleolus versus time. There is a sharp decrease in velocity of the nucleolus right at the moment the pseudopod detaches indicating the importance of this structure in allowing the nucleus to enter the channel.

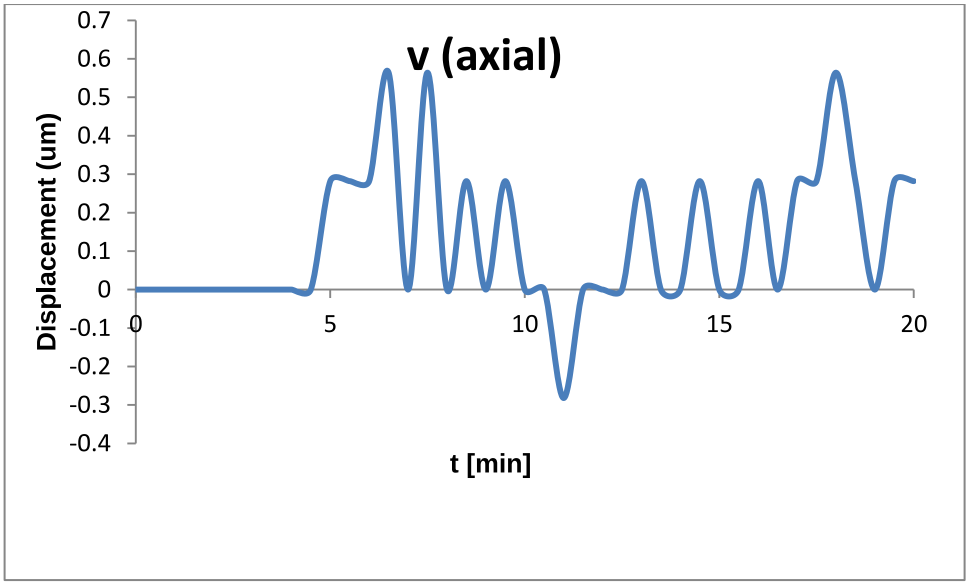

Figure A-6. Vertical displacement versus time of the nucleolus. Surprisingly there is cyclic rise and fall of the nucleolus that maintains a very repeatable 1 minute period.

Table A-4. Raw Data of GBM Nucleolus Position During Cell Entry

t (mins)	Area	X	Y	u (axial)	du/dt	v (axial)
0	8.907	64.578	32.853	0		0
0.5	10.577	65.565	32.853	0.987	1.974	0
1	10.577	66.411	32.853	1.833	1.692	0
1.5	10.577	67.539	32.853	2.961	2.256	0
2	10.577	69.231	32.853	4.653	3.384	0
2.5	10.577	71.487	32.853	6.909	4.512	0
3	10.577	72.615	32.853	8.037	2.256	0
3.5	10.577	74.307	32.853	9.729	3.384	0
4	10.577	75.435	32.853	10.857	2.256	0
4.5	10.577	75.717	32.853	11.139	0.564	0
5	10.577	76.563	33.135	11.985	1.692	0.282
5.5	10.577	77.409	33.135	12.831	1.692	0.282
6	10.577	78.537	33.135	13.959	2.256	0.282
6.5	10.577	79.101	33.417	14.523	1.128	0.564
7	10.577	79.383	32.853	14.805	0.564	0
7.5	10.577	79.665	33.417	15.087	0.564	0.564
8	10.577	80.229	32.853	15.651	1.128	0
8.5	10.577	81.357	33.135	16.779	2.256	0.282
9	10.577	82.203	32.853	17.625	1.692	0
9.5	10.577	83.049	33.135	18.471	1.692	0.282
10	10.577	84.459	32.853	19.881	2.82	0
10.5	10.577	85.869	32.853	21.291	2.82	0
11	10.577	86.715	32.571	22.137	1.692	-0.282
11.5	10.577	87.843	32.853	23.265	2.256	0
12	10.577	88.689	32.853	24.111	1.692	0
12.5	10.577	90.099	32.853	25.521	2.82	0
13	10.577	90.945	33.135	26.367	1.692	0.282
13.5	10.577	92.073	32.853	27.495	2.256	0
14	10.577	93.201	32.853	28.623	2.256	0
14.5	10.577	94.329	33.135	29.751	2.256	0.282
15	10.577	95.175	32.853	30.597	1.692	0
15.5	10.577	96.303	32.853	31.725	2.256	0
16	10.577	97.149	33.135	32.571	1.692	0.282
16.5	10.577	98.841	32.853	34.263	3.384	0
17	10.577	99.969	33.135	35.391	2.256	0.282
17.5	10.577	100.533	33.135	35.955	1.128	0.282
18	10.577	101.379	33.417	36.801	1.692	0.564
18.5	10.577	102.507	33.135	37.929	2.256	0.282
19	10.577	103.917	32.853	39.339	2.82	0
19.5	10.577	104.481	33.135	39.903	1.128	0.282
20	10.577	105.327	33.135	40.749	1.692	0.282

Appendix B

Bleb Analysis Data

Protrusion and Bleb Analysis

The tables below list the raw data derived from area and centroid measurements taken for sixteen rear and sixteen front blebs. Figures B-1 and B-2 show the history of front and rear bleb areas respectively over the 50 minutes the cell was followed.

Images are stored in BME 380 on Dell Precision T1700. The image locations can be found at E:\Jamie\GlialCellImaging_Actin\Tractin_0915_ActinRings

Table B-1 Rear Bleb 1.

t (min)	t (s)	A	X	Y	P
0.25	15	11.21	11.64	19.75	13.01
0.5	30	10.19	11.68	20.05	12.26
0.75	45	10.34	11.8	19.82	12.15
1	60	10.01	11.93	19.77	12.37
1.25	75	11.09	11.87	19.83	12.78
1.5	90	9.61	11.95	19.96	12.16
1.75	105	8.77	11.72	19.86	11.04
2	120	7.48	11.93	19.76	10.64
2.25	135	7.4	11.6	19.8	10.23
2.5	150	7.59	11.47	19.74	10.23
2.75	165	6.73	11.81	19.73	10.43
3	180	7.97	11.62	19.7	10.45
3.25	195	5.69	11.68	19.67	9.08
3.5	210	5.22	11.51	19.58	8.43
3.75	225	4.87	11.64	19.69	8.65
4	240	4.1	11.58	20.07	7.68
4.25	255	4.87	11.67	20	8.23
4.5	270	4.85	11.42	20.28	8.06
4.75	285	3.72	11.52	20.03	7.3
5	300	2.3	11.63	20.2	5.95
5.25	315	2.32	11.54	19.97	5.9
5.5	330	1.04	11.53	19.85	4.26
5.75	345	0.24	11.7	19.54	1.78

Table B-2 Rear Bleb number 2

t (min)	t (s)	A	X	Y	P
0.25	15	30.23	8.29	18.14	21.57
0.5	30	31.86	8.25	18.08	21.56
0.75	45	31.82	8.27	18.15	21.57
1	60	29.29	8.15	18.29	20.74
1.25	75	33.12	8.32	18.14	21.78
1.5	90	32.33	8.36	18.12	21.59
1.75	105	31.09	8.28	18.19	21.14
2	120	31.97	8.58	18.08	21.89
2.25	135	32.15	8.51	18.04	21.88
2.5	150	30.78	8.43	18.19	21.57
2.75	165	31.69	8.32	18.11	21.28
3	180	32.46	8.46	18.29	21.54
3.25	195	34.45	8.52	18.1	22.06
3.5	210	33.28	8.6	18.13	21.86
3.75	225	32.17	8.64	18.09	21.23
4	240	33.79	8.67	18.1	22.1
4.25	255	32.06	8.6	18.29	21.42
4.5	270	30.96	8.45	18.25	20.49
4.75	285	33.55	8.59	18.26	21.35
5	300	31.33	8.43	18.23	20.68
5.25	315	31.2	8.57	18.35	20.5
5.5	330	31.18	8.73	18.35	20.73
5.75	345	26.24	8.82	18.45	18.93
6	360	34.34	9.11	18.38	21.38
6.25	375	32.51	8.88	18.65	20.82
6.5	390	31.73	8.8	18.54	20.36
6.75	405	32.86	8.79	18.5	20.88
7	420	30.85	8.98	18.46	20.09
7.25	435	30.4	9.02	18.45	19.91
7.5	450	29.78	9.07	18.43	19.74
7.75	465	28.36	9.18	18.4	19.22
8	480	24.02	8.91	18.38	17.61
8.25	495	23.21	8.95	18.45	17.37
8.5	510	23.69	9.23	18.58	17.59
8.75	525	22.28	9.35	18.57	17.08
9	540	20.62	9.53	18.61	16.47
9.25	555	18.64	9.59	18.62	15.71
9.5	570	17.38	9.73	18.59	15.2
9.75	585	13.53	9.79	18.58	13.33
10	600	11.89	9.92	18.67	12.46
10.25	615	9.81	10.59	18.61	11.41
10.5	630	8.11	10.75	18.3	10.41

Table B-2 Continued.

10.75	645	6.47	10.88	18.49	9.26
11	660	2.83	10.6	18.52	6.2
11.25	675	3.19	10.89	18.59	6.63
11.5	690	1.17	11.19	18.5	4.07
11.75	705	0.67	11.26	18.38	3.12
12	720	0.4	11.5	18.31	2.57
12.25	735	25.55	8.81	18.4	18.61

Table B-3 Rear bleb number 3.

t (min)	t (s)	A	X	Y	P
10.5	630	0.75	11.36	16.75	3.73
10.75	645	0.88	11.03	16.68	4.18
11	660	0.88	11.03	16.68	4.18
11.25	675	1.68	11.23	16.56	5.53
11.5	690	2.46	11	16.7	6.15
11.75	705	2.72	11.28	16.79	6.59
12	720	1.81	11.45	17.01	5.1
12.25	735	1.33	11.38	16.94	4.27
12.5	750	1.24	11.7	16.98	4.11
12.75	765	0.89	12	17.24	3.52
13	780	1.2	11.94	17.13	3.93
13.25	795	0.27	12.3	17.3	1.89

Table B-4 Rear Bleb number 4.

t (min)	t (s)	A	X	Y	P
6.5	390	0.73	12.05	17.45	3.08
6.75	405	1.02	12.11	17.37	3.86
7	420	0.35	12.05	17.41	2.18

Table B-5 Rear bleb number 5.

t (min)	t (s)	A	X	Y	P
12.25	735	1.5	10.89	19.61	4.79
12.5	750	2.37	10.43	19.63	6.15
12.75	765	4.47	10.53	19.42	7.98
13	780	6.36	10.18	19.42	10.97
13.25	795	10.72	10.08	19.35	14.96
13.5	810	11.14	10.1	19.33	14.28
13.75	825	9.9	10.06	19.47	13.99
14	840	11.98	9.8	19.27	14.03
14.25	855	14.33	9.64	19.12	14.79
14.5	870	15.24	9.85	19.2	15.77
14.75	885	14.79	10.18	19.05	15.3
15	900	12.82	10.18	19.08	14.29
15.25	915	11.87	10.39	18.74	13.4
15.5	930	12.16	10.04	18.97	13.49
15.75	945	12.69	10	19.07	13.88
16	960	16.28	10.07	19.06	15.41
16.25	975	15.39	10.04	19.13	14.96
16.5	990	17	10.29	18.85	15.51
16.75	1005	17.62	10.42	19.29	15.92
17	1020	16.34	10.83	19.26	15.18
17.25	1035	15.5	10.88	19.22	14.68
17.5	1050	13.51	11.27	19.26	13.72
17.75	1065	12.62	11.41	19.26	13.19
18	1080	9.35	11.56	19.38	11.64
18.25	1095	11.45	11.73	19.52	12.61
18.5	1110	9.15	11.66	19.44	11.41
18.75	1125	8.26	11.91	19.76	10.71
19	1140	7.22	12.27	19.73	9.76
19.25	1155	7.08	12.22	19.39	10.09
19.5	1170	4.85	11.98	19.77	8.17
19.75	1185	4.98	12.11	19.95	8.2
20	1200	3.65	12.45	19.97	7.07
20.25	1215	2.44	12.45	19.64	5.91
20.5	1230	2.53	12.48	19.56	5.86
20.75	1245	2.44	12.74	19.7	5.99
21	1260	2.24	12.88	19.58	5.6

Table B-6 Rear bleb number 6.

t (min)	t (s)	A	X	Y	P
21.25	1275	1.77	12.81	19.63	4.88
21.5	1290	1.53	12.46	19.7	4.57
21.75	1305	1.53	12.46	19.7	4.57
22	1320	1	12.66	19.71	3.72
22.25	1335	0.95	12.71	20.02	3.51

Table B-7 Rear bleb number 7.

t (min)	t (s)	A	X	Y	P
15.25	915	0.89	13.4	17.04	3.77
15.5	930	4.14	12.71	17	7.78
15.75	945	5.03	12.77	17	8.37
16	960	4.56	12.97	17.11	7.94
16.25	975	4.23	13.01	17.14	7.7
16.5	990	4.07	13	17.2	7.71
16.75	1005	2.32	13.32	17.62	5.58
17	1020	1.17	13.59	17.67	3.94
17.25	1035	0.75	13.5	17.76	3.75
17.5	1050	1.53	13.65	17.36	4.71
17.75	1065	2.66	13.85	17.36	5.95
18	1080	1.86	13.46	17.79	5.09
18.25	1095	1.37	13.43	17.78	4.33
18.5	1110	0.97	13.33	17.75	3.7
18.75	1125	0.95	13.15	18.26	3.59
19	1140	0.44	13.26	18.54	2.66

Table B-8 Rear bleb number 8.

t (min)	t (s)	A	X	Y	P
16	960	0.38	14.42	16.45	2.3
16.25	975	1.13	14.44	16.46	3.92
16.5	990	1.4	14.52	16.33	4.54
16.75	1005	6.24	12.28	16.55	12.82
17	1020	7.93	11.68	16.92	14.4
17.25	1035	13.42	10.69	17.2	18.65
17.5	1050	13.8	9.4	17.21	19.64
17.75	1065	16.56	9.51	17.52	20.47

Table B-8 continued.

18	1080	18.93	9.87	17.54	20.55
18.25	1095	18.14	9.95	17.38	19.46
18.5	1110	18.58	10.14	17.4	21.9
18.75	1125	21.1	10.55	17.45	20.22
19	1140	21.43	10.63	17.51	19.78
19.25	1155	21.66	10.75	17.55	18.56
19.5	1170	21.81	10.66	17.6	20.4
19.75	1185	22.7	10.53	17.64	20.59
20	1200	22.25	10.9	17.84	19.41
20.25	1215	21.48	10.61	17.74	19.77
20.5	1230	23.89	10.72	17.92	19.6
20.75	1245	26.42	11.04	17.92	20.21
21	1260	26.68	10.84	17.92	21.03
21.25	1275	21.9	10.51	17.95	18.38
21.5	1290	20.1	10.56	17.95	17.75
21.75	1305	17.94	10.49	17.98	15.88
22	1320	19.17	10.3	18.09	16.46
22.25	1335	14.21	10.19	18.22	14.09
22.5	1350	17.78	10.56	18.32	15.83
22.75	1365	16.34	10.42	18.03	15.69
23	1380	18.98	11.01	18.1	16.12
23.25	1395	19.75	10.99	18.17	16.63
23.5	1410	16.87	11.28	18.25	15.1
23.75	1425	15.06	10.86	17.82	14.3
24	1440	15.57	10.93	17.9	14.64
24.25	1455	13.29	10.87	17.81	13.49
24.5	1470	11.03	11.04	17.67	12.09
24.75	1485	8.84	11.12	17.58	11.08
25	1500	8.22	11.21	17.48	10.58
25.25	1515	8.64	11.53	17.59	10.64
25.5	1530	7.37	11.89	17.52	9.97
25.75	1545	6.25	12.2	17.8	9.2
26	1560	8.83	11.89	17.98	11.07
26.25	1575	10.03	12.22	18.29	11.73
26.5	1590	4.83	12.27	17.78	8.14
26.75	1605	4.54	12.3	18.59	8.15
27	1620	1.55	12.32	19.04	4.77
27.25	1635	1.24	12.64	18.87	4.46
27.5	1650	1.37	12.72	19.02	5.48

Table B-9 Rear bleb number 9.

t (min)	t (s)	A	X	Y	P
25.25	1515	1.5	9.58	17.59	4.98
25.5	1530	3.7	9.26	17.52	7.24
25.75	1545	6.47	9.38	17.87	9.54
26	1560	13.46	9.64	18.3	15.51
26.25	1575	17	9.55	18.14	16.31
26.5	1590	19.22	9.43	18.16	17.19
26.75	1605	16.94	9.39	17.94	15.4
27	1620	17.34	9.46	18.2	16.25
27.25	1635	19	9.84	17.79	17.17
27.5	1650	18.09	9.88	17.93	16.74
27.75	1665	19.71	10.22	18.11	17.18
28	1680	16.83	10.38	17.89	15.8
28.25	1695	18.03	10.4	17.83	16.05
28.5	1710	19	10.83	17.88	16.74
28.75	1725	17.67	10.94	17.76	15.72
29	1740	16.85	10.57	17.85	16.07
29.5	1770	17.36	10.73	17.83	15.49

Table B-10 Rear bleb number 10.

d	t (s)	A	X	Y	P
29.75	1785	18.36	10.85	17.9	15.87
30	1800	17.1	10.69	17.91	15.25
30.25	1815	17.87	10.81	17.84	15.55
30.5	1830	18.93	10.87	18.01	16.04
30.75	1845	16.74	10.92	17.96	14.96
31	1860	18.02	10.87	17.95	15.61
31.25	1875	16.61	10.69	18.03	14.86
31.5	1890	17.16	10.75	17.99	15.12
31.75	1905	16.08	10.81	18.02	14.82
32	1920	17.32	10.93	17.9	15.16
32.25	1935	15.77	10.88	17.87	14.52
32.5	1950	15.45	10.8	17.96	14.31
32.75	1965	13.93	10.92	17.81	13.6
33.25	1995	10.65	11.18	17.5	12.04
33.5	2010	9.03	11.36	17.42	11.19

Table B-10 continued.

34	2040	8.1	11.81	17.24	10.44
34.25	2055	5.25	12.05	17.13	8.53
34.5	2070	3.46	12.28	17.17	6.9
34.75	2085	3.14	12.57	17.05	6.61
35	2100	1.86	12.65	17.28	5.03
35.25	2115	1.6	13.12	17.38	4.67
35.5	2130	1.71	13.04	17.24	4.73
35.75	2145	1.04	13.17	17.72	3.77
36	2160	1.13	13.02	17.34	4.24
36.25	2175	0.53	12.84	17.55	2.69
36.5	2190	0.57	13.08	17.43	3.04
36.75	2205	0.64	12.98	17.17	3.54

Table B-11 Rear bleb number 11.

t (min)	t (s)	A	X	Y	P
34.5	2070	1.66	10.64	17.7	5.1
34.75	2085	3.14	10.56	17.59	7.18
35	2100	4.12	10.58	17.1	9.33
35.25	2115	3.77	11.12	17.36	7.87
35.5	2130	3.32	11.38	17.49	6.95
35.75	2145	4.65	11.73	17.46	8.13
36	2160	4.45	11.85	17.53	7.89
36.25	2175	4.54	12.03	17.43	8.04
36.5	2190	4.1	12.23	17.52	7.58
36.75	2205	3.9	12.34	17.32	7.53
37	2220	3.81	12.35	17.24	7.54
37.25	2235	3.7	12.51	17.35	7.3
37.5	2250	4.05	12.7	17.43	7.33
37.75	2265	2.81	12.64	17.22	6.32
38	2280	2.9	12.78	17.48	6.38
38.25	2295	8.01	13.26	18.45	11.36
38.5	2310	4.45	13.21	18.03	8.31
38.75	2325	5.71	12.92	18.47	10.35
39	2340	4.32	13.39	18.1	9.24
39.25	2355	3.54	13.32	18	7.52
39.5	2370	10.52	12.87	18.43	13.06
39.75	2385	9.54	12.76	18.53	12.79
40	2400	7.51	13	18.47	10.96

Table B-11 continued.

40.25	2415	6.36	12.96	18.17	10.16
40.5	2430	6.66	12.79	18.29	10.94
40.75	2445	6.77	13.03	18	10.25
41	2460	6.47	13.34	17.9	9.79
41.25	2475	7.9	13.36	18.62	11.48
41.5	2490	7.06	13.48	18.05	11.22
41.75	2505	6.66	13.53	18.37	10.59
42	2520	6.18	13.34	18.21	10.2
42.25	2535	4.89	13.45	18.25	8.71
42.5	2550	3.99	13.51	18.37	8.46
42.75	2565	3.54	13.53	18.03	7.72
43	2580	2.83	13.48	17.96	7.46
43.25	2595	3.06	13.24	17.9	6.87
43.5	2610	2.97	13.25	17.95	6.94
43.75	2625	1.33	13.3	17.91	4.48
44	2640	1.02	13.45	17.8	3.82
44.25	2655	1.95	13.56	18.1	5.11
44.5	2670	1.51	13.31	18.18	4.98
44.75	2685	1.19	13.35	18.1	4.16
45.25	2715	1.71	13.38	18.52	5.26
45.5	2730	1.09	13.44	18.46	4.32
45.75	2745	0.53	13.17	18.74	3.38

Table B-13 Rear bleb number 13.

t (min)	t (s)	A	X	Y	P
46.5	2790	0.744	13.687	19.077	3.495
46.75	2805	0.991	13.287	19.179	3.677
47	2820	1.305	13.338	18.96	4.513
47.25	2835	0.826	13.487	18.873	3.472
47.5	2850	1.074	13.757	18.768	3.807
47.75	2865	0.826	13.798	18.605	3.488
48	2880	0.182	13.76	18.738	1.961
48.5	2910	0.231	14.323	18.4	2.118

Table B-14 Rear bleb number 14.

t (min)	t (s)	A	X	Y	P
46.25	2775	1.504	12.823	16.149	4.808
46.5	2790	1.256	12.736	16.169	4.454
46.75	2805	1.884	12.836	16.252	5.594
47.25	2835	2.958	13.122	16.363	6.979
47.5	2850	3.338	13.108	16.221	8.071
47.75	2865	4.461	12.558	16.141	9.595
48	2880	5.585	12.229	16.235	10.036
48.25	2895	5.403	12.472	16.287	9.183
48.5	2910	3.718	12.235	16.199	8.114
48.75	2925	4.065	12.549	16.256	7.627
49	2940	3.09	12.629	16.215	6.371
49.25	2955	2.082	12.888	16.222	5.301
49.5	2970	2.198	12.776	16.27	5.402
49.75	2985	1.322	13.123	16.425	4.386

Table B-15 Rear bleb number 15

t (min)	t (s)	A	X	Y	P
48.75	2925	0.777	12.019	17.467	4.15
49	2940	1.537	11.507	17.416	5.024
49.25	2955	5.915	11.608	16.873	9.827
49.5	2970	8.113	11.268	16.746	11.089
49.75	2985	9.468	11.54	16.665	12.057
50	3000	8.394	11.636	16.635	11.312
50.25	3015	10.839	11.439	16.644	12.595
50.5	3030	11.203	11.548	16.557	12.676
50.75	3045	10.278	11.551	16.594	12.169
51	3060	11.236	11.782	16.657	12.553
51.25	3075	11.5	11.591	16.683	12.542

Table B-16 Rear bleb number 16

t (min)	t (s)	A	X	Y	P
17.75	1065	1.355	11.978	15.985	4.402
18	1080	1.999	11.836	16.112	5.512
18.25	1095	2.693	12.139	16.058	6.939
18.5	1110	2.66	12.042	15.909	6.314
18.75	1125	3.123	12.183	16.231	7.038
19	1140	3.024	12.329	16.12	6.528
19.25	1155	3.272	12.323	16.151	6.94
19.5	1170	3.255	12.279	16.055	7.038
19.75	1185	2.644	12.219	15.935	6.144
20	1200	1.305	12.33	16.155	4.75
20.25	1215	1.223	12.55	16.25	4.215
20.5	1230	1.454	12.539	16.34	4.692

Table B-17 Front bleb number 1

t (mins)	t (s)	A	X	Y	P
0	0	10.575	70.094	17.954	12.448
0.25	15	12.758	69.861	18.001	13.275
0.5	30	11.853	69.786	17.947	12.971
0.75	45	12.483	69.834	18.035	13.24
1	60	10.963	69.755	18.076	12.422
1.25	75	11.901	69.978	18.045	13.247
1.5	90	10.883	69.847	18.039	13.151
1.75	105	11.093	69.853	17.994	12.448
2	120	12.419	69.991	17.924	13.78
2.25	135	9.767	70.025	17.913	12.433
2.5	150	10.624	69.89	18.074	13.128
2.75	165	10.883	69.861	17.87	13.264
3	180	12.451	69.785	18.034	14.31
3.25	195	10.786	69.755	18.026	13.014
3.5	210	12.241	69.729	17.892	14.444
3.75	225	9.346	69.805	17.95	12.336
4	240	10.689	69.958	17.793	13.177
4.25	255	11.287	70.074	17.819	13.68
4.5	270	12.823	69.679	17.852	13.722
4.75	285	10.866	69.736	17.751	12.943
5	300	11.077	69.618	17.917	12.54
5.25	315	11.804	69.64	17.856	13.157

Table B-17 continued.

5.5	330	12.807	69.902	17.83	13.861
5.75	345	11.804	69.932	17.835	13.421
6	360	10.915	69.71	18.007	13.3
6.25	375	9.039	69.931	18.049	11.879
6.5	390	12.112	69.819	17.757	13.353
6.75	405	11.028	69.858	18.042	12.783
7	420	11.157	69.967	18.038	13.098
7.25	435	9.735	69.977	17.95	12.266
7.5	450	11.109	69.88	17.983	12.997
7.75	465	11.352	69.899	17.97	13.393
8	480	12.16	70.086	17.85	13.614
8.25	495	11.869	69.749	17.878	13.123
8.5	510	11.934	69.765	17.884	13.441
8.75	525	13.583	69.642	17.864	13.742
9	540	13.276	69.478	17.82	13.531
9.25	555	14.844	69.217	17.948	15.308
9.5	570	14.23	69.131	17.917	14.483
9.75	585	15.216	68.658	17.89	14.936
10	600	15.62	68.726	17.943	14.705
10.25	615	13.923	68.467	17.951	13.969
10.5	630	12.677	68.68	17.936	13.565
10.75	645	12.112	68.305	17.919	13.102
11	660	12.969	68.078	17.949	13.858
11.25	675	11.853	67.847	17.962	13.064
11.5	690	11.95	67.832	18.142	14.375
11.75	705	11.901	67.831	18.008	14.293
12	720	13.486	67.735	17.923	15.063
12.25	735	12.451	67.636	17.932	13.964
12.5	750	14.505	67.493	17.931	14.541
12.75	765	12.306	67.609	18.142	14.354
13	780	13.502	67.754	17.95	14.619
13.25	795	10.09	67.48	18.03	12.198
13.5	810	12.095	67.443	18.004	13.133
13.75	825	9.637	67.673	18.002	12.294
14	840	8.78	67.558	18.158	12.084
14.25	855	8.748	67.516	18.201	11.856
14.5	870	7.487	67.705	18.193	10.877
14.75	885	5.498	67.57	18.23	9.875
15	900	5.126	67.698	18.368	9.313
15.25	915	3.089	67.879	18.568	7.164

Table B-17 continued.

15.5	930	1.536	67.709	18.612	4.95
15.75	945	1.18	67.784	18.589	4.681
16	960	0.275	67.864	18.457	2.177
16.25	975	0.065	67.523	17.676	0.823

Table B-18 Front bleb number 2.

t (mins)	t (s)	A	X	Y	P
7.75	465	1.498	70.363	18.277	4.562
8	480	2.486	70.603	18.038	6.211
8.25	495	4.076	70.773	17.981	7.489
8.5	510	4.339	70.622	17.841	8.077
8.75	525	3.196	70.607	17.907	7.593
9	540	4.956	70.266	17.673	8.28
9.25	555	3.968	70.194	17.796	7.316
9.5	570	3.675	70.257	17.61	7.041
9.75	585	2.795	69.893	17.5	6.313
10	600	0.201	69.8	17.783	1.64

Table B-19 Front bleb number 3.

t (mins)	t (s)	A	X	Y	P
8.75	525	7.072	69.764	15.663	11.765
9	540	7.983	70.318	15.705	13.329
9.25	555	10.191	70.427	15.925	14.236
9.5	570	13.618	70.399	16.124	17.005
9.75	585	17.293	70.299	16.19	19.135
10	600	18.945	70.451	16.406	18.919
10.25	615	21.323	70.277	16.38	22.56
10.5	630	20.783	70.24	16.268	20.728
10.75	645	21.292	70.298	16.336	21.244
11	660	21.277	70.163	16.281	21.877
11.25	675	21.446	70.167	16.413	21.226
11.5	690	20.921	70.063	16.358	20.114
11.75	705	23.299	70.082	16.25	21.984
12	720	22.558	69.801	16.185	21.239
12.25	735	23.531	69.873	16.308	22.269
12.5	750	23.099	69.966	16.35	21.649

Table B-19 continued.

12.75	765	23.979	69.905	16.373	21.354
13	780	25.276	69.845	16.282	22
13.25	795	24.982	69.941	16.266	21.006
13.5	810	24.982	69.941	16.266	21.641
13.75	825	25.183	69.893	16.544	21.68
14	840	25.26	69.89	16.42	20.737
14.25	855	25.569	69.83	16.434	21.399
14.5	870	25.044	69.887	16.449	20.907
14.75	885	24.349	69.794	16.441	20.306
15	900	25.322	69.855	16.43	19.956
15.25	915	25.801	69.653	16.561	20.02
15.5	930	27.484	69.231	16.588	20.81
15.75	945	26.881	69.549	16.484	20.985
16	960	30.927	69.472	16.477	21.573
16.25	975	27.484	69.666	16.588	20.487
16.5	990	29.259	69.523	16.595	20.713
16.75	1005	28.456	69.518	16.474	20.772
17	1020	27.005	69.539	16.555	20.366
17.25	1035	26.248	69.566	16.475	20.188
17.5	1050	28.595	69.333	16.443	20.791
17.75	1065	29.136	69.309	16.674	20.399
18	1080	27.437	69.345	16.5	20.44
18.25	1095	31.73	69.348	16.672	21.487
18.5	1110	27.978	69.62	16.702	20.755
18.75	1125	30.757	69.378	16.51	20.793
19	1140	30.973	69.494	16.576	21.049
19.25	1155	32.934	69.168	16.518	21.84
19.5	1170	26.82	69.264	16.585	20.094
19.75	1185	27.221	69.167	16.569	19.898
20	1200	28.781	69.218	16.498	21.085
20.25	1215	28.101	69.134	16.55	20.938
20.5	1230	27.098	69.209	16.659	19.98
20.75	1245	30.309	69.16	16.634	20.9
21	1260	30.355	69.251	16.629	20.961
21.25	1275	31.452	69.221	16.565	21.691
21.5	1290	29.182	69.265	16.52	20.978
21.75	1305	29.136	69.285	16.715	20.852
22	1320	27.669	69.285	16.559	20.761

Table B-19 continued.

22.25	1335	31.992	69.375	16.677	21.818
22.5	1350	33.15	69.286	16.664	22.549
22.75	1365	31.452	69.219	16.451	21.907
23	1380	33.521	69.044	16.699	22.281
23.25	1395	32.888	69.11	16.503	22.349
23.5	1410	32.888	69.11	16.503	22.349
23.75	1425	32.533	68.939	16.514	22.175
24	1440	31.668	68.967	16.581	21.961
24.25	1455	32.548	69.038	16.579	22.217
24.5	1470	32.424	69.094	16.622	22.008
24.75	1485	33.181	69.076	16.606	22.345
25	1500	31.899	69.016	16.624	21.59
25.25	1515	33.629	68.991	16.573	22.3
25.5	1530	33.443	68.997	16.526	22.29
25.75	1545	33.227	69.085	16.543	21.922
26	1560	33.227	69.085	16.543	21.922
26.25	1575	34.2	69.098	16.59	22.386
26.5	1590	34.092	69.126	16.527	22.408
26.75	1605	35.914	69.038	16.572	23.294
27	1620	35.914	69.105	16.623	23.02
27.25	1635	36.393	69.001	16.61	23.424
27.5	1650	37.828	69.01	16.576	24.077
27.75	1665	40.422	69.092	16.62	24.804
28	1680	38.848	68.965	16.59	24.621
28.25	1695	40.036	69.074	16.527	24.967
28.5	1710	40.376	68.999	16.622	24.897
28.75	1725	40.808	69.143	16.692	24.629
29	1740	40.314	69.101	16.717	24.823
29.25	1755	41.565	69.167	16.712	25.078
29.5	1770	42.461	69.095	16.674	25.366
29.75	1785	41.441	69.041	16.598	25.187
30	1800	39.419	69.068	16.712	24.959
30.25	1815	37.473	69.014	16.705	24.685
30.5	1830	39.944	68.978	16.671	25.297
30.75	1845	42.491	69.006	16.692	25.831
31	1860	44.699	68.921	16.65	27.125
31.25	1875	37.89	69.044	16.743	24.881
31.5	1890	38.323	68.972	16.791	24.389

Table B-19 continued.

31.75	1905	39.45	68.945	16.725	23.97
32	1920	40.268	69.113	16.698	24.263
32.25	1935	38.122	69.067	16.731	23.737
32.5	1950	36.13	69.122	16.749	23.5
32.75	1965	37.103	69.155	16.625	23.887
33	1980	37.844	69.081	16.825	24.34
33.25	1995	35.929	68.907	16.784	23.684
33.5	2010	35.852	69.092	16.784	23.89
33.75	2025	34.077	69.067	16.775	23.319
34	2040	37.319	69.046	16.759	24.204
34.25	2055	34.54	68.997	16.82	23.468
34.5	2070	35.42	69.072	16.842	24.14
34.75	2085	36.377	69.158	16.907	24.32
35	2100	35.281	69.137	16.84	24.163
35.25	2115	38.724	68.928	16.824	25.165
35.5	2130	39.959	69.117	16.886	25.807
35.75	2145	38.446	69.171	16.923	25.23
36	2160	38.77	69.075	16.886	25.207
36.25	2175	42.955	68.97	16.741	25.999
36.5	2190	40.268	68.979	16.783	25.391
36.75	2205	41.534	69.044	16.832	26.098
37	2220	42.183	68.886	16.617	26.213
37.25	2235	41.395	69.064	16.702	26.207
37.5	2250	43.495	68.909	16.623	26.312
37.75	2265	42.136	68.93	16.616	26.027
38	2280	43.279	68.924	16.763	25.908
38.25	2295	45.055	68.896	16.635	26.487
38.5	2310	39.712	69.006	16.875	25.12
38.75	2325	40.947	68.957	16.681	25.188
39	2340	41.966	69.056	16.848	25.775
39.25	2355	43.001	68.909	16.891	25.334
39.5	2370	41.133	68.767	16.808	24.817
39.75	2385	40.469	69.097	16.768	24.599
40	2400	40.484	68.737	16.809	25.011
40.25	2415	41.395	69.034	16.754	25.898
40.5	2430	41.318	69.152	16.736	25.518
40.75	2445	39.867	69.006	16.846	24.987
41	2460	39.728	69.076	16.757	25.122

Table B-19 continued.

41.25	2475	39.774	69.115	16.751	25.259
41.5	2490	38.739	69.053	16.78	25.598
41.75	2505	38.245	69.089	16.76	25.074
42	2520	40.036	69.017	16.655	25.435
42.25	2535	40.669	68.955	16.677	25.33
42.5	2550	40.16	68.909	16.764	24.89
42.75	2565	43.047	69.082	16.645	25.908
43	2580	38.168	69.358	16.741	25.751
43.25	2595	39.666	69.181	16.925	25.306
43.5	2610	42.661	69.217	16.765	25.342
43.75	2625	42.383	69.074	16.699	25.705
44	2640	44.715	69.098	16.677	26.568
44.25	2655	42.584	69.111	16.729	25.87
44.5	2670	44.082	69.001	16.705	26.215
44.75	2685	45.579	69.137	16.627	26.526
45	2700	47.139	69.099	16.565	27.075
45.25	2715	45.008	69.075	16.66	27.175
45.5	2730	44.823	69.263	16.758	26.779
45.75	2745	48.019	69.245	16.707	27.69
46	2760	43.788	69.056	16.693	26.008
46.25	2775	37.828	68.968	16.777	24.936
46.5	2790	41.689	69.089	16.773	26.506
46.75	2805	42.198	68.867	16.673	25.978
47	2820	42.553	68.841	16.778	26.55
47.25	2835	41.982	68.818	16.716	26.383
47.5	2850	47.371	68.516	16.636	27.989
47.75	2865	51.261	68.582	16.675	29.416
48	2880	50.489	68.58	16.704	29.965
48.25	2895	56.851	68.062	16.578	32.474
48.5	2910	58.657	68.211	16.704	32.665
48.75	2925	59.553	68.082	16.67	33.382
49	2940	57.36	68.129	16.778	33.109
49.25	2955	61.514	67.469	16.733	34.973
49.5	2970	67.041	67.139	16.528	36.561
49.75	2985	71.751	67.369	16.603	36.806
50	3000	63.382	67.291	16.652	36.269
50.25	3015	63.413	67.284	16.702	36.067
50.5	3030	62.008	67.293	16.762	34.817
50.75	3045	64.015	67.476	16.548	37.908
51	3060	66.439	67.167	16.636	36.57

Table B-20 Front bleb number 4.

t (mins)	t (s)	A	X	Y	P
17	1020	0.814	70.363	16.621	3.667
17.25	1035	1.881	69.651	16.313	5.207
17.5	1050	1.935	69.427	16.317	5.193
17.75	1065	1.646	69.502	16.235	5.127
18	1080	1.736	69.511	16.344	4.902
18.25	1095	1.809	69.64	16.462	4.996
18.5	1110	1.157	69.726	16.281	3.959
18.75	1125	0.109	69.864	16.407	1.139

Table B-21 Front bleb number 5.

t (mins)	t (s)	A	X	Y	P
19	1140	0.904	67.86	16.068	4.139
19.25	1155	0.651	67.675	16.011	3.818
19.5	1170	0.687	67.582	16.255	3.153
19.75	1185	1.085	67.47	16.246	4.398
20	1200	1.157	67.313	16.1	4.175
20.25	1215	0.886	67.084	16.054	3.53
20.5	1230	0.995	67.287	16.107	3.751
20.75	1245	0.959	67.261	16.114	4.025
21	1260	0.705	67.347	16.212	2.993
21.25	1275	1.754	67.697	15.974	4.97
21.5	1290	1.754	67.697	15.974	4.97
21.75	1305	1.754	67.693	16.128	4.819
22	1320	1.628	68.115	16.078	5.297
22.25	1335	1.573	67.855	16.408	4.885
22.5	1350	1.248	67.829	16.383	4.082
22.75	1365	1.085	67.932	16.342	3.84
23	1380	0.832	67.637	16.427	3.55
23.5	1410	0.579	67.658	16.386	2.952
23.75	1425	0.597	67.578	16.625	2.817
24	1440	0.452	67.659	16.727	2.635
24.25	1455	0.651	67.459	16.747	3.052
24.5	1470	0.452	67.056	16.819	2.635
25	1500	0.217	67.029	17.124	2.197

Table B-22 Front bleb number 6

t (mins)	t (s)	A	X	Y	P
23	1380	1.302	65.075	20.27	5.576
23.25	1395	4.377	65.695	20.085	9.274
23.5	1410	5.914	66.244	19.848	11.269
23.75	1425	7.632	66.299	19.398	13.45
24	1440	8.953	66.088	19.284	14.349
24.25	1455	7.415	66.033	19.402	12.956
24.5	1470	8.898	66.244	19.236	12.882
24.75	1485	8.699	66.379	19.098	12.972
25	1500	8.5	66.155	19.015	12.299
25.25	1515	7.759	66.322	18.999	11.698
25.5	1530	8.012	66.298	19.236	12.052
25.75	1545	6.457	66.32	19.119	10.641
26	1560	7.488	66.336	19.051	11.527
26.25	1575	6.583	66.361	19.112	11.073
26.5	1590	6.818	66.308	18.977	10.611
26.75	1605	6.457	66.043	19.104	10.135
27	1620	5.896	66.148	19.01	9.629
27.25	1635	4.648	65.982	19.221	8.314
27.5	1650	4.648	66.04	19.186	8.683
27.75	1665	3.78	65.686	19.037	7.884
28	1680	3.274	65.643	19.058	7.793
28.25	1695	3.78	65.547	19.031	8.05
28.5	1710	2.514	65.171	19.473	6.785
28.75	1725	0.886	65.001	19.54	3.837
29	1740	1.61	64.681	19.762	4.707
29.25	1755	1.375	64.803	19.606	4.346
29.5	1770	1.32	64.583	19.556	4.259
29.75	1785	0.922	64.575	19.248	3.549
30	1800	0.326	64.485	19.366	2.047
30.25	1815	0.072	64.283	19.298	1.173

Table B-23 Front bleb number 7.

t (mins)	t (s)	A	X	Y	P
22	1320	1.429	66.443	16.137	4.513
22.25	1335	2.297	66.147	16.284	6.37
22.5	1350	2.604	66.13	16.257	6.685
22.75	1365	2.767	66.205	16.281	6.365
23	1380	2.442	65.982	16.358	6.338
23.25	1395	3.129	66.134	16.189	7.491
23.5	1410	3.057	66.076	16.389	6.789
23.75	1425	3.382	66.046	16.417	6.841
24	1440	2.948	66.1	16.332	6.48
24.25	1455	2.604	66.045	16.483	6.13
24.5	1470	2.876	65.716	16.413	6.475
24.75	1485	2.442	65.836	16.208	6.833
25	1500	2.622	65.937	16.217	7.476
25.25	1515	2.442	66.114	16.172	7.443
25.5	1530	1.971	65.852	16.281	5.426
25.75	1545	1.284	65.451	16.514	4.644
26	1560	1.031	65.212	16.295	4.219
26.25	1575	0.344	65.065	16.538	2.785

Table B-24 Front bleb number 8.

t (mins)	t (s)	A	X	Y	P
21.75	1305	1.465	67.186	17.763	4.938
22	1320	2.405	67.139	17.745	6.125
22.25	1335	2.152	66.88	18.019	5.604
22.5	1350	2.496	67.143	17.85	5.867
22.75	1365	2.261	67.11	17.856	5.6
23	1380	1.537	66.895	18.075	4.534
23.5	1410	1.429	66.713	17.756	4.673

Table B-25 Front bleb number 9.

t (mins)	t (s)	A	X	Y	P
29	1740	1.736	65.463	16.892	4.794
29.25	1755	1.827	65.296	16.698	5.011
29.5	1770	2.46	65.263	16.82	6.368
29.75	1785	2.369	65.251	16.79	5.795
30	1800	2.514	65.17	16.707	6.058
30.25	1815	2.116	65.24	16.659	5.303
30.5	1830	1.067	65.39	16.725	4.133
30.75	1845	1.483	65.375	16.832	5.233
31	1860	1.067	65.18	16.698	4.11
31.25	1875	1.356	65.089	16.659	4.235
31.5	1890	1.013	65.032	16.493	3.686
31.75	1905	0.886	64.746	16.658	3.487
32	1920	0.814	64.984	16.549	3.355
32.25	1935	0.47	64.904	16.676	2.513

Table B-26 Front bleb number 10.

t (mins)	t (s)	A	X	Y	P
32.5	1950	1.284	64.504	16.107	4.126
32.75	1965	1.085	64.294	16.091	4.259
33	1980	1.194	64.039	16.266	4.088
33.25	1995	0.922	63.9	16.197	3.53
33.5	2010	1.121	63.782	16.437	3.794
33.75	2025	0.796	63.742	16.352	3.496
34	2040	1.194	63.686	16.23	4.013
34.25	2055	0.362	63.833	16.279	2.21
34.5	2070	0.289	63.686	16.432	1.994

Table B-27 Front bleb number 11.

t (mins)	t (s)	A	X	Y	P
28.75	1725	2.478	66.071	19.465	6.144
29	1740	4.449	66.399	19.546	7.986
29.25	1755	4.178	66.541	19.414	8.208
29.5	1770	3.545	66.305	19.681	7.413
29.75	1785	4.16	66.101	19.507	7.964
30	1800	4.467	65.96	19.493	8.171
30.25	1815	5.028	65.776	19.533	8.652
30.5	1830	4.63	65.668	19.447	7.985
30.75	1845	4.214	65.968	19.305	7.699
31	1860	3.834	65.762	19.434	7.562
31.25	1875	3.599	65.577	19.662	7.397
31.5	1890	4.829	65.575	19.578	8.235
31.75	1905	4.72	65.722	19.635	8.375
32	1920	4.431	65.457	19.57	7.76
32.25	1935	1.827	64.469	19.9	5.187
32.5	1950	1.935	64.474	19.801	5.742
32.75	1965	1.519	64.32	20.004	4.954
33	1980	1.031	64.249	20.138	3.742
33.25	1995	0.597	64.033	19.995	2.894

Table B-28 Front bleb number 12.

t (mins)	t (s)	A	X	Y	P
32.5	1950	0.705	65.571	17.171	3.343
32.75	1965	2.333	65.631	16.85	5.539
33	1980	3.509	65.541	16.813	6.904
33.25	1995	4.051	65.598	16.69	7.776
33.5	2010	4.232	65.591	16.844	7.773
33.75	2025	3.925	65.423	16.684	7.479
34	2040	3.961	65.348	16.577	7.906
34.25	2055	3.744	65.108	16.682	7.098
34.5	2070	3.635	65.129	16.619	7.066
34.75	2085	3.726	65.288	16.571	7.249
35	2100	4.196	65.203	16.696	7.869
35.25	2115	3.491	64.91	16.574	7.082
35.5	2130	4.323	64.991	16.577	7.803
35.75	2145	2.839	64.703	16.493	6.238

Table B-28 continued.

36	2160	3.907	64.895	16.424	7.832
36.25	2175	4.105	64.749	16.378	8.475
36.5	2190	3.653	64.864	16.444	7.754
36.75	2205	3.183	65.06	16.602	7.274
37	2220	3.111	64.822	16.575	7.125
37.25	2235	2.478	65.115	16.397	6.633
37.5	2250	1.682	65.059	16.483	5.388
37.75	2265	1.483	65.977	16.425	5.675

Table B-29 Front bleb number 13.

t (mins)	t (s)	A	X	Y	P
33	1980	2.46	65.412	18.988	5.773
33.25	1995	6.638	66.341	19.578	10.032
33.5	2010	8.157	66.732	19.555	11.086
33.75	2025	8.573	66.634	19.422	10.914
34	2040	9.586	66.584	19.625	11.679
34.25	2055	11.213	66.561	19.525	12.661
34.5	2070	12.335	66.587	19.523	13.394
34.75	2085	11.177	66.718	19.567	12.826
35	2100	11.141	66.689	19.669	12.945
35.25	2115	14.125	66.688	19.153	14.322
35.5	2130	13.818	66.612	19.27	14.114
35.75	2145	11.937	66.424	19.503	13.981
36	2160	13.872	66.67	19.477	13.937
36.25	2175	13.98	66.865	19.186	13.96
36.5	2190	16.494	66.525	18.893	15.344
36.75	2205	14.812	66.519	19.274	14.337
37	2220	14.83	66.377	19.119	14.302
37.25	2235	14.885	66.454	19.1	14.45
37.5	2250	13.203	66.549	19.114	13.595
37.75	2265	15.373	66.539	18.858	14.585
38	2280	15.771	66.219	18.971	14.972
38.25	2295	15.246	66.361	18.682	15.079
38.5	2310	16.639	66.103	19.013	15.345
38.75	2325	13.474	66.203	18.776	13.708
39	2340	17.073	66.225	18.912	15.972
39.25	2355	17.326	66.278	19.054	15.73

Table B-29 continued.

39.5	2370	18.267	66.046	19.008	15.81
39.75	2385	18.773	66.071	19.094	15.982
40	2400	17.561	66.073	18.867	15.428
40.25	2415	18.249	65.978	19.079	16.127
40.5	2430	17.67	65.773	18.956	16.116
40.75	2445	18.321	65.517	18.925	16.29
41	2460	14.197	65.922	18.842	14.432
41.5	2490	15.572	65.736	18.788	14.958
41.75	2505	17.652	65.758	18.635	15.635
42	2520	15.825	65.536	18.907	14.889
42.25	2535	14.197	65.677	18.869	14.234
42.5	2550	15.554	65.54	19.034	14.992
42.75	2565	14.903	65.622	19.06	14.535
43	2580	15.373	65.523	18.813	14.917
43.25	2595	14.288	65.426	18.837	14.771
43.5	2610	14.523	65.407	19.208	14.913
43.75	2625	13.8	65.399	18.829	14.249
44	2640	14.867	65.305	18.989	14.423
44.25	2655	10.743	65.371	19.175	12.907
44.5	2670	9.947	65.346	19.304	12.147

Table B-30 Front bleb number 14.

t (mins)	t (s)	A	X	Y	P
44.75	2685	10.707	65.187	19.484	12.342
45	2700	8.03	64.995	19.54	11.023
45.25	2715	6.855	64.907	19.651	10.678
45.5	2730	6.963	65.028	19.551	10.97
45.75	2745	8.356	65.051	19.81	12.171
46	2760	7.162	65.376	19.84	10.206
46.25	2775	7.686	65.281	19.563	10.493
46.5	2790	5.932	65.116	19.748	9.167
46.75	2805	5.896	65.094	19.564	9.061
47	2820	6.927	64.874	19.731	10.067
47.25	2835	6.258	64.936	19.727	9.22
47.5	2850	5.173	64.685	19.8	9.581
47.75	2865	3.762	65.355	19.404	7.323
48	2880	2.098	65.353	19.105	5.369

Table B-30 continued.

48.25	2895	2.008	65	19.031	5.364
48.5	2910	1.429	65.001	18.776	4.336
48.75	2925	0.488	64.729	18.88	2.601
49	2940	0.199	64.693	18.736	1.672

Table B-31 Front bleb number 15.

t (mins)	t (s)	A	X	Y	P
37	2220	0.85	66.516	16.523	3.633
37.25	2235	3.635	67.477	16.498	7.361
37.5	2250	3.129	67.162	16.545	7.277
37.75	2265	2.387	67.855	16.181	6.735
38	2280	5.806	68.11	16.628	9.576
38.25	2295	5.498	67.875	16.256	10.028
38.5	2310	9.224	68.37	16.427	14.576
38.75	2325	9.188	68.181	16.358	13.425
39.25	2355	8.808	67.494	16.689	13.446
39.5	2370	7.234	68.095	16.745	12.438
39.75	2385	7.488	67.826	16.619	11.775
40	2400	5.986	67.879	16.451	10.772
40.25	2415	5.082	67.691	16.656	9.681
40.5	2430	6.023	67.805	16.62	10.062
40.75	2445	6.511	67.612	16.617	11.001
41	2460	8.645	67.433	16.491	17.302
41.25	2475	6.475	67.648	16.654	11.425
41.5	2490	7.18	66.977	16.521	12.332
41.75	2505	5.01	67.555	16.404	10.18
42	2520	5.408	67.068	16.75	11.139
42.25	2535	7.524	67.522	16.523	12.245
42.5	2550	3.075	66.051	16.535	7.622
42.75	2565	3.002	65.865	16.405	7.677
43	2580	2.713	65.124	16.166	6.424
43.25	2595	1.573	65.298	16.113	5.209
43.5	2610	1.592	65.497	16.176	4.561
43.75	2625	1.32	65.284	16.13	4.35
44	2640	2.008	65.584	16.071	5.461

Table B-32 Front bleb number 16.

t (mins)	t (s)	A	X	Y	P
15.5	930	1.987	65.055	16.139	5.993
15.75	945	2.957	65.064	15.843	8.465
16	960	5.708	64.754	15.798	10.099
16.25	975	8.077	65.071	16.376	11.877
16.5	990	8.633	65.2	16.439	13.629
16.75	1005	8.347	65.13	16.474	13.073
17	1020	8.363	65.264	15.916	12.7
17.25	1035	9.81	65.145	16.289	13.913
17.5	1050	11.686	65.058	16.471	14.762
17.75	1065	12.194	65.295	16.373	15.102
18	1080	9.666	65.234	16.27	14.121
18.25	1095	9.364	65.167	16.102	14.115
18.5	1110	11.606	65.175	16.18	15.119
18.75	1125	12.544	64.948	16.469	13.412
19	1140	13.943	64.621	16.525	14.033
19.25	1155	17.346	64.039	16.494	17.245
19.5	1170	16.233	64.005	16.577	16.154
19.75	1185	11.94	64.614	16.385	13.619
20	1200	15.088	64.592	16.82	14.721
20.25	1215	14.15	64.58	16.709	14.095
20.5	1230	12.115	64.563	16.622	12.722
20.75	1245	12.957	64.345	16.612	13.364
21	1260	13.578	64.464	16.675	13.72
21.25	1275	10.827	64.538	16.522	12.823
21.5	1290	12.131	64.482	16.489	13.679
21.75	1305	11.988	64.365	16.361	12.889
22	1320	12.671	64.557	16.528	13.34
22.25	1335	12.353	64.406	16.514	12.885
22.5	1350	10.509	64.634	16.583	12.441
22.75	1365	12.783	64.326	16.539	13.597
23	1380	12.099	64.503	16.663	12.9
23.25	1395	10.557	64.51	16.51	11.983
23.5	1410	10.557	64.382	16.598	12.093
23.75	1425	10.668	64.364	16.552	12.698
24	1440	11.495	64.298	16.419	12.518
24.25	1455	10.62	64.414	16.311	11.986
24.5	1470	10.175	64.333	16.396	11.721

Table B-32 continued.

24.75	1485	8.585	64.347	16.238	10.672
25	1500	8.236	64.393	16.374	10.518
25.25	1515	8.903	64.35	16.436	10.906
25.5	1530	10.128	64.392	16.136	11.776
25.75	1545	9.269	64.48	16.248	11.555
26	1560	9.635	64.748	16.191	11.561
26.25	1575	10.398	64.236	16.186	12.47
26.5	1590	9.38	64.321	16.226	11.406
26.75	1605	9.015	64.31	16.212	11.202
27	1620	8.22	64.204	16.362	10.676
27.25	1635	8.728	63.979	16.225	11.859
27.5	1650	8.49	64.12	16.579	10.761
27.75	1665	8.617	64.275	16.316	10.916
28	1680	9.587	64.467	16.182	11.371
28.25	1695	10.398	64.249	16.517	11.741
28.5	1710	11.511	63.823	16.484	12.556
28.75	1725	11.225	63.93	16.406	12.537
29	1740	9.873	63.997	16.423	12.362
29.25	1755	9.73	63.984	16.226	12.541
29.5	1770	8.41	64.257	16.222	11.04
29.75	1785	7.711	64.117	16.342	11.032
30	1800	10.525	63.889	16.174	12.953
30.25	1815	10.016	63.733	16.399	12.173
30.5	1830	10.7	63.558	16.288	13.287
30.75	1845	10.096	63.624	16.149	13.663
31	1860	10.318	63.445	16.161	13.118
31.25	1875	12.926	63.53	16.385	13.742
31.5	1890	12.862	63.607	16.322	13.987
31.75	1905	13.816	63.502	16.429	14.66
32	1920	14.563	63.557	16.479	14.888
32.25	1935	15.088	63.807	16.73	15.766
32.5	1950	15.295	63.894	16.808	15.339
32.75	1965	14.404	63.553	16.699	15.975
33	1980	12.512	63.926	16.563	13.3
33.25	1995	11.495	63.908	16.346	13.45
33.5	2010	10.096	63.906	16.483	11.883
33.75	2025	11.384	64.018	16.472	12.467
34	2040	9.587	64.031	16.342	12.625

Table B-32 continued.

34.25	2055	10.128	63.914	16.232	13.164
34.5	2070	8.474	64.033	16.082	11.789
34.75	2085	6.789	64.015	15.955	10.313
35	2100	6.693	64.127	16.027	10.214
35.25	2115	7.329	63.916	15.583	11.454
35.5	2130	8.331	64.084	15.628	12.712
35.75	2145	10.287	63.922	15.845	16.576
36	2160	7.774	63.982	15.724	13.16
36.25	2175	5.421	63.839	15.477	10.554
36.5	2190	3.402	63.788	15.433	7.651
36.75	2205	4.722	64	15.567	9.15
37	2220	2.941	64.07	15.686	6.602
37.25	2235	2.178	64.659	16.08	6.127
37.5	2250	2.607	64.335	15.82	6.01
37.75	2265	3.752	64.588	15.742	7.741
38	2280	3.625	64.658	15.943	7.798
38.25	2295	3.386	64.311	15.794	7.344
38.5	2310	4.499	64.614	15.924	8.199
38.75	2325	2.687	65.234	15.807	8.613
39	2340	3.482	64.708	15.789	10.065
39.25	2355	2.703	65.004	16.545	7.413
39.5	2370	2.369	64.989	16.963	9.273
39.75	2385	2.973	65.259	16.403	8.547
40	2400	3.18	65.249	16.283	7.699
40.25	2415	3.386	65.181	16.094	8.599
40.5	2430	3.196	64.899	16.517	9.864
40.75	2445	3.816	64.982	16.358	9.874
41	2460	3.863	64.991	16.575	10.235
41.25	2475	3.418	64.741	16.505	9.292
41.5	2490	4.022	64.99	16.26	9.537
41.75	2505	4.277	65.102	16.203	9.48
42	2520	5.676	64.656	17.019	11.73
42.25	2535	6.646	64.554	17.191	11.767
42.5	2550	10.318	64.267	16.58	13.958
42.75	2565	8.84	64.269	16.493	12.706
43	2580	10	64.185	16.299	14.018
43.25	2595	10.716	64.069	16.212	13.614
43.5	2610	11.622	63.964	16.299	14.739

Table B-32 continued.

43.75	2625	10.97	64.03	16.346	13.509
44	2640	10.064	63.949	16.309	13.576
44.25	2655	10.811	63.878	16.304	13.685
44.5	2670	10.016	63.626	16.437	12.784
44.75	2685	11.908	63.435	16.267	14.843
45	2700	13.148	63.214	16.259	15.258
45.25	2715	11.558	63.325	16.337	14.015
45.5	2730	13.673	63.474	16.304	14.94
45.75	2745	13.244	63.24	16.448	15.62
46	2760	16.392	63.401	16.553	16.634
46.25	2775	15.549	63.287	16.539	16.167
46.5	2790	15.772	63.467	16.524	16.086
46.75	2805	18.125	63.454	16.495	17.47
47	2820	17.838	63.408	16.638	16.858
47.25	2835	18.029	63.386	16.507	16.876
47.5	2850	16.185	62.965	16.682	15.569
47.75	2865	14.595	62.969	16.59	14.936
48	2880	12.894	63.032	16.677	14.864
48.25	2895	6.423	61.882	16.348	10.207
48.5	2910	7.425	62.423	16.191	10.545
48.75	2925	3.498	61.729	16.176	7.036
49	2940	7.631	61.821	15.907	10.434
49.25	2955	1.606	60.507	16.003	5.388

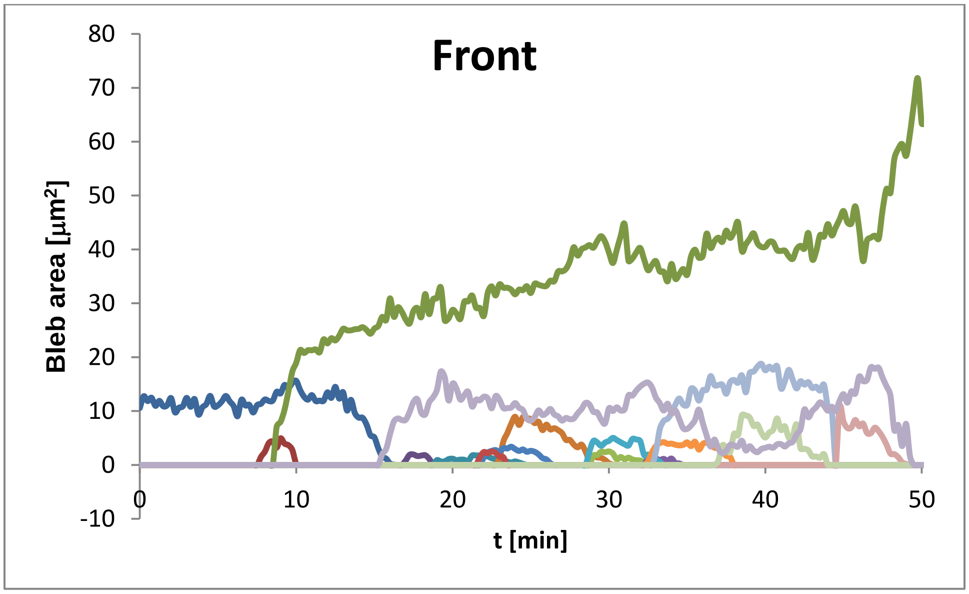

Figure B-1. Front bleb area history.

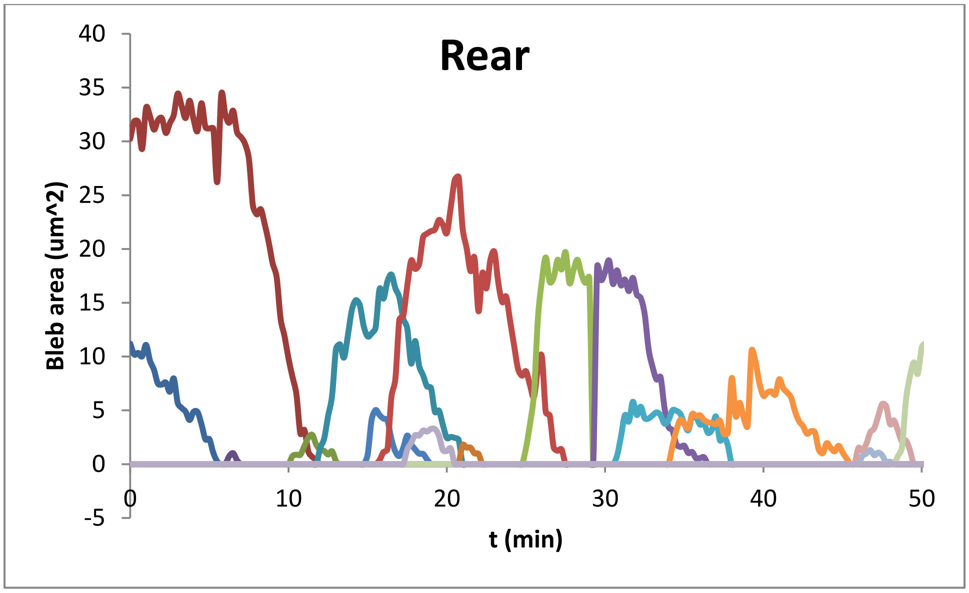

Figure B-2. Rear bleb area history.

References

1. Holland EC (2000) Glioblastoma multiforme: the terminator. *Proceedings of the National Academy of Sciences of the United States of America* 97(12):6242-6244.
2. Furnari FB*, et al.* (2007) Malignant astrocytic glioma: genetics, biology, and paths to treatment. *Genes & development* 21(21):2683-2710.
3. Wen PY & Kesari S (2008) Malignant gliomas in adults. *The New England journal of medicine* 359(5):492-507.
4. Bui L (2016) Brain Tumor Genetic Modification Yields Increased Resistance to Paclitaxel in Physical Confinement. *Scientific Reports*.
5. Friedl P & Alexander S (2011) Cancer Invasion and the Microenvironment: Plasticity and Reciprocity. *Cell* 147(5):992-1009.
6. Renkawitz J & Sixt M (2010) Mechanisms of force generation and force transmission during interstitial leukocyte migration. *EMBO reports* 11(10):744-750.
7. Theriot JA (2000) The polymerization motor. *Traffic* 1(1):19-28.
8. Ananthakrishnan R & Ehrlicher A (2007) The forces behind cell movement. *International journal of biological sciences* 3(5):303-317.
9. Fournier MF, Sauser R, Ambrosi D, Meister JJ, & Verkhovsky AB (2010) Force transmission in migrating cells. *The Journal of cell biology* 188(2):287-297.
10. Mogilner A & Oster G (2003) Force generation by actin polymerization II: the elastic ratchet and tethered filaments. *Biophysical journal* 84(3):1591-1605.
11. Mogilner A & Oster G (2003) Polymer motors: pushing out the front and pulling up the back. *Current biology : CB* 13(18):R721-733.
12. Mogilner A & Oster G (1996) Cell motility driven by actin polymerization. *Biophysical journal* 71(6):3030-3045.
13. Giannone G, Mege RM, & Thoumine O (2009) Multi-level molecular clutches in motile cell processes. *Trends in cell biology* 19(9):475-486.
14. Gardel ML, Schneider IC, Aratyn-Schaus Y, & Waterman CM (2010) Mechanical integration of actin and adhesion dynamics in cell migration. *Annual review of cell and developmental biology* 26:315-333.
15. Mogilner A (2009) Mathematics of cell motility: have we got its number? *J Math Biol* 58(1-2):105-134.
16. Cukierman E, Pankov R, Stevens DR, & Yamada KM (2001) Taking cell-matrix adhesions to the third dimension. *Science* 294(5547):1708-1712.
17. Lammermann T*, et al.* (2008) Rapid leukocyte migration by integrin-independent flowing and squeezing. *Nature* 453(7191):51-55.
18. Wilson K*, et al.* (2013) Mechanisms of leading edge protrusion in interstitial migration. *Nat Commun* 4.
19. Balzer EM*, et al.* (2012) Physical confinement alters tumor cell adhesion and migration phenotypes. *Faseb J* 26(10):4045-4056.
20. Fraley SI*, et al.* (2010) A distinctive role for focal adhesion proteins in three-dimensional cell motility. *Nat Cell Biol* 12(6):598-604.
21. Chen HC (2005) Boyden chamber assay. *Methods in molecular biology* 294:15-22.
22. Ehrbar M*, et al.* (2011) Elucidating the role of matrix stiffness in 3D cell migration and remodeling. *Biophysical journal* 100(2):284-293.

23. Wolf K, *et al.* (2013) Physical limits of cell migration: control by ECM space and nuclear deformation and tuning by proteolysis and traction force. *The Journal of cell biology* 201(7):1069-1084.
24. Petrie RJ, Koo H, & Yamada KM (2014) Generation of compartmentalized pressure by a nuclear piston governs cell motility in a 3D matrix. *Science* 345(6200):1062-1065.
25. Stroka KM, *et al.* (2014) Water permeation drives tumor cell migration in confined microenvironments. *Cell* 157(3):611-623.
26. Tong ZQ, *et al.* (2012) Chemotaxis of Cell Populations through Confined Spaces at Single-Cell Resolution. *Plos One* 7(1).
27. Irimia D & Toner M (2009) Spontaneous migration of cancer cells under conditions of mechanical confinement. *Integr Biol* 1(8-9):506-512.
28. Mak M, Reinhart-King CA, & Erickson D (2011) Microfabricated Physical Spatial Gradients for Investigating Cell Migration and Invasion Dynamics. *Plos One* 6(6).
29. Pathak A & Kumar S (2012) Independent regulation of tumor cell migration by matrix stiffness and confinement. *Proceedings of the National Academy of Sciences of the United States of America* 109(26):10334-10339.
30. Nagel O, *et al.* (2014) Geometry-Driven Polarity in Motile Amoeboid Cells. *Plos One* 9(12).
31. Belin BJ, Goins LM, & Mullins RD (2014) Comparative analysis of tools for live cell imaging of actin network architecture. *Bioarchitecture* 4(6):189-202.
32. Whitesides GM (2006) The origins and the future of microfluidics. *Nature* 442(7101):368-373.
33. Kim YT, Karthikeyan K, Chirvi S, & Dave DP (2009) Neuro-optical microfluidic platform to study injury and regeneration of single axons. *Lab on a chip* 9(17):2576-2581.
34. Kiss A, Horvath P, Rothballer A, Kutay U, & Csucs G (2014) Nuclear Motility in Glioma Cells Reveals a Cell-Line Dependent Role of Various Cytoskeletal Components. *Plos One* 9(4).
35. Dimilla PA, Barbee K, & Lauffenburger DA (1991) Mathematical-Model for the Effects of Adhesion and Mechanics on Cell-Migration Speed. *Biophysical journal* 60(1):15-37.
36. Gerbal F, Chaikin P, Rabin Y, & Prost J (2000) An elastic analysis of Listeria monocytogenes propulsion. *Biophysical journal* 79(5):2259-2275.
37. Larripa K & Mogilner A (2006) Transport of a 1D viscoelastic actin-myosin strip of gel as a model of a crawling cell. *Physica A* 372(1):113-123.
38. Sakamoto Y, Prudhomme S, & Zaman MH (2011) Viscoelastic Gel-Strip Model for the Simulation of Migrating Cells. *Ann Biomed Eng* 39(11):2735-2749.
39. Hawkins RJ, *et al.* (2009) Pushing off the walls: a mechanism of cell motility in confinement. *Physical review letters* 102(5):058103.
40. Wolgemuth CW (2005) Lamellipodial contractions during crawling and spreading. *Biophysical journal* 89(3):1643-1649.
41. Herant M & Dembo M (2010) Form and function in cell motility: from fibroblasts to keratocytes. *Biophysical journal* 98(8):1408-1417.
42. Herant M, Marganski WA, & Dembo M (2003) The mechanics of neutrophils: synthetic modeling of three experiments. *Biophysical journal* 84(5):3389-3413.

43. Shao D, Levine H, & Rappel WJ (2012) Coupling actin flow, adhesion, and morphology in a computational cell motility model. *Proceedings of the National Academy of Sciences of the United States of America* 109(18):6851-6856.
44. Charras GT, Mitchison TJ, & Mahadevan L (2009) Animal cell hydraulics. *J Cell Sci* 122(Pt 18):3233-3241.
45. Moeendarbary E*, et al.* (2013) The cytoplasm of living cells behaves as a poroelastic material. *Nature materials* 12(3):253-261.
46. Bayly PV, Taber LA, & Carlsson AE (2012) Damped and persistent oscillations in a simple model of cell crawling. *Journal of the Royal Society, Interface / the Royal Society* 9(71):1241-1253.
47. Taber LA, Shi Y, Yang L, & Bayly PV (2011) A Poroelastic Model for Cell Crawling Including Mechanical Coupling between Cytoskeletal Contraction and Actin Polymerization. *Journal of mechanics of materials and structures* 6(1-4):569-589.
48. Yang M, Taber LA, & Clark EB (1994) A nonliner poroelastic model for the trabecular embryonic heart. *Journal of biomechanical engineering* 116(2):213-223.
49. Keren K*, et al.* (2008) Mechanism of shape determination in motile cells. *Nature* 453(7194):475-480.
50. Truskey GFY, and David Katz (2009) *Transport Phenomena in Biological Systems* (Peason) 2nd Ed p 888.
51. Burnette DT*, et al.* (2014) A contractile and counterbalancing adhesion system controls the 3D shape of crawling cells. *The Journal of cell biology* 205(1):83-96.
52. Davidson PM, Denais C, Bakshi MC, & Lammerding J (2014) Nuclear deformability constitutes a rate-limiting step during cell migration in 3-D environments. *Cellular and molecular bioengineering* 7(3):293-306.
53. Friedl P, Entschladen F, Conrad C, Niggemann B, & Zanker KS (1998) CD4+ T lymphocytes migrating in three-dimensional collagen lattices lack focal adhesions and utilize beta1 integrin-independent strategies for polarization, interaction with collagen fibers and locomotion. *European journal of immunology* 28(8):2331-2343.
54. Wang N, Tytell JD, & Ingber DE (2009) Mechanotransduction at a distance: mechanically coupling the extracellular matrix with the nucleus. *Nat Rev Mol Cell Bio* 10(1):75-82.
55. Maniotis AJ, Chen CS, & Ingber DE (1997) Demonstration of mechanical connections between integrins cytoskeletal filaments, and nucleoplasm that stabilize nuclear structure. *Proceedings of the National Academy of Sciences of the United States of America* 94(3):849-854.
56. Anonymous (!!! INVALID CITATION !!!).
57. Tojkander S, Gateva G, & Lappalainen P (2012) Actin stress fibers--assembly, dynamics and biological roles. *J Cell Sci* 125(Pt 8):1855-1864.
58. Chen CS (2008) Mechanotransduction - a field pulling together? *J Cell Sci* 121(20):3285-3292.
59. Kassianidou E & Kumar S (2015) A biomechanical perspective on stress fiber structure and function. *Biochimica et biophysica acta* 1853(11 Pt B):3065-3074.

.

Chapter 3